Characterization of Rheology and Prediction of Three-Dimensional Fiber Orientation State during Injection Molding of Long Glass Fiber Reinforced Polypropylene

Vom Fachbereich Maschinenbau und Verfahrenstechnik
der Universität Kaiserslautern
zur Erlangung des akademischen Grades

Doktor-Ingenieur (Dr.-Ing.)

genehmigte Dissertation

vorgelegt von

Dipl.-Ing. Andreas Reinhardt
aus Seelen

Tag der mündlichen Prüfung:	17. Mai 2002
Prüfungsvorsitzender:	Prof. Dr.-Ing. R. Renz
1. Berichterstatter:	Prof. Dr.-Ing. M. Maier
2. Berichterstatter:	Prof. Dr. Dr. h.c. H. Neunzert
3. Berichterstatter:	Prof. S.G. Advani

D 386

Preface

This work was completed at the Institut für Verbundwerkstoffe GmbH (IVW), Kaiserslautern, and partially at the Center for Composite Materials (CCM), Newark DE, USA. Financial support was granted by the 'Stiftung Rheinland-Pfalz für Innovation'.

First and foremost, I would like to thank Prof. Dr.-Ing. M. Maier, head of the Design and Analysis division at IVW, for providing support and freedom for my professional development.

I am thankful to Prof. S.G. Advani for his guidance and encouragement throughout this research as well as his professional and personal advise. His expertise has been invaluable for completing this dissertation.

I would also like to thank Prof. Dr.-Ing. R. Renz and Prof. Dr. Dr. h.c. H. Neunzert for their participation in my comittee.

I am indebted to Prof. Dr.-Ing. H. Schüle, Dipl.-Ing. Ch. Schimmele and Dipl.-Ing. Ch. Rauer (FH Pirmasens) as well as Dipl.-Ing. G. Hens (FACT GmbH) for their support during the experimental work. I am grateful to Dr.-Ing. J. Linn for his work on fiber orientation and the lively discussions. Thanks to all those numerous members of IVW who have supported this work.

I have made lifelong friends at IVW and CCM. I wish them happiness and success.

The support and encouragement of my family has been crucial throughout all difficulties we have encountered.

This work is dedicated in love and gratitude to my father, Dieter Reinhardt.

Munich, May 2002 Andreas Reinhardt

Contents

Symbols

- Vectors are denoted in small boldface letters ($\mathbf{a}$)
- Tensors are denoted in capital boldface letters ($\mathbf{A}$)
- ($\mathbf{A} \otimes \mathbf{B}$) denotes the tensor product

Latin symbols

A	[mm^2]	area, cross-section
$\mathbf{A}$	[1]	fiber orientation tensor
a_r	[1]	aspect ratio
c_p	[J/kgK]	specific heat
C_I	[1]	interaction coefficient
D, d	[m]	diameter
d_E	[m]	penetration depth
$\mathbf{E}$	[s^{-1}]	rate of deformation tensor
f_p	[1]	fiber orientation parameter
H, h	[m]	height
k	[W/mK]	heat conductivity
k_0	[Pa s^{-n}]	consistency index of shear viscosity
L, l	[m]	length
l_0	[Pa s^{-t}]	consistency index of extensional viscosity
M_W	[g/mol]	molecular weight
n	[1]	power-law index, shear viscosity
p	[bar]	pressure
Q	[cm^3/s]	flow rate
S	[m^2]	surface area
T	[^{o}C]	temperature
$\mathbf{T}$	[N/mm^2]	stress tensor
t	[1]	power-law index, extensional viscosity
$\mathbf{v}$	[m/s]	velocity
$\mathbf{x}$	[m]	position
x, y, z	[m]	cartesian coordinates

Greek symbols

α	[1/K]	coefficient of thermal expansion
α	[1/GPa]	pressure coefficient of viscosity
β	[1/K]	temperature coefficient of viscosity
$\dot{\epsilon}$	[s^{-1}]	rate of extension
η	[Pa s]	shear viscosity
φ	[1]	volume fraction
$\dot{\gamma}$	[s^{-1}]	shear rate
λ	[Pa s]	extensional viscosity
λ	[m]	wavelength
$\mathbf{\Omega}$	[s^{-1}]	vorticity tensor
Ψ	[1]	distribution function
ϕ	[^{o}]	in-plane fiber orientation angle
ψ	[1]	mass fraction
ρ	[kg/m^3]	density
σ	[N/mm^2]	normal stress
θ	[^{o}]	out-of-plane fiber orientation angle
τ	[N/mm^2]	shear stress
μ	[1]	coefficient of absorption

Abbreviations

HDPE	high density polyethylene
GMT	glass mat reinforced thermoplastics
LDPE	low density polyethylene
LFT	long fiber reinforced thermoplastics
PA	polyamide
PA-LGF	long glass fiber reinforced polyamide
PP	polypropylene
PP-LGF	long glass fiber reinforced polypropylene
PS	polystyrene
SMC	sheet molding compounds

Zusammenfassung

Die Verarbeitung von langfaserverstärkten Thermoplasten (LFT) im Spritzgießverfahren wurde im Laufe des vergangenen Jahrzehnts als Herstellungsverfahren für Strukturbauteile in sehr hohen Stückzahlen ohne Nachbearbeitung etabliert. Während die ersten Anwendungen, die vor allem in der Automobilindustrie zu finden sind, auf einer Polyamidmatrix basierten, steigt aus Kosten- und Verarbeitungsvorteilen der Anteil von Polypropylen.
Die Eigenschaften von spritzgegossenen faserverstärkten Thermoplasten sind von der anisotropen, inhomogenen Mikrostruktur abhängig, die durch die Orientierung, die verbleibende Länge und die Dispersion der Fasern charakterisiert wird. Die Mikrostruktur entsteht durch die Strömung der fasergefüllten Schmelze und durch die Interaktion zwischen Schmelze, Fasern und Werkzeugwänden. Einfluss auf die Mikrostruktur kann durch die Materialkomposition, die Prozessführung und die Werkzeuggestaltung genommen werden.
Angesichts der Komplexität dieses Herstellungsprozesses stellt die Simulation ein wertvolles Werkzeug zur Unterstützung des Bauteilentwurfs und der Prozeßgestaltung in der Entwicklungsphase dar. Die Ergebnisse der Prozeßsimulation bilden die Grundlage für die Berechnung der Schwindung, des Verzugs und des Strukturverhaltens bei thermischer und mechanischer Belastung.
Gegenstand der Arbeit ist die Vorhersage der strömungsinduzierten Mikrostruktur bei der Spritzgießverarbeitung von langfaserverstärktem Polypropylen (PP-LGF) mittels Prozeßsimulation. Grundlage hierfür bildet die experimentelle Untersuchung des Einflusses von Materialkomposition, Verarbeitungsparametern und Geometriegrößen auf die rheologischen Eigenschaften und auf die resultierende Mikrostruktur unter prozeßnahen Bedingungen.
Die rheologischen Untersuchungen wurden unter Verwendung einer Flachschlitzdüse mit einer Spritzgießmaschine durchgeführt. Mit diesem Aufbau war gewährleistet, daß die Schmelze die identische thermische und mechanische Vorbeanspruchung des realen Herstellungsprozesses erfährt.
Anhand des Druckverlustes in der Messdüse und des Einlaufdruckverlustes bei konvergenter Strömung wurde die Scher- und Dehnviskosität von PP-LGF ermittelt. Im Rahmen der rheologischen Untersuchungen wurde festgestellt, daß die Dehnviskosität etwa zwei Größenordnungen höher als die Scherviskosität ist. Bezüglich der Verarbeitungsparameter wurde beobachtet, daß die Viskosität einerseits mit zunehmender Deformationsgeschwindigkeit und Temperatur und andererseits mit sinkendem Druck abnimmt.

Hinsichtlich der Werkstoffkomposition wurde ein dominanter Einfluss des Fasergehaltes auf die rheologischen Eigenschaften ermittelt. Eine Erhöhung der Faserlänge von 10mm auf 12mm hatte eine geringe Steigerung der Viskosität zufolge. Es wurde jedoch festgestellt, daß die Oberflächenbehandlung der Glasfasern einen signifikanten Einfluss auf die makroskopischen Fließeigenschaften der fasergefüllten Schmelze hat.
Für die Scherviskosität wurde kein Zusammenhang mit den Abmessungen des Fließspaltes festgestellt und im betrachteten Schergeschwindigkeits- und Temperaturbereich eine gute Übereinstimmung mit kapillarrheometrischen Untersuchungen an reinem PP erzielt. Hinsichtlich der Dehnviskosität wurde jedoch ein Anstieg mit zunehmender Fließspalthöhe und abnehmendem Verengungsverhältnis ermittelt.
Auf der Grundlage der rheologischen Untersuchungen wurden die Koeffizienten eines orthotropen Materialgesetzes für Polypropylen bei unterschiedlichem Fasergehalt ermittelt. Eine exponentielle Abhängigkeit der Koeffizienten von der Deformationsgeschwindigkeit und der Schmelzetemperatur ergab im betrachteten Parameterbereich eine gute Übereinstimmung mit den Ergebnissen der experimentellen Untersuchungen.
Zur Untersuchung des Zusammenhanges zwischen Mikrostruktur und rheologischen Eigenschaften wurde die Morphologie von spritzgegossenen Proben anhand von Röntgenaufnahmen mittels bildverarbeitender Methoden evaluiert. Wie bei kurzfaserverstärkten Thermoplasten war der in Kernschicht und Deckschicht unterteilbare Aufbau zu beobachten. Während in Wandnähe aufgrund der Scherströmung ein hoher Ausrichtungsgrad und eine feine Dispersion der Fasern festzustellen war, zeichnete sich die Kernschicht durch Faserbündel mit transversaler und parabolischer Orientierung aus.
Eine Erhöhung der Faserausrichtung in Hauptfließrichtung war mit steigender Deformationsgeschwindigkeit und abnehmender Schmelzetemperatur zu beobachten. Bei einem hohen Faseranteil wurde eine erhöhte Ausrichtung der Faser aufgrund der geringeren Wahrscheinlichkeit von Kollisionen zwischen den Fasern ermittelt. Eine schlechtere Qualität der Oberflächenbehandlung der Glasfasern führte zu einer regelloseren Orientierung der Fasern. Eine Erhöhung der Kanalhöhe resultierte in einer ausgeprägteren Ausrichtung.
Die Analyse der Strangaufweitung ergab eine Abnahme der elastischen Rückverformung mit zunehmender Schergeschwindigkeit, Schmelzetemperatur und steigendem Faseranteil sowie reduzierter Qualität der Faserschlichte. Für das mittlere Längen-Durchmesser-Verhältnis wurde anhand der rheologischen Ergebnisse mittels theoretischer Überlegungen Werte zwischen 60 und 135, bei einem Ausgangswert von 588, ermittelt. Die Faserlänge nimmt dabei mit zunehmendem Fasergehalt und sinkender Schmelzetemperatur ab.

Zur Evaluierung der Morphologie von LFT wurde die dreidimensionale Mikrostruktur anhand von Röntgenaufnahmen von Probenquerschnitten mittels computertomographischer Methoden rekonstruiert. Die Methode ermöglicht die Darstellung der Faserorientierung, Faserlänge und Dispersion bei praxisrelevanten Probendimensionen.
Die Ergebnisse der rheologischen Untersuchungen wurden unter Verwendung des 3D-Füllsimulationswerkzeuges SIGMASOFT verifiziert. Bei hohen Scherraten war eine Diskrepanz zwischen berechnetem und experimentell ermitteltem Temperaturanstieg in der Kavität festzustellen. Das Ausmaß der Dissipation wurde überschätzt, woraus zu schließen ist, daß die Viskositätswerte zu hoch waren. Für den Druckverlust in der Kavität war generell eine gute Übereinstimmung mit den Experimenten zu beobachten, jedoch wurde der zusätzliche Druckverlust am Einlauf, der durch Dehnströmung und Faserausrichtung in Querrichtung auftritt, nicht erfaßt.
Zur Vorhersage der 3D-Faserorientierung auf der Grundlage des simulierten Strömungsfeldes wurde am Institut für Techno- und Wirtschaftsmathematik (ITWM) ein Programm entwickelt. Die Orientierungsdynamik wurde durch das Folgar-Tucker-Modell beschrieben. Die Faser-Wand-Interaktion wurde experimentell untersucht und der stabilisierende Effekt der Wand durch eine erhöhte Scherrate modellhaft abgebildet.
Auf der Grundlage der experimentell beobachteten Verteilung der Komponenten des Faserorientierungstensors wurden die Interaktionskoeffizienten für PP-LGF bestimmt. Es ist zu beachten, daß der Interaktionskoeffizient C_I keine reine Materialgröße ist, sondern bei geringerem Fasergehalt und höherer Schmelzetemperatur ansteigt. In Verbindung mit der hybriden Abschlussapproximation wurden für Werte zwischen C_I= 0.005 und C_I= 0.025 geringste Abweichungen zwischen Simulation und experimenteller Verteilung erzielt.
Der Informationsgewinn durch Simulation mit Volumenelementen wurde anhand von Anwendungsbeispielen, sowohl bei rezirkulierender Strömung bei dickwandigen Bauteilen und Quellflußströmung an der Fließfront, als auch bei der Abbildung von Effekten durch Rippen und Kanten aufgezeigt. Die Dauer einer Simulation der Werkzeugfüllung und der Faserorientierung für ein Fahrzeugstrukturbauteil mit einem Volumen von 140 cm^3 betrug bei 100000 Zellen für die Bauteilgeometrie und 1,4 Millionen Volumen für das Spritzgießwerkzeug etwa 5 Tage.
Die Simulation des Herstellungsprozesses mit Volumenelementen stellt einen Schritt zu einem integrativen Entwicklungsprozeß dar, da die volumenbasierte Modellierung in der Konstruktion Stand der Technik ist. Aufgrund der reduzierten Dauer für die Modellgenerierung bei der Prozeßsimulation sind sowohl Kostenvorteile als auch das Potenzial für kürzere Entwicklungszeiten gegeben.

1 Introduction

In the last decade, injection molding of long-fiber reinforced thermoplastics (LFT) has been established as a low-cost, high volume technique for manufacturing parts with complex shape without any post-treatment [1–3]. Applications are mainly found in the automotive industry with a volume annually growing by 10% to 15% [4].
While first applications were based on polyamide (PA6 and PA6.6), the market share of glass fiber reinforced polypropylene (PP) is growing due to cost savings and ease of processing. With the use of polypropylene, different processing techniques such as gas-assisted injection molding [5] or injection compression molding [6] have emerged in addition to injection molding [7, 8].
In order to overcome or justify higher materials costs when compared to short fiber reinforced thermoplastics, the manufacturing techniques for LFT pellets with fiber length greater than 10mm have evolved starting from pultrusion by improving impregnation and throughput [9] or by direct addition of fiber strands in the mold [10–12].
The benefit of long glass fiber reinforcement either in PP or PA is mainly due to the enhanced resistance to fiber pull-out resulting in an increase in impact properties and strength [13–19], even at low temperature levels [20]. Creep and fatigue resistance are also substantially improved [21, 22].
The performance of fiber reinforced thermoplastics manufactured by injection molding strongly depends on the flow-induced microstructure which is driven by materials composition, processing conditions and part geometry. The anisotropic microstructure is characterized by fiber fraction and dispersion, fiber length and fiber orientation.
Facing the complexity of this processing technique, simulation becomes a precious tool already in the concept phase for parts manufactured by injection molding. Process simulation supports decisions with respect to choice of concepts and materials. The part design is determined in terms of mold filling including location of gates, vents and weld lines. Tool design requires the determination of melt feeding, logistics and mold heating. Subsequently, performance including prediction of shrinkage and warpage as well as structural analysis is evaluated [23].
While simulation based on two-dimensional representation of three-dimensional part geometry has been extensively used during the last two decades, the complexity of the parts as well as the trend towards solid modelling in CAD and CAE demands the step towards three-dimensional process simulation.

The scope of this work is the prediction of flow-induced microstructure during injection molding of long glass fiber reinforced polypropylene using three-dimensional process simulation. Modelling of the injection molding process in three dimensions is supported experimentally by rheological characterization in both shear and extensional flow and by two- and three-dimensional evaluation of microstructure.
In chapter 2 the fundamentals of rheometry and rheology are presented with respect to long fiber reinforced thermoplastics. The influence of parameters on microstructure is described and approaches for modelling the state of microstructure and its dynamics are discussed.
Chapter 3 introduces a rheometric technique allowing for rheological characterization of polymer melts at processing conditions as encountered during manufacturing. Using this rheometer, both shear and extensional viscosity of long glass fiber reinforced polypropylene are measured with respect to composition of materials, processing conditions and geometry of the cavity.
Chapter 4 contains the evaluation of microstructure of long glass fiber reinforced polypropylene in terms of two-dimensional fiber orientation and its dependence on materials parameters and processing condition. For the evaluation of three-dimensional microstructure, a technique based on x-ray tomography is introduced.
In chapter 5, modelling of microstructural dynamics is addressed. One-way coupling of interactions between fluid and fibers is described macroscopically. The flow behavior of fibers in the vicinity of cavity walls is evaluated experimentally. From these observations, a model for treatment of fiber-wall interaction with respect to numerical simulation is proposed.
Chapter 6 presents the application of three-dimensional simulation of the injection molding process. Mold filling simulation is performed using a commercial code while prediction of 3D fiber orientation is based on a proprietary module. The rheological and thermal properties derived in chapter 3 are tested by simulation of the experiments and comparison of predicted pressure and temperature profile versus recorded results. The performance of fiber orientation prediction is verified using analytical solutions of test examples from literature. The capability of three-dimensional simulation is demonstrated based on the simulation of mold filling and prediction of fiber orientation for an automotive part.

2 Fundamentals

2.1 Rheometry on long fiber reinforced thermoplastics

2.1.1 Shear flow techniques

2.1.1.1 Rotational Viscometers

Rotational viscometers, such as cone and plate viscometer, coaxial cylinder as well as torsional and disc viscometers allow for the rheological characterization of polymer melts at shear rates ranging from 0.01 to 100 $s^{-}1$ [24–26].
Typically, rotational viscometers are used for neat or short fiber reinforced thermoplastics. A cone and plate rheometer has been used by Greene [27] in order to determine the shear viscosity of PP, PA6.6 and PC reinforced by glass fibers (ψ = 0 to 45%) with an initial fiber length of 3 and 6mm. Static tests revealed that the viscosity increases with the addition of fibers but yield values of the neat polymer at high shear rates. The elasticity also increases with fiber fraction, more pronounced at low frequencies.

2.1.1.2 Extrusion rheometers

The most widely used technique in rheometry on fiber reinforced thermoplastics is performed using extrusion rheometers. The majority of studies on PP [28–36], PA6.6 [37–39], PS [40] or PU [41] reinforced by long glass fibers have been carried out using capillary rheometers. Rheological experiments on long fiber reinforced using slit dies have been conducted for PP [42, 43] or PE [44]. These rheometers are typically feeded by a plunger in a cylinder, an extruder or an injection molding machine.
Capillary rheometers usually have one pressure transducer and one separate temperature sensor. The exit effects, entry and exit pressure drop, have to be accounted for. The exit pressure drop is often of minor importance [45–47] and therefore can be neglected. Entry effects are eliminated applying the Bagley procedure, where several dies with different aspect ratio (L/D) are used. The pressure drop is then plotted versus L/D. By extrapolating the pressure drop to L/D = 0, the entry pressure drop can be determined and the pressure drop due to shear flow calculated from the overall pressure drop.

2.1.2 Elongational flow techniques

2.1.2.1 Homogeneous Stretching

An excellent review on uniaxial elongational rheometry is given in [48]. Laboratory extensional rheometry aims to achieve isothermal homogeneous deformation either at constant stress or steady strain rate [49] and measuring the resulting stress or displacement, respectively. Tests can be conducted with samples that may have constant or variable length.

2.1.2.1.1 Variable sample length

For tests at constant elongation rate, a cylindrical sample is attached at one end to a force transducer and the other end is moved outwards. The sample length increases and a total strain of 4 can be induced. Errors arise due to non-uniform deformation and temperature rise. A minimum viscosity of 10^4 Pas at processing temperature is required in order to neglect surface tension, gravity and fluid drag.
Constant stress experiments are also called creep experiments since strain is measured. Cogswell [50] subjected a sample to a constant stress using a spiral shaped cam and weights, Münstedt [51] introduced an apparatus, where a sample is extended vertically in an oil bath. As the cross-sectional area A decreases continuously, the pulling forces also reduces. The deformation is inhomogeneous due to the contraction of the melt strand and the constrain imposed by the cams. The melt is typically heated using an oil bath, with the chance of diffusion, especially with polyolefins. The melt viscosity has to be high and temperature low in order to obtain a detectable signal. For PP the maximum temperature is approximately $T_{max} = 175^o$C [52]. The method is restricted to low strain rates and requires a complex preparation of the specimen. Münstedt [53] proposed a rheometer, in which a sample, placed in an oil bath, is connected at one end to a load cell and extended by a DC servomotor. This type has been made commercially available by Göttfert and Rheometrics.

2.1.2.1.2 Constant sample length

Meissner [54,55] introduced a method, where two ends of a sample are pulled outwards by rotary clamps. The use of inert gas instead of oil reduces the chance of diffusion. Steady elongational viscosities are obtained at stretch rates $\dot{\epsilon}$ lower than 1 s^{-1}. Such an instrument enables the extensional characteristics to be evaluated at relatively low extensional strain rates but at strains up to 7.

Meissner's apparatus has evolved as a commercial instrument, the Rheometrics RME extensional rheometer [56], where nitrogen is used instead of silicone oil. A metal belt induces strains up to seven and a temperature of 350^{o}C can be achieved.

2.1.2.2 Non-uniform stretching

Meissner also introduced a rheometer, Rheotens, in which the melt is produced with constant flow rate in a laboratory extruder. The vertical melt strand is pulled at a linearly increasing velocity by two counter-rotating wheels and the pull-down force is monitored. The setup is simple and offers a qualitatively good method for comparing different melts.
However, the extensional viscosity depends on the shape of nozzle. The rate of deformation and stresses varies spatially and with time [57], therefore the transient shape of the melt strand has to be known. At elevated stretch rates, periodic pressure fluctuations may occur [52]. Wagner [58] improved the design by using a constant extrusion pressure rather than constant flow rate.
The uniaxial extensiometer, feeded by a single-screw extruder, has been applied to long fiber reinforced PP, LDPE and HDPE at stretching rates between 0.1 to 4 s^{-1} by Lin [59]. With this setup, it was observed that the drawability of the melt is reduced by the addition of long fibers. The extensional viscosity rises with fiber fraction up to a maximum but then decreases. There has been no difference in viscosity reported depending on the diameter, but the results using D = 3,5mm are not reliable due to the inhomogeneity of the melt.

2.1.2.3 Biaxial and Planar Extension Instruments

Besides sheet inflation and biaxial sheet stretching, the typical method for biaxial deformation is squeeze flow. With these rheometers, equi-biaxial elongation can be achieved [60–62]. Due to wall effects, the flow deviates from the ideal situation. Although the lubricant viscosity is small, a significant contribution to the stress difference is observed. With the loss of lubricant, shear flow becomes more pronounced. Errors due to the lubricant are induced when the sample thickness becomes very small [63].

2.1.2.4 Converging Flow

Entrance flows have received considerable attention in experimental, theoretical and computational rheology and are common features of polymer processing operations such as injection molding, extrusion and fiber spinning. In real processing, time scales, strain rates and thermo-mechanical processing effects differ considerably from those of precision controlled laboratory test conditions of the constant strain rate devices. Knowledge of low strain rate, steady state, extensional viscosities of melts subject to very high strains is important for development of understanding of polymer rheology, but is not so relevant to actual processing of such melts through complex geometry dies.
Using dies with circular or rectangular cross-section, uniaxial or planar extensional deformation is obtained. In entrance flow, the total pressure drop is due to shear flow, the viscous and elastic elongational deformation, the reorganization of velocity profile and the formation of vortices. The shear flow properties are to be known, the viscous part of the pressure drop has to be eliminated analytically [64].
In flows through convergent geometries, melts are not exposed to a pure elongational deformation, but are subjected to progressively increasing stretch rates [65]. There may also be uncertainties in strain history, for example upstream of the convergence. Previous research on neat thermoplastics [37] has demonstrated that strain history has a significant effect on the magnitude of the measured extensional viscosities. However, the velocity profile is as encountered in polymer processing. With the simple setup, stretch rates $\dot{\epsilon}$ up to 1000 s^{-1} can be achieved.

2.1.3 Analysis of elongational flow data

2.1.3.1 Cogswell's analysis

Metzner [66] and later Cogswell [67, 68] estimated extensional properties of polymer melts by applying continuum mechanics analysis to separate entry flow into shear and extensional components in the convergent flow regions encountered in abrupt entry contractions. Cogswell's model is the oldest and appears to be the most widely used in the literature.
In Cogswell's theory it is assumed that Δp can be written as the direct summation of two pressure drops, one due to shear viscosity and the other due to extensional viscosity. Based on the assumption of unconstrained convergent flow with minimum pressure consumption, Cogswell then solved for each of these two pressure drops individually, applying a force balance on a differential section of the funnel-shaped entry-flow region and integrating over the

entire entry section. The analysis assumes plug flow of plane sections in the convergent flow region. Tensile stress and extensional viscosity can be calculated from knowledge of the shear viscosity and pressure drop in a convergent section.
The minimum pressure drop equations are applicable only in the freely convergent situation where the entrance angle is large enough that the die walls do not interfere with the flow pattern. The model was extended to a constrained convergence situation. Further improvement was achieved introducing a variable power-law coefficient [69–72] or a Carreau-type constitutive law into the equation for the pressure drop [52] in order to extend the applicability of the method to low deformation rates.
The majority of processes involve the forced flow of melts through dies with complex forms where the melt stream is fixed by the profile of the flow channel surfaces giving rise to complex extensional strain fields. Although apparently simple, the flow of melts through abrupt axi-symmetric contraction geometries encompasses most elements required for developing an understanding of the processing behavior of polymer melts.

2.1.3.2 Binding's analysis

Binding [73,74] introduced a more rigorous theoretical analysis assuming convergent flow with minimum energy consumption to relate pressure drop to extensional rate and viscosity (s. appendix B.1). Viscoelastic effects were included into the theory [30] and more recently, a variable power-law coefficient [65] was introduced.

2.1.3.3 Gibson's analysis

Gibson [45] also derived expressions for extensional properties using a different analysis of entry flows. Assuming a spherical velocity field model Gibson did not attempt to predict the profile of convergence into a capillary, therefore the theory is applicable from low entrance angle to $\alpha = 90^o$. Dominant source of the entrance pressure drop is extensional flow, which does not strongly depend on the velocity profile across the die.

2.1.4 Discussion

When comparing entrance flow to other techniques, fairly good agreement in extensional viscosity data derived using an extensiometer was observed at strain rates in the power-law region for HDPE, LDPE, and PS [75, 76] and PP [76, 77]. At lower strain rates, the entrance flow data yielded an estimate of extensional viscosity that was too low. Consistency between measured extensional viscosities of PP [78] was found using free surface melt spinning. Using Gibson's, Cogswell's and Binding's technique Reasonably good agreement between the predictions was found for PE [79] and PP [52]. Cogswell's analysis yields highest values with the tendency to overestimate viscosity, to yield lower strain rates and to predict smaller natural angles when compared to Binding's analysis [79, 80]. Modification of Cogswell's analysis improved its accuracy [70, 77].

2.2 Rheology

2.2.1 Analysis of shear flow

Viscosity is derived from shear stress due to a pressure drop that drives the flow. In capillary flow, several series of injections with varying cavities are required in order to obtain a plot of pressure drop versus capillary length, also known as Bagley plot. Exit effects are eliminated by extrapolating the curve obtained to zero capillary length. With multiple transducers along the die, the pressure profile can be derived with one setup. With the assumption of a linear pressure profile

$$p(z) = a + bz \tag{2.1}$$

the exit pressure becomes

$$a = p_{exit} \tag{2.2}$$

and the pressure gradient yields

$$b = \frac{\partial p}{\partial z} \tag{2.3}$$

Assuming a parabolic pressure profile

$$p(z) = a + bz + cz^2 \tag{2.4}$$

the coefficients for a power-law type dependence of viscosity on pressure [75, 81]

$$\eta = \eta_0 \cdot e^{\alpha_\eta \cdot p} \tag{2.5}$$

can be derived as

$$\alpha_\eta = \frac{2c}{b^2} \tag{2.6}$$

Shear viscosity was calculated from shear stress at the cavity wall

$$\tau = \frac{\partial p}{\partial z} \cdot \frac{h}{2} \tag{2.7}$$

and the apparent shear rate for slit flow

$$\dot{\gamma}_a = \frac{6Q}{wh^3} \tag{2.8}$$

and capillary flow

$$\dot{\gamma}_a = \frac{4Q}{\pi r^3} \tag{2.9}$$

The influence of channel dimensions is accounted for using

$$\tau = \frac{\partial p}{\partial z} \cdot \frac{h}{2(1 + h/w)} \tag{2.10}$$

The effect of a non-parabolic velocity field in the gap-wise direction due to the non-newtonian flow behavior is accounted for using the true shear rate $\dot{\gamma}$. For slit flow $\dot{\gamma}$ yields

$$\dot{\gamma} = \frac{2n + 1}{3n} \cdot \dot{\gamma}_a \tag{2.11}$$

with the slope of shear stress versus apparent shear rate

$$n = \frac{d(log\tau)}{d(log\dot{\gamma}_a)} \tag{2.12}$$

In capillary flow, the non-newtonian effect is accounted for using

$$\dot{\gamma} = \frac{3n + 1}{4n} \cdot \dot{\gamma}_a \tag{2.13}$$

2.2.2 Analysis of extensional flow

Extensional viscosity was derived from entrance pressure drop measurements in converging dies and shear viscosity using Binding's analysis (s. appendix B.1). Power-law behavior is assumed in both shear and extensional flow:

$$\eta = k \cdot \dot{\gamma}^{n-1} \tag{2.14}$$

$$\lambda = l \cdot \dot{\epsilon}^{t-1} \tag{2.15}$$

Based on the pressure signal sampled by the sensors along the converging die, the entrance pressure drop is derived as depicted in fig. 2.1. The power-law coefficient for extensional viscosity, t, can be calculated from the entrance pressure drop with slope $t(n+1)/(t+1)$.

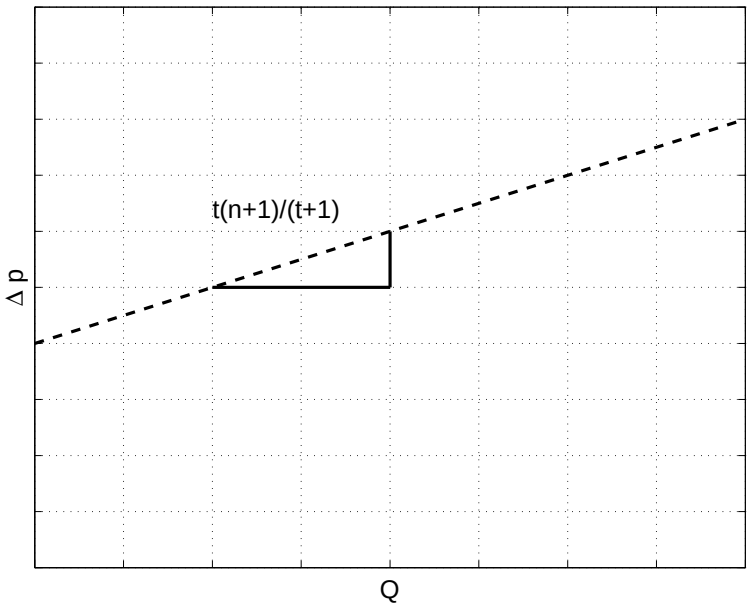

Figure 2.1: Entrance pressure drop versus flow rate

The parameter l is calculated by solving the equation for energy consumption for l (s. eqn. B.14). Finally, the maximum rate of extension is derived as

$$\dot{\epsilon} = (n+1) \cdot \left[\frac{k}{l(2n+1)tn^t \cdot I_{nt}} \right] \cdot \dot{\gamma}_{H_0}^{\left(\frac{n+1}{t+1}\right)} \tag{2.16}$$

2.2.3 Prediction of extensional viscosity

The prediction of extensional viscosity for suspensions, filled with fibers of different aspect ratio, originates from Batchelor's [82] theory for dilute suspensions of a newtonian fluid. The model was then extended to semi-dilute suspensions [83] and experimentally confirmed by Mewis and Metzner [84]. Shaqfeh and Fredrickson [85] distinguished between randomly oriented and completely aligned particles in semi-dilute suspensions. A model for an oriented fiber assembly suspended in a newtonian fluid [86] and in a carreau fluid [87] was proposed by Pipes et al.
For oriented fibers, the resistance of the fluid to extension is strongly related to the viscous resistance of the matrix since the fibers are inextensible and the matrix is subject to shearing between the fibers. The extensional viscosity is derived from both the contributions of the fibers (f) and the matrix (m)

$$\lambda = \lambda_f \cdot \varphi + \eta_m \cdot (1 - \varphi) \tag{2.17}$$

The share of the fibers depends on fiber fraction and fiber length

$$\lambda_f = k_0 \cdot (\frac{l}{d})^{n+1} \cdot F(n, \varphi) \cdot \dot{\epsilon}^{n-1} \tag{2.18}$$

Fiber length appeared to be the determining parameter for extensional viscosity

$$\frac{\lambda_f}{\eta_m} = (\frac{l}{d})^{n+1}) \cdot F(n, \varphi) \tag{2.19}$$

F characterizes the spatial distribution of the fibers and the decrease in shear rate in the vicinity of the fiber. For a power-law fluid Goddard [88] derived from Batchelor's model

$$F(n, \varphi) = \frac{2}{n+2} \left[\frac{1-n}{n} \cdot \frac{1}{1 - (\frac{\varphi}{\pi})^{\frac{1-n}{2n}}} \right]^n \tag{2.20}$$

Goddard's model has been modfied by Binding [30] in order to account for the fiber length distribution rather than for the initial fiber length. Based on the model of Coffin and Pipes for a Carreau fluid [89], the application to power-law fluids yields

$$F(n, \varphi) = \left[\sqrt{\frac{\varphi}{\pi}} - 2 \right]^n \tag{2.21}$$

2.3 Flow-induced microstructure

2.3.1 Experimental observations

The morphology of long fiber reinforced thermoplastics processed by injection molding (fig. 2.2 and 2.3) is highly anisotropic and inhomogeneous due to the interaction between fluid, fibers and cavity walls.

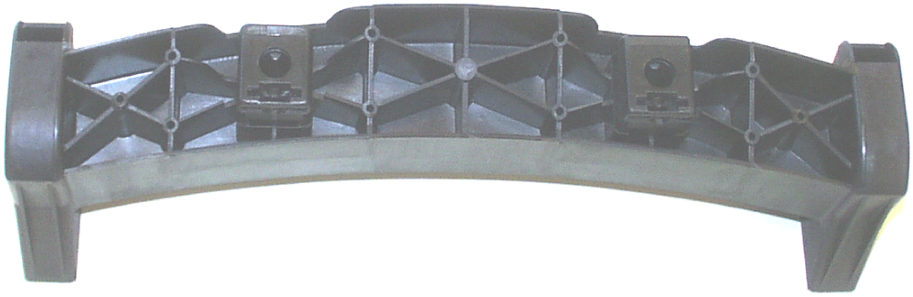

Figure 2.2: Passenger seat component

Figure 2.3: Fiber skeleton of passenger seat component

In the case of long fiber reinforced thermoplastics, microstructure is characterized by orientation, length distribution and dispersion of fibers (fig. 2.4).

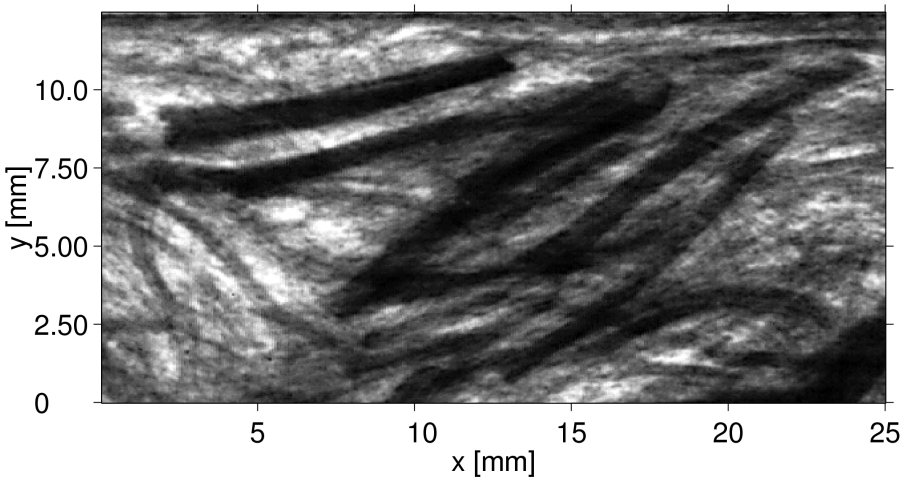

Figure 2.4: Microstructure of PP-LGF50, x-ray image

2.3.1.1 Fiber orientation

Across the thickness, three different regimes of orientation for both short fiber filled and long fibers reinforced thermoplastics are observed according to the velocity profile of non-newtonian fluids. Close to the mold wall, a very thin layer with random orientation, referred to as the skin layer, is observed. The random orientation is due to fountain flow. The shell layer is dominated by a high degree of orientation due to high shear rates. The center section of the cavity, the core zone, is characterized by a low degree of orientation due to the lack of shear deformation. In the core region, orientation therefore does not change substantially and often remains as imposed at the gate section.
When compared to short fiber-reinforced thermoplastics, the thickness of the core zone of LFT is higher, the orientation in main flow direction increases and the gap-wise orientation declines [90]. In the core zone, fibers are less oriented in the main direction of flow [90, 91]. The transverse orientation is due to extensional flow at the diverging cross-section of the gate, with its maximum at the mid-plane of the cavity.

For long fiber reinforced thermoplastics, a parabolic fiber orientation due to fiber bending is observed. The transverse orientation can be conserved during mold filling, especially in regions with lack of shear flow. The thickness of the core zone increases with flow rate and cavity height whereas the skin zone remains unchanged [92]. For the out-of-plane orientation of long fibers Skourlis [93] found that 80% of the fibers are aligned at an angle less than 20^o with respect to the midplane of the cavity.

2.3.1.2 Fiber length

The fiber length declines during plasticization of the melt and during mold filling. The average fiber length for long fiber reinforced polypropylene with an initial length of 10mm ranges between 3mm and 5mm. The critical fiber length l_c, determining whether fiber pull-out is expected to occur, yields a value of l_c = 3.1 mm for standard PP and 0.9mm for chemically modified PP [94].
With standard screws in injection molding machines, fiber length can be significantly reduced prior to the actual mold filling. The reduction in fiber length can yield values up to 50 to 55%. In simple cavities, the major amount of breakage occurs in the region with smallest cross-section, i.e. the gate. The average fiber length can be reduced to 25% to 30% of the initial fiber length.
Very often, a temporary blocking, the log-jamming effect, is reported since the length of the fibers exceeds the gate dimensions. For long fiber filled PA, jetting is also observed while PP reinforced by long fibers yields uniform mold filling. However, a certain extent of breakage due to shear deformation in cavities is present in regions with recirculating flow, rising with complexity of molds.
Metten [94] found that the variation of average fiber length with flow length corresponded to the thickness of the freezing layer near the cavity walls at the end of the filling stage. Fiber breakage occurs when one end of the long fibers is fixed in the frozen layer and the fiber is subject to shear deformation imposed by the melt. The thickness of the frozen layer in a mold is smallest at the gate and at the flow front, due to the supply with melt from the barrel and fountain flow, respectively.
With increasing flow rate, the location of the region with largest thickness of the frozen layer and hence with smallest average fiber length is shifted towards the end of the flow path. As the melt velocity increases from 40mm/s to 70mm/s, the volume average fiber length declined from 3.3mm to 2.3mm. It was also found that average fiber length strongly depends on back pressure, decreasing from 4.5mm to 2.6mm with increasing back pressure from 175bar to 600bar. Toll [90] found that the average fiber length is higher in the core, since the fiber length is reduced in the shell region due to breakage.

2.3.1.3 Fiber fraction and dispersion

Fiber fraction varies on different scales. First, fiber fraction may vary on a macroscopic level due to geometry, e.g. in ribs and weld lines. For example, with progressing mold filling, a higher fiber fraction is found at the flow front [2]. Second, according to the skin-shell-core structure, fiber fraction is not constant in gap-wise direction of the cavity and a migration in the core zone is observed since in laminar shear flow, the fibers tend to migrate in the region of highest velocity [13, 90].
Third, especially for long fibers, poor dispersion and the formation of clusters (s. fig. 2.4, 2.5 and 2.6) has been reported [95–97]. The flow of fibers in bundles preserves the average fiber length since breakage is reduced. However, there is a trade-off between dispersion and remaining fiber length, since mechanical performance increases with both fiber dispersion and fiber length.

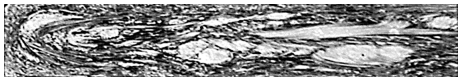

Figure 2.5: Microstructure of PP-LGF50, x-ray image of the cross-section transverse to the main direction of flow

Figure 2.6: Microstructure of PP-LGF50, x-ray image of the cross-section parallel to the main direction of flow

2.3.2 Characterization of microstructure

2.3.2.1 Fiber orientation state

The orientation of a single fiber (s. fig. 2.7) with unit length is defined by the unit vector $\mathbf{p}$, where the components of the vector are given by

$$\mathbf{p} = \left\{ \begin{array}{c} p_1 \\ p_2 \\ p_2 \end{array} \right\} = \left\{ \begin{array}{c} \sin\theta \cdot \cos\varphi \\ \sin\theta \cdot \sin\varphi \\ \cos\varphi \end{array} \right\} \tag{2.22}$$

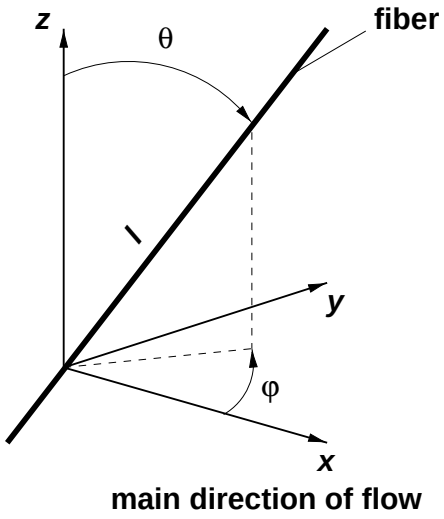

Figure 2.7: Fiber orientation

2.3.2.2 Fiber length distribution

Fiber length has an impact on both rheological and thermo-mechanical properties of fiber reinforced thermoplastics. To date, fiber length distribution is determined by pyrolising the matrix of molded specimens or by evaluating polished sections [98]. The fiber fractions are typically sorted by length into several classes and then averaged within each class. According to the method of averaging, one has to distinguish between average length by number

$$l_N = \frac{\sum l_i \cdot N_i}{\sum N_i} \tag{2.23}$$

and the fiber length averaged by volume

$$l_V = \frac{\sum {l_i}^2 \cdot N_i}{\sum l_i \cdot N_i} \tag{2.24}$$

which provides a better description for the presence of short fiber fractions. Binding [30] and Shuler [38] used an averaging method for the effective fiber length l_{eff}, for which the stress acting on the power-law type suspension is taken into account

$$l_{eff}^{n+1} = \frac{1}{N \cdot l_N} \cdot \sum N_i \cdot {l_i}^{n+2} \tag{2.25}$$

with the flow exponent n and the total number of fibers N. Applying this method reflects the influence of a small fraction of long fibers on thermo-mechanical properties.

2.3.2.3 Fiber dispersion

Fiber concentration and its variation in polymer processing has only been addressed in a small number of experimental studies [99, 100]. Information on the aggregation of particles originates almost exclusively from computer simulations (e.g. [101]).
Ranganathan and Advani [95] introduced a clustering index for characterization of fiber dispersion in short fiber filled polymers. The clustering index, derived from mixing analogy, yields a comparison of statistical differences in the primary variable of interest, e.g. components of the fiber orientation tensor.

2.3.3 Fiber orientation dynamics

In composites processing, the suspension must flow through channels or mold cavities with varying geometries. As the fibers are dispersed they do not only interact with each other, but with the walls and inserts in the mold. A model for the particle orientation must consider the non-linear effects of these interactions [102]. Several biological and engineering applications involve the flow of a suspension of particles in viscous fluids. Many researchers have addressed the aspects of fiber orientation in flowing suspensions [103–121].

2.3.3.1 Fluid-fiber interaction

Predicting the motion of particles in a flow field is a first step to understanding many complex phenomena such as the flow of red blood cells in the arteries [122–124], suspended particles in pipe flows [125, 126], the aerodynamics of bodies in wakes and boundary layers [126, 127], and in polymer processing and composites manufacturing [128–130].
The majority of macroscopic models currently used for prediction of fiber orientation are based on the classical work of Jeffery [131], who analyzed the motion of a single ellipsoidal particle in a newtonian fluid. A different model for fiber orientation was introduced by Modlen [132], based on the assumption that the fibers align according to the deformation of the surrounding fluid. Dinh and Armstrong obtained the same result while developing a constitutive law for fiber filled fluids at moderate filler fraction [133]. The model accounts for transient flow and non-newtonian fluids and has been applied for simulation of compression molding of glass-mat reinforced thermoplastics [134, 135].
Many experiments have been conducted to observe the motion of a particle in shear flow. Goldsmith and Mason [136] verified Jeffery's equations for rods and disks in low Reynolds number flow. Trevelyan and Mason [137] confirmed the motion of a long circular cylinder in uniform shear flow. Anczurowski *et al.* [138] and Okagawa *et al.* [139] observed the transient orientation evolution of a dilute suspension of cylinders in Couette flow. Folgar [140], Stover [141], and Ranganathan [142, 143] observed semi-concentrated suspensions in a Couette flow apparatus with two concentric cylinders.

2.3.3.2 Fiber-fiber interaction

The prediction using Jeffery's theory based on the assumption of dilute suspensions becomes inaccurate for concentrated suspensions. Each fiber interacts with many others. Concentrated suspensions are characterized by the number of particles per unit volume exceeding

$$N \geq \frac{1}{l^2 d} \tag{2.26}$$

For a fiber length of l = 10mm and a diameter of d = 17μm, N yields 0.6 particles per mm^3. For a fiber mass fraction in PP-LGF of 50%, which corresponds to a fiber volume fraction of 26%, the particle number per unit volume is in the order of 1200. The interaction between fibers leads to a superposed scatter on the alignment predicted using Jeffery's model.

2.3.3.3 Fiber-wall interaction

Theoretical research has been conducted for the case of particle interaction with a plane wall [102, 125, 127, 144–149], a curved surface [150], and a fluid-fluid interface [125, 151–153]. Under Poiseuille flow, it has been observed that a fiber close to a solid wall follows a pole-vaulting motion, and its centroid location from the wall is periodic [141, 154].
Stover studied the motion of a rod-like particle in a shear-thinning fluid under Poiseuille flow and observed a stabilizing effect on the fiber by the wall of the container. A fiber aligned along the wall remained there indefinitely, barring any large external perturbation.
Experiments were conducted to observe fiber orientation in injection molded parts [155, 156]. Fiber migration in the areas closest to the walls and fiber alignment in the flow direction outside this region was observed.
The interaction between fibers and the surrounding cavity is addressed experimentally in this work and a modification of Jeffery's model proposed in order to account for fiber-wall interaction.

2.3.4 Coupling of flow and orientation

The majority of approaches applied to modelling of polymer processing are based on a decoupled solution for flow and fiber orientation. While fiber orientation is calculated from the flow field, rheology is not altered by the state of orientation and its dynamics.
Models for the influence of fiber orientation on rheology were proposed by Dinh [133] and Shaqfeh [85]. The two-way coupling of flow and orientation has been examined for axi-symmetric contractions by Lipscomb [157] and for radially diverging flow by Ranganathan and Advani [113] and Chung and Kwon [158].
Verweyst [159] derived from isothermal simulations, that for radially diverging flow, coupling of flow and orientation has a minor effect on velocity and fiber orientation. However, for abrupt contractions and expansions a substantial effect is reported in the vicinity of the transition. For shear flow and planar stretching flow, the most common flow fields in injection molding, the effect of coupling fiber orientation and rheology was found to negligible.

2.4 Simulation of the injection molding process

The injection molding process is divided into the following sequence of operations

- Pre-plasticization: the fiber reinforced thermoplastic supplied either as compound or pellet is mixed and melt in the screw barrel
- Plasticization: the rotating and backward moving screw pushes the compound to the reservoir at the front end of the screw barrel
- Mold filling: the rotation of the screw is stopped and the melt is injected at high pressure (higher than 1000bar) into the mold by a system of runners and gates
- Packing: Once the mold is filled, back pressure is maintained in order to supply a uniform pressure distribution in the mold and to compensate for shrinkage of the mold
- Cooling: The melt in the cavity freezes by heat transfer from the core to the cavity walls
- Ejection of the final part

While short fiber filled polymers are compounded, long fiber reinforced thermoplastics are typically supplied as pellets (s.fig. 2.8), manufactured by pultrusion, in order to provide fiber length and to achieve high volume fraction.

Figure 2.8: PP-LGF50, x-ray image of pellets with lead glass fiber fraction

Injection molding is a highly non-linear process due to the thermal, rheological and mechanical properties of the melt [160]. Two-dimensional analysis of the injection molding process has been the standard for more than two decades [161]. While numerous papers exist addressing simulation of injection molding of short fiber reinforced thermoplastics, numerical modelling of processing of long fiber reinforced polymers has been the subject of only a limited number of studies [93, 135, 162–164].

To date, several trends are emerging. Progress towards three-dimensional mold filling simulation is inevitable since solid modelling has already become standard in CAD. Concurrent engineering, which relies on a common geometric database and unified interfaces, is becoming more important [160]. Subsequent analysis, such as prediction of warpage and shrinkage or structural analysis will also be performed using 3D models.

The assumption of two-dimensional flow, as stated in the Hele-Shaw approximation, is satisfactory for a simple geometry when the dimensions in the thickness direction are much smaller than in the flow direction. An injection molded part typically shows both thin and thick wall sections with drastic changes causing zones of recirculation. The mold is virtually complex, perhaps with ribs, and mid-plane generation can become ambiguous. The mold can also contain multiple runners and inserts. The process itself has been developed towards co-injection, gas assistance and injection compression molding. Under these circumstances, flow in a mold is typically three-dimensional.

CAE based on solid models has been considered too expensive. With increasing computing power and the transfer from workstations to PC, this fraction will further be reduced. On the other hand, the expense for data transfer, modelling (e.g. mid-plane generation) and meshing accounts is reduced. With an increasing amount of information with a 3D analysis, the total gain using 3D analysis has been estimated as 230 to 280% [165]. So far, three-dimensional simulation of injection molding has been performed in a limited number of cases [159, 166, 167].

3 Rheology

3.1 Experimental

3.1.1 Rheometer

All experiments were carried out on an injection molding machine with a screw diameter of d = 35 mm (ARBURG Allrounder 270V 500-150). The extrusion rheometer, a slit die (Fig.3.1), is mounted on the injection molding machine using an adapter [168].

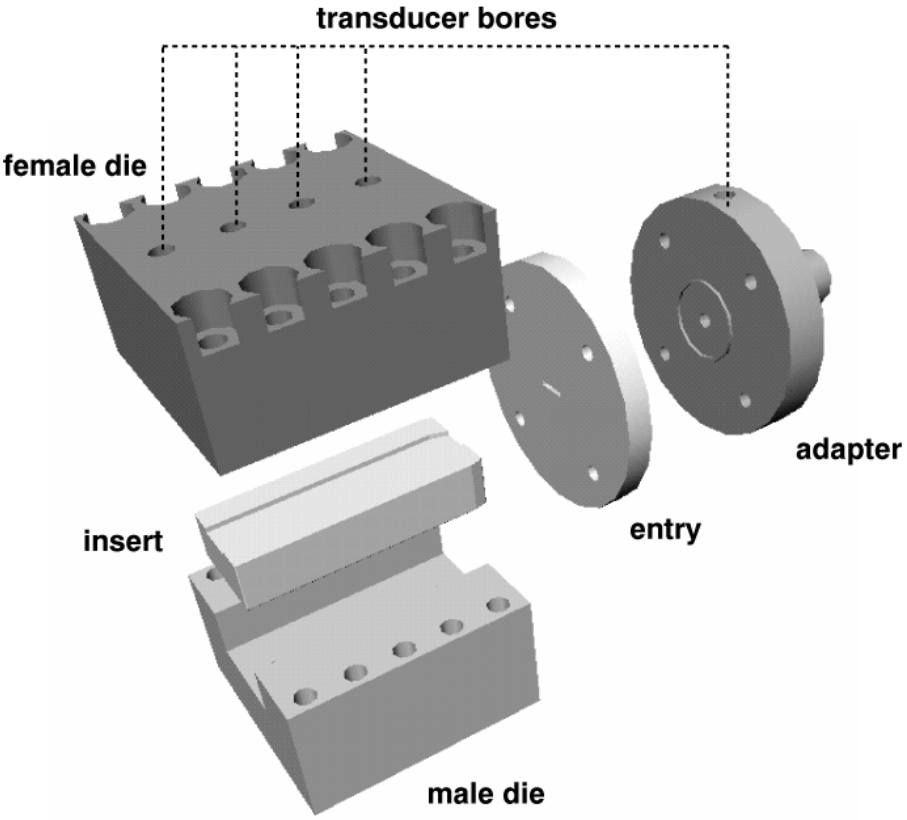

Figure 3.1: Modular rheometer

In the entrance section, the shape of the flow channel is lead from a circular to a rectangular cross section. Both the adapter and the female die incorporate drilled holes where transducers can be mounted. The insert is included in the male die.

The modular design of the cavity allows for fast modifications of the slit geometry while the rheometer is still mounted on the injection molding machine. The flow channel can easily be altered by unmounting the female die and replacing the insert. In order to achieve quasi-isothermal conditions, the rheometer is enclosed within frame and ring heaters providing a mold temperature equal to the melt temperature in the barrel.

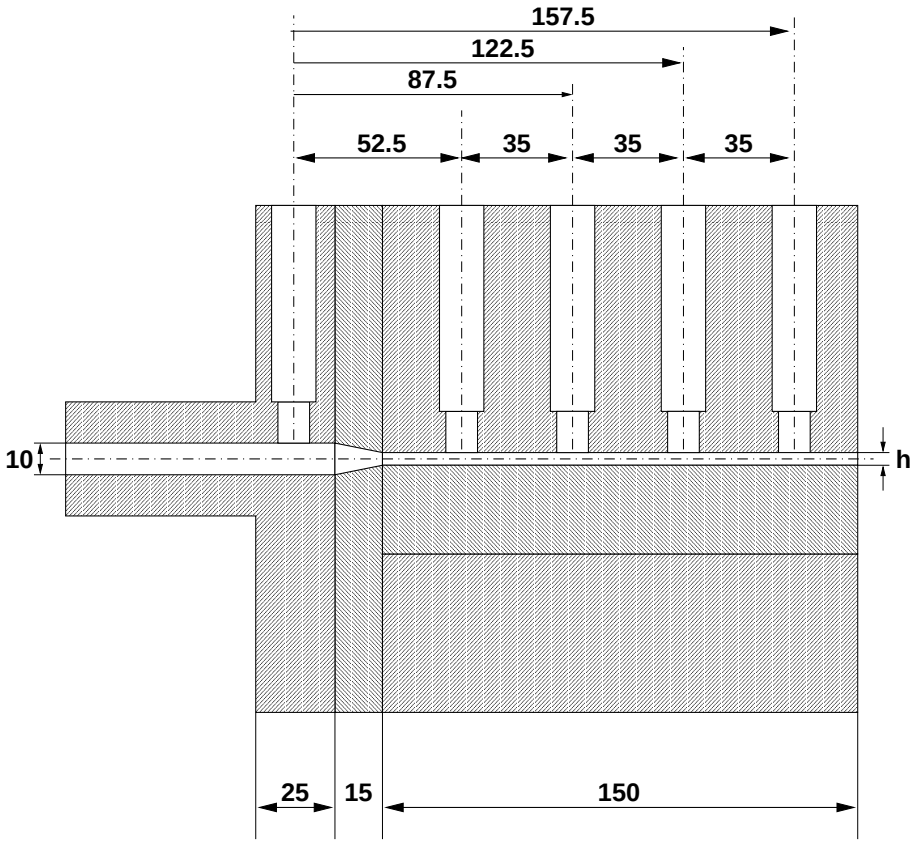

Figure 3.2: Rheometer dimensions and sensor locations (side view)

Using multiple pressure transducers in order to determine the pressure profile along the die allows for separation of entrance and exit effects. End correction, as used in Bagley's procedure, is therefore not required.
The use of a slit die offers several advantages when compared to capillary rheometers. First, a slit die represents a typical flow channel as encountered in injection molding [169]. It also offers a higher degree of freedom for fiber orientation since the width of the channel is larger than the initial fiber length. Pressure holes are avoided and flow is less disturbed since a plane channel and transducers with flat tips are used [47].
On the other hand, there are several drawbacks associated as there is the effect of finite slit width and slit corners as well as the rearrangement of the velocity field near the exit of the die [24]. Slit flow is more complex and more expensive than capillary flow [26].
Cavities with different gap height (h = 1, 2 and 3 mm) and width (w = 25 mm and 18 mm) were used. Two different contraction ratios (2:1, 3:1) were employed in order to determine extensional viscosity (s. fig 3.3).

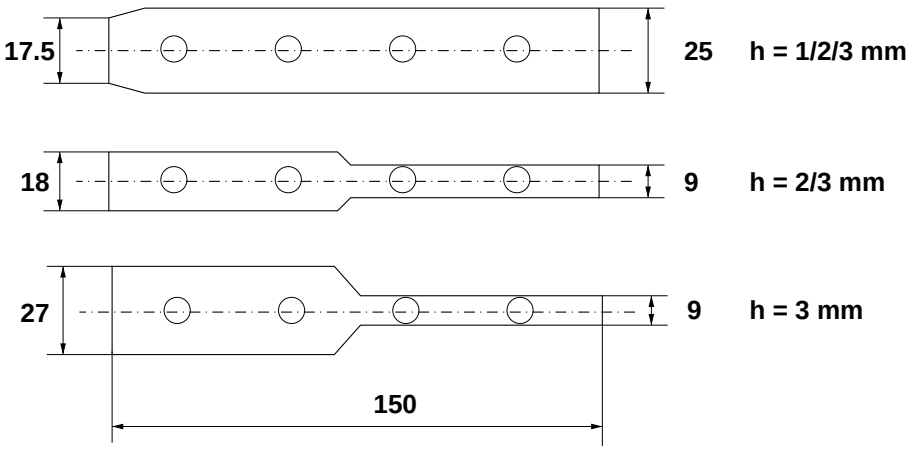

Figure 3.3: Dimensions of cavities and sensor positions (top view)

3.1.2 Sensors

3.1.2.1 Pressure transducers

The extrusion pressure sensor (KISTLER, s. table 3.1) contains a silicon measuring element which operates according to the piezo-resistive principle. Since this measuring element operates reliably even at high temperatures, it can be fitted directly behind the diaphragm, so that no pressure transmitting medium such as a push rod, oil or mercury is required. The diaphragm can be made much thicker and therefore more rugged without compromising accuracy or repeatability. Due to the rugged diaphragm it can be used in very abrasive processes where highly filled materials are processed. The solid-state design leads to an extremely high natural frequency allowing transient pressure changes to be captured. Very accurate results due to of digital compensation can be obtained.

operating temperature range	$T[^o$C]	25 - 300
maximum temperature	$T_{max}[^o$C]	350
operating pressure range	p [MPa]	0 - 25 (100)
maximum pressure	p_{max} [MPa]	150
response time	t [ms]	$<$3.3
natural frequency	f [kHz]	$>$100

Table 3.1: Extrusion sensor, 4090B, KISTLER

Unlike a strain gauge sensor a piezo-resistive sensor is capable of measuring ambient temperature as well as pressure simultaneously. Temperature is determined by the drift of the measuring bridge, where the voltage for compensation is related to the increase in temperature. Depending on the position in the cavity, sensors with different maximum pressure operating range (250 to 1000 bar) were used in order to obtain reliable results.

3.1.2.2 Infrared Sensor

3.1.2.2.1 Fundamentals

Temperature measurement using an infrared (IR) sensor is based on the detection of electromagnetic radiation that is emitted due to the brownian motion of molecules. The energy per time, area and spectral range, i.e. the spectral radiation density $L_{\lambda,b}$, which is is emitted normal to the surface of a black

body can be determined using Planck's radiation law. The spectral radiation of any arbitrary body, M_λ, is derived from the spectral radiation of the black body $M_{\lambda,b}$ (s. fig. 3.4) multiplied by the emissivity ϵ:

$$M_\lambda = M_{\lambda,b} \cdot \epsilon(\lambda, \vartheta) = \pi \cdot L_{\lambda,b} \cdot \epsilon(\lambda, \vartheta) = \frac{c_1}{\lambda^5 \left(e^{\frac{c_2}{\lambda \vartheta}} \right) - 1} \cdot \epsilon(\lambda, \vartheta) \qquad (3.1)$$

with $h = 6.626 \cdot 10^{-34}$ Js , $k = 1.381 \cdot 10^{-23}$ J/K, respectively, $c_0 = 2.9979 \cdot 10^8$ m/s, $c_1 = 2\pi h c_0^2 = 3.7418 \cdot 10^{-16}$ W/m^2 and $c_2 = h c_0 / k = 1.4388 \cdot 10^{-2}$ m/K.

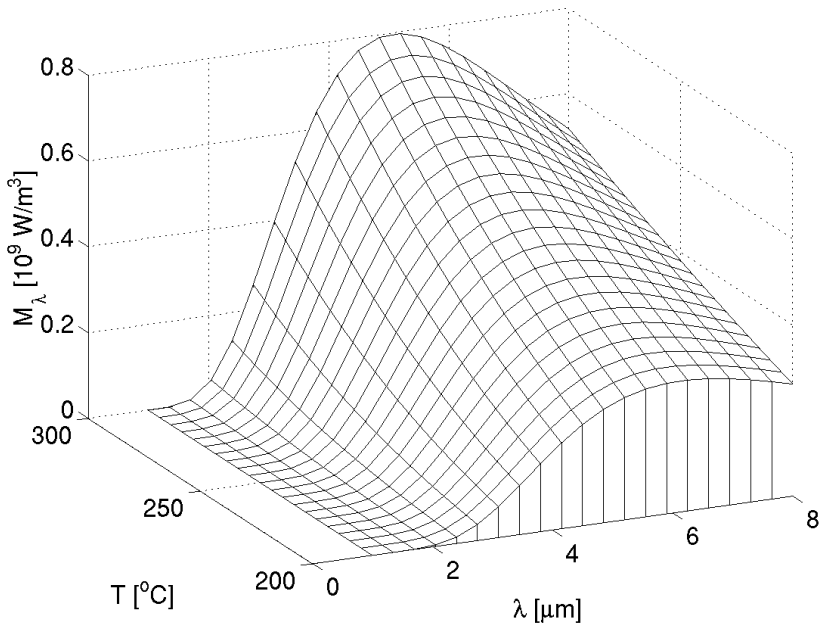

Figure 3.4: Spectral radiation of a black body

In the typical plastics processing range from 200^{o}C to 300^{o}C, the largest fraction of radiation is emitted between 4 and 8 μm.
The wavelength at which the radiation reaches a maximum is shifted from 6 μm to 5 μm with an increase in temperature from 200^{o}C to 300^{o}C. The inverse proportionality between the position of the maximum of radiant intensity and absolute temperature ϑ can be expressed using Wien's law:

$$\lambda_{max} = \frac{\alpha}{\vartheta} \tag{3.2}$$

with $\alpha = 2.898 \cdot 10^{-6}$mK. The penetration depth of radiation has been evaluated experimentally for PP-LGF (s. fig. 3.5) from transmission spectra (appendix A) using an infrared spectrometer (NICOLET). The penetration depth is defined as distance where the intensity of radiation is reduced to 1/e (36.8%).

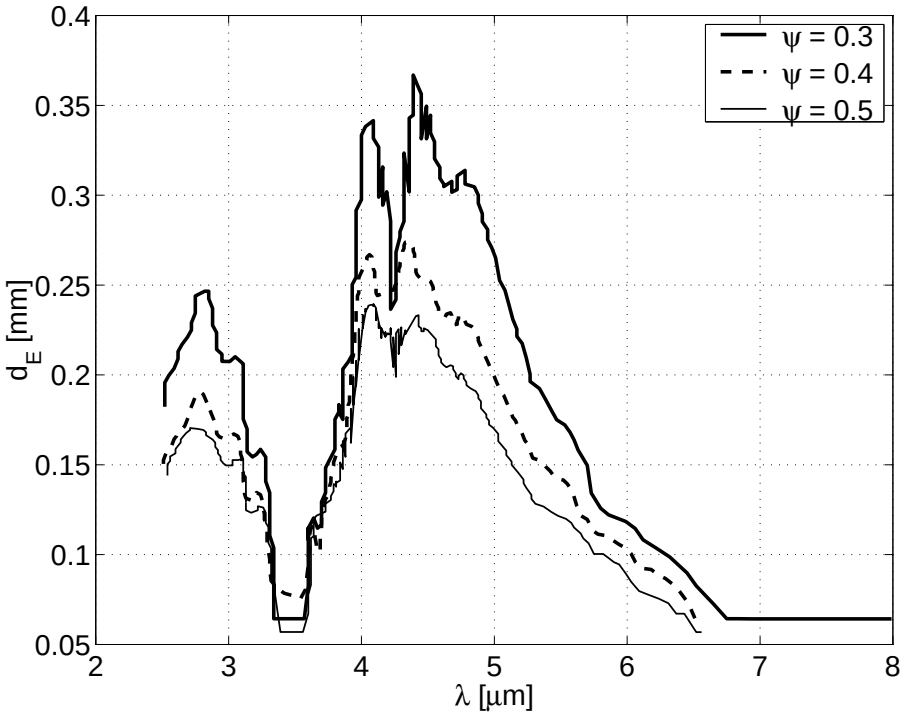

Figure 3.5: Penetration depth for PP vs. fiber fraction

The maximum penetration depth is observed between 4 and 5 μm, where radiation also reaches highest values (s. fig. 3.4). When the fiber fraction is varied from 30% to 50%, the penetration depth decreases from 0.37mm to 0.23mm.

3.1.2.2.2 Principle of Infrared Sensors

When measuring with radiation thermometers, it is essential to know where and from which depth the radiation is originating. IR sensors yield weighted values of the temperature of a defined control volume. The radiation does not only come from the surface, but also from deeper layers since plastics are penetrable for radiation in the near infrared range. Depending on the absorption coefficient μ of the melt, the radiation from the opposite wall and reflected fractions originating either from the probe or the wall can add a significant amount to the total radiation measured by the IR sensor [170].
The heat radiation emitted by the melt enters the sensor through a wear-resistant sapphire window and is converted into an electrical signal by a detector located in the sensor connection head. The range of application, e.g. bandwidth of wavelength, is limited by the type of sensor. Sensors generally differ by the optical components and the method how the radiation is transferred from the sapphire window to the detector.
Most sensors use fiber-optics, e.g. quartz glass fibers, for the transmission of radiation which limits the maximum wavelength to 4 μm (s. fig. A.2). A large portion of the radiation is neglected and measuring takes place in the region with steepest slope and therefore errors are likely to rise. In addition, no continuous signal is obtained since light detective resistance measurement (LDR) is applied.
The sensor applied in this study contains a sapphire window, a polished tube and a sapphire lens. The maximum detectable wavelength is only limited by the transmission of the sapphire window and yields a bandwidth of 0.18 to 7 μm. The detector itself has an operating range from 0.4 to 15 μm.

3.1.2.2.3 Application

The use of IR sensors allows for continuous temperature measurement at elevated temperature levels and high pressure (s. table 3.2). The flat tip of the sensor avoids interference with the cavity.

operating temperature range	T [^{o}C]	50 - 400
maximum temperature	T_{max} [^{o}C]	600
maximum pressure	p_{max} [MPa]	100
response time	t [ms]	15

Table 3.2: IR sensor, IR THERM 2001, FOS Messtechnik GmbH

The infrared measuring method with a response time of the sensor less than 15 ms is much faster than conventional thermometers and therefore capable of detecting changing melt temperatures and temperature peaks. IR sensors are typically calibrated for a black radiator with $\epsilon = 1.0$ and need to be re-calibrated depending on the optical properties of the melt. For this purpose, the sensor used in this study possesses a built-in thermocouple for on-line calibration. Time consuming external calibration [171] is not necessary.

3.1.3 Rheometry

3.1.3.1 Materials

Rheological characterization of neat polypropylene (Montell H39S) was performed. Further, polypropylene cylindrical pellets, reinforced by E-Glass fibers aligned along the cylindrical axis with an initial length of 10mm (FACTOR-PP, FACT GmbH) were used. With a weight fraction of 30%, 40% and 50%, fiber volume fraction yielded 13%, 19% and 26%, respectively.
In the case of the 50% reinforcement, the influence of sizing of the fibers on the bulk viscosity was studied using a special sizing for polypropylene and a standard sizing for thermoplastics. The effect of fiber length on rheological properties was examined by comparing the standard material to pellets with an initial fiber length of 12mm at a fiber fraction of 30% (DSM).

3.1.3.2 Procedure

The pellets were processed within a nominal temperature range from 220^{o}C to 270^{o}C. The melt was injected after a holding time of 30s with a maximum pressure of 1350 bar at 8 different flow rates (Q = 5 to 180 cm^3/s) with logarithmic spacing. 5 injections with a shot volume of V = 105 cm^3 per setup were performed.

3.1.3.3 Data Acquisition

Pressure and temperature signals were sampled at a rate of 100 Hz using a Data Acquisition Board (max. 16 channels, 250 kHz) and LABVIEW (both National Instruments) running on Windows NT. The signals were stored in ASCII type format on the local hard disk and then transferred via LAN for further processing.

3.1.3.4 Data Analysis

Signal processing is required for peak detection of both temperature and pressure. The maximum and average values during each injection were calculated and then again averaged over 5 injections. In contrast to short fibers, where flow is stabilized by the presence of fibers, a variation in pressure up to 30%, especially at higher fiber fraction is reported in previous studies using capillary rheometers [35, 37, 38], due to temporary fiber blockage or jamming at the entry. In this study, the maximum variation in pressure accounts for up to 20%, even at highest shear rates (fig. 3.6).

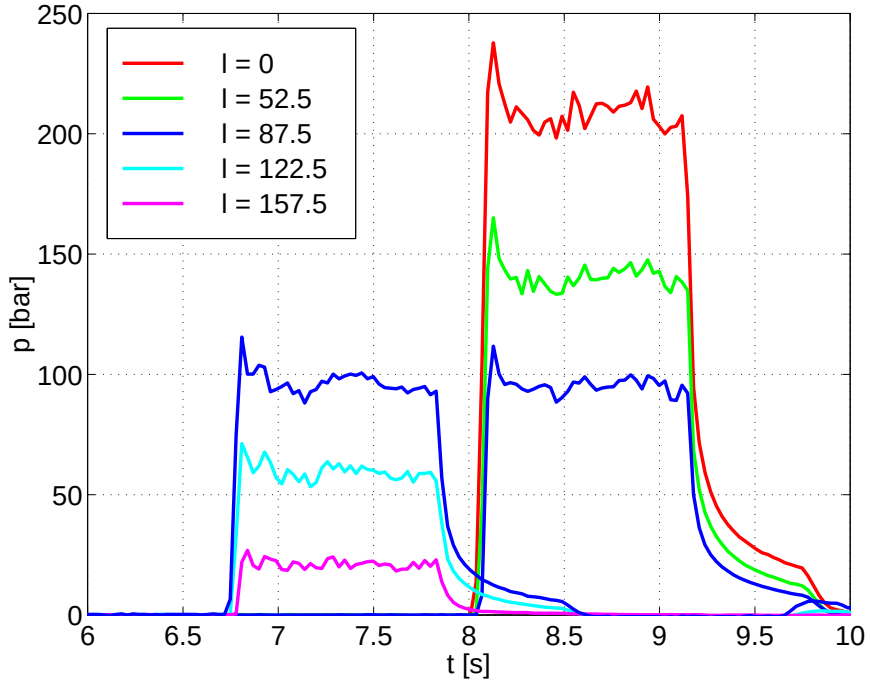

Figure 3.6: Pressure signal versus sensor location, Q = 180 cm^3/s

A graphical user interface (MATLAB) was designed for signal processing of pressure and temperature, data analysis for calculating pressure drop, shear stress, shear and extensional viscosity for both linear and parabolic pressure profiles and visualization of these quantities depending on materials, channel geometry and processing parameters.

3.2 Pressure Profile

3.2.1 Pressure Drop

The pressure profile along the cavity is depicted for neat and filled PP in figs. 3.7 and 3.8. The exit is located at z = 0. Assuming a linear profile based on the 3 sensors close to the exit provides a good fit to the experimental values.

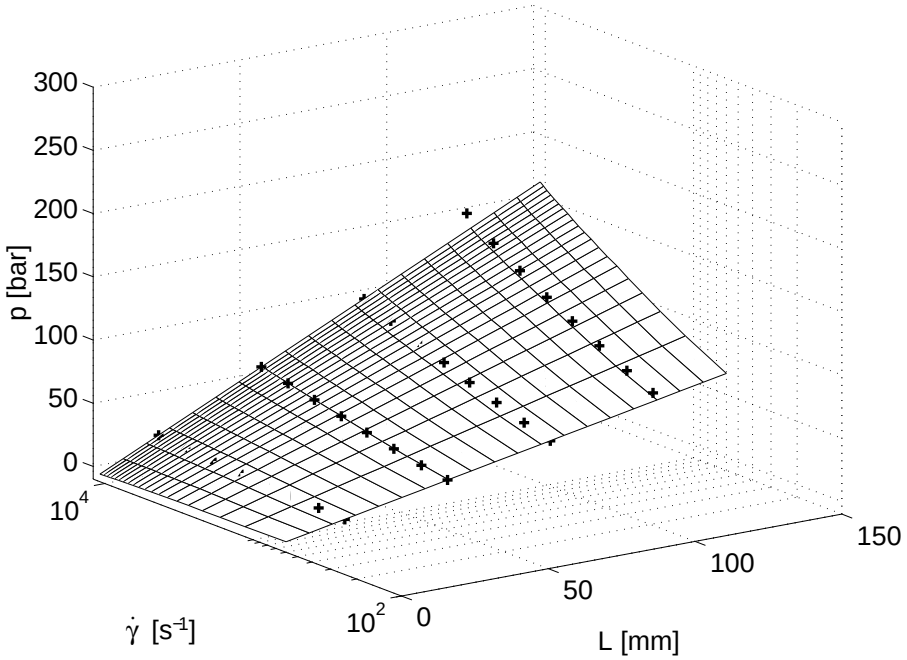

Figure 3.7: Pressure drop, PP, 250^{o}C

At the entrance, the experimental values deviate from this linear profile suggesting entrance effects [172]. Non-linear pressure profiles with a curvature upwards could be caused either by a strong dependence of viscosity on pressure, due to viscous heating [75, 81] or insufficient die length [172]. Convex curvature occurs due to pressure dependent slip at high shear stresses [173].

Previous work by Mutel [43] on PP exhibited linear profiles for both neat and filled PP with variations less than 1% but non-linearity increased with cavity height. It was therefore suggested, that the distance between the entrance and the first pressure sensor should be greater than 20 times the height of the cavity in order to assure fully developed flow. Crowson [28] obtained non-linear Bagley plots for neat PP and assumed the presence of this effect to be due to the dependence of viscosity on pressure.

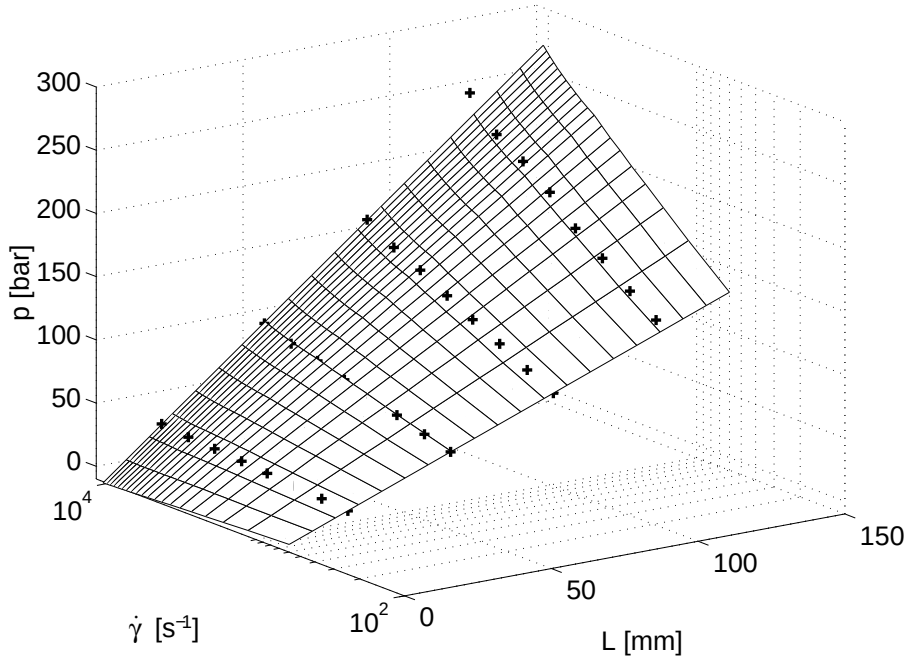

Figure 3.8: Pressure drop, PP-LGF50, 250^{o}C

3.2.2 Exit Pressure

The exit pressure drop is due to the viscous loss in the vicinity of the exit, caused by the re-arrangement of the velocity field. For both linear and parabolic interpolation between the three sensors located closest to the exit, the extrapolation of the pressure profile yields negative values for the exit pressure drop Δp_{exit}. The pressure at the exit should be equal to zero.
For neat PP, the exit pressure loss is increasing with shear rate from 1% to 3% of the total pressure drop. With increasing melt temperature, the exit pressure loss is slightly declining. With increasing fiber fraction, the amount of exit pressure loss is yielding a greater share of the overall pressure drop. Gibson [45] observed an exit pressure loss two orders of magnitude higher for filled PA compared to neat PA in capillary flow. In this work, an exit pressure loss of 3% to 5% was observed for PP-LGF50. Based on these results, the assumption of a linear pressure profile was confirmed and the exit pressure loss was considered to be negligible.

3.2.3 Entrance Pressure

At the transition from the circular cross-section to a rectangular shape in the adapter of the rheometer, entrance pressure loss is observed. The amount of entrance pressure drop is calculated from the difference between total pressure drop and pressure drop derived by extrapolating the linear pressure profile between the three sensors located closest to the exit of the cavity to the sensor located close to the gate.
Entrance pressure loss is only due to viscous dissipation. In capillary rheometry, entrance pressure loss can account for half of the total pressure drop, as observed by Gibson [45]. The entrance pressure loss Δp_E slightly increases with melt temperature. Obendrauf [52] measured entrance pressure loss for 6 different types of PP. Δp_E, increasing with molecular weight, differed by one order of magnitude.

As observed earlier by Crowson [28], increasing entrance effects with fiber fraction were found (s. fig 3.9). While for neat PP, the entrance pressure loss yielded between 8% to 10% of the total pressure drop, Δp_{ent} was found to be 10% to 11% for PP-LGF50. However the entrance pressure drop declined with increasing shear rate affirming the statement of Gibson [45], that the the entrance pressure drop reduces with increasing orientation in the skin zone of the melt.

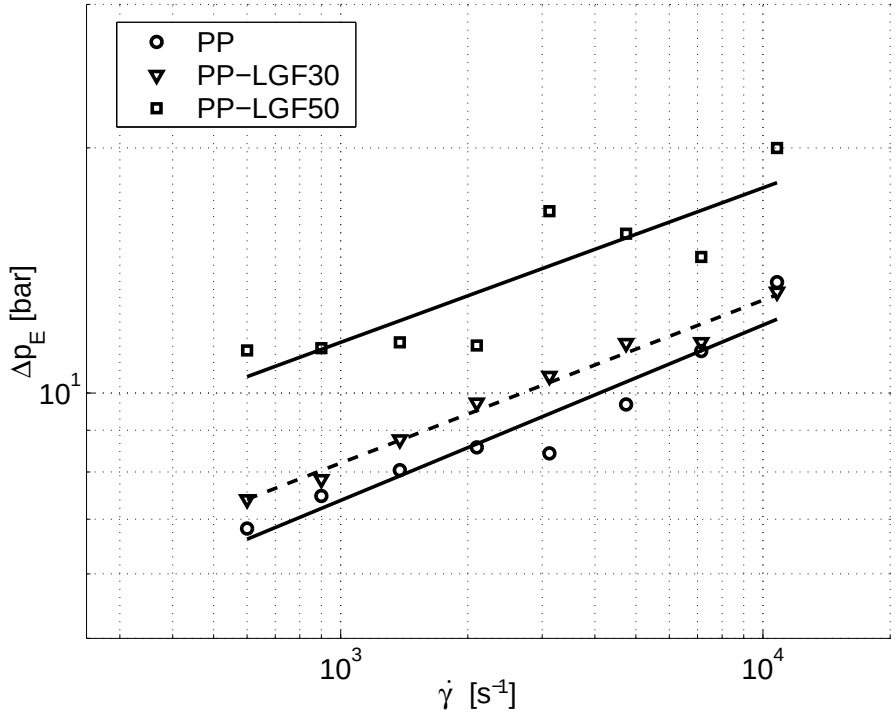

Figure 3.9: Entry Pressure drop vs. fiber fraction, T = 250^{o}C

3.3 Shear stress

From the pressure drop, measured at various shear rates, shear stress is derived from eqn. 2.7 using the correction for cavity dimensions (eqn. 2.10). For different slit heights, the values for shear stress depicted in fig. 3.10 were obtained.

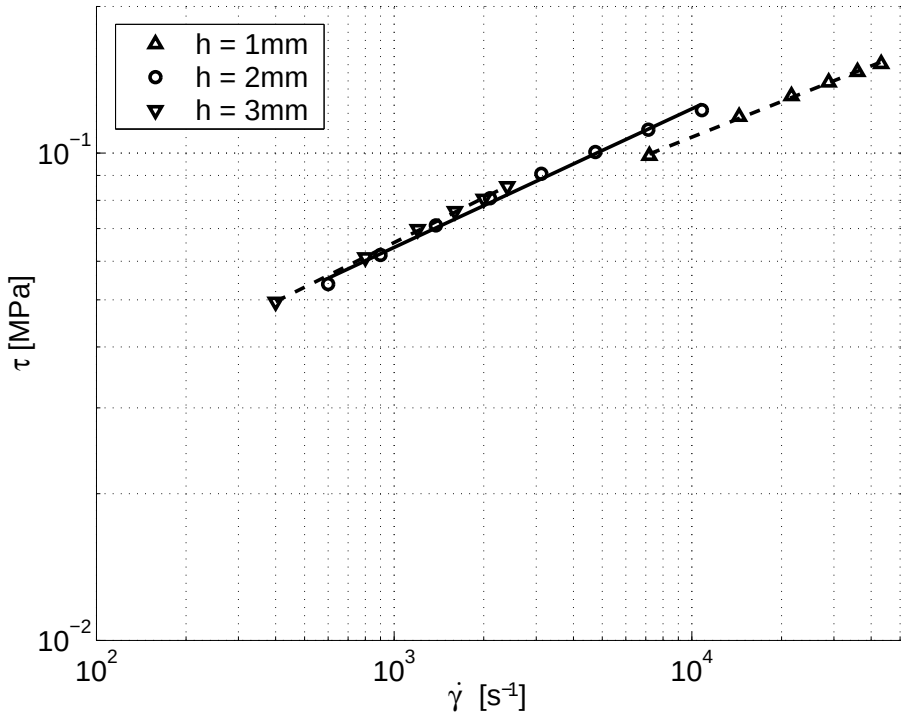

Figure 3.10: Shear stress, PP, T = 220^{o}C

With the combination of cavities mounted on the injection molding machine, true shear rates ranging from 400 to 40000 s^{-1} were obtained. Shear stress yields values of up to τ = 0.1MPa at which melt fracture is likely to occur.
The results derived using the cavities with a height of 2mm and 3mm, respectively, yield similar values. However, the results measured using the slit with a height of 1mm differ significantly and will not be used for further considerations limiting the validity of experimental results to a range of shear rate between 400 to 10000 s^{-1}.

The addition of fibers ($\psi = 0.5$) nearly doubles the values obtained for shear stress, as depicted in fig. 3.11. The slope of the stress curves versus shear rate becomes less steeper and the deviation from a linear curve becomes more pronounced for fiber filled PP.

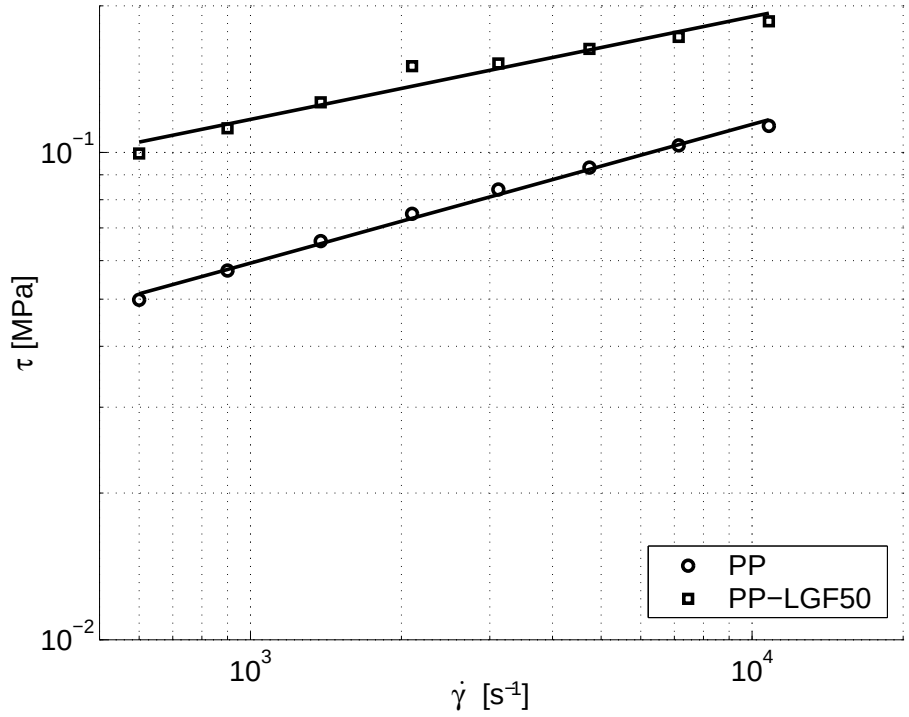

Figure 3.11: Shear stress versus fiber fraction, h = 2mm, T = 220^{o}C

From shear stress, shear viscosity was calculated and non-newtonian flow behavior accounted using the correction by Weissenberg and Rabinovich (eqn. 2.11). Therefore all plots of shear viscosity depict true shear viscosity including correction for channel dimensions and non-newtonian behavior versus true shear rate.

3.4 Viscosity

3.4.1 Influence of processing parameters on viscosity

3.4.1.1 Rate of deformation

The extensional viscosity of long fiber reinforced polypropylene, λ, was found to be 60 times higher than shear viscosity (s. fig. 3.12). In agreement with previous studies on long fiber reinforced thermoplastics [31, 46, 174, 175], a power-law type relation shows good agreement with results for both shear and extensional viscosity in the evaluated range of deformation rates.

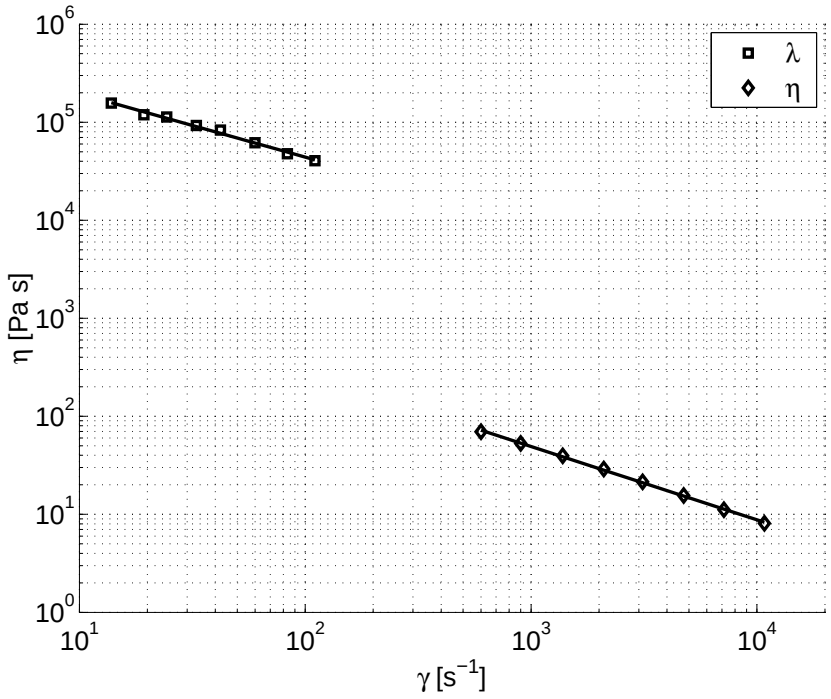

Figure 3.12: Shear and extensional viscosity, PP-LGF50, 250^{o}C

Thinning with rate of deformation is more pronounced in shear flow, since the slope of the curve is steeper for shear viscosity compared to extensional viscosity. With increasing shear rate from $10^3 s^{-1}$ to $2{\cdot}10^4 s^{-1}$, viscosity of PP-LGF50 declines by 90%.

3.4.1.2 Temperature

As depicted in fig. 3.13, shear viscosity of neat PP is a strong function of temperature. Increasing the temperature from 220^{o}C to 235^{o}C reduces shear viscosity by 7%. Further increase in temperature to 270^{o}C yields a reduction in shear viscosity in the order of 20%.

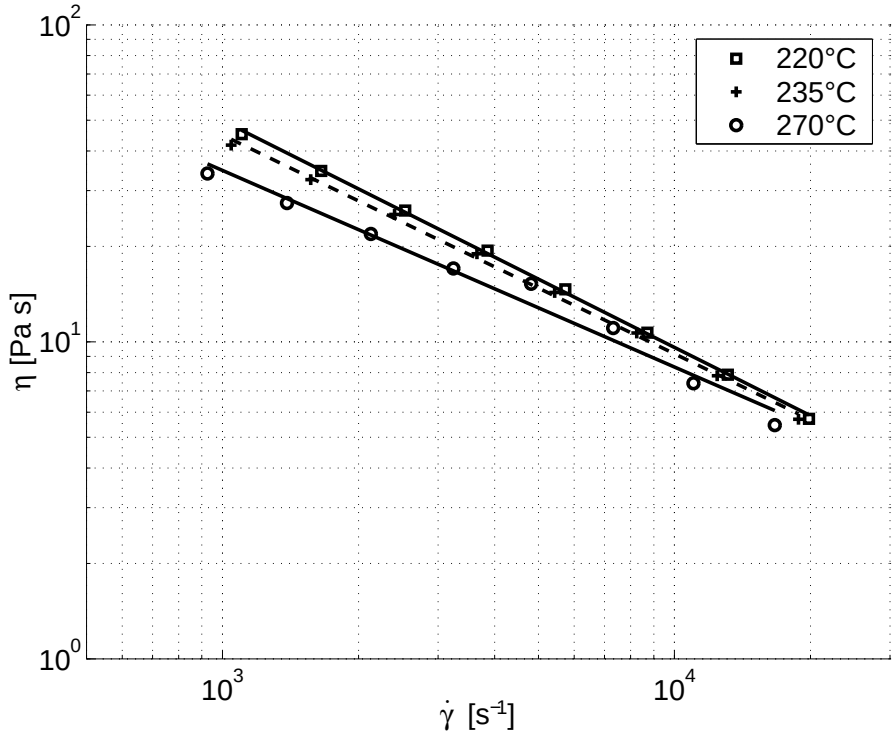

Figure 3.13: Shear viscosity vs. temperature, PP

From literature, only a few number of studies carried out at different temperature levels are known since each polymer grade has a recommended processing temperature.

Crowson [29] evaluated the shear viscosity of glass fiber reinforced PP with respect to melt temperature, fiber fraction and fiber length. For neat PP, he observed a reduction in viscosity of 60% with a melt temperature increasing from 180^{o}C to 270^{o}C.
For PP with a fiber mass fraction of 50%, as depicted in fig. 3.14, the effect of temperature on shear viscosity is still present. However, the temperature dependence of shear viscosity becomes slightly more pronounced with fiber fraction. For instance, an increase in temperature from 220^{o}C to 235^{o}C or 270^{o}C induces a reduction in viscosity by 8% and 25% respectively. Similar behavior of short fiber reinforced PP with a mass fraction of 20% was found by Crowson.

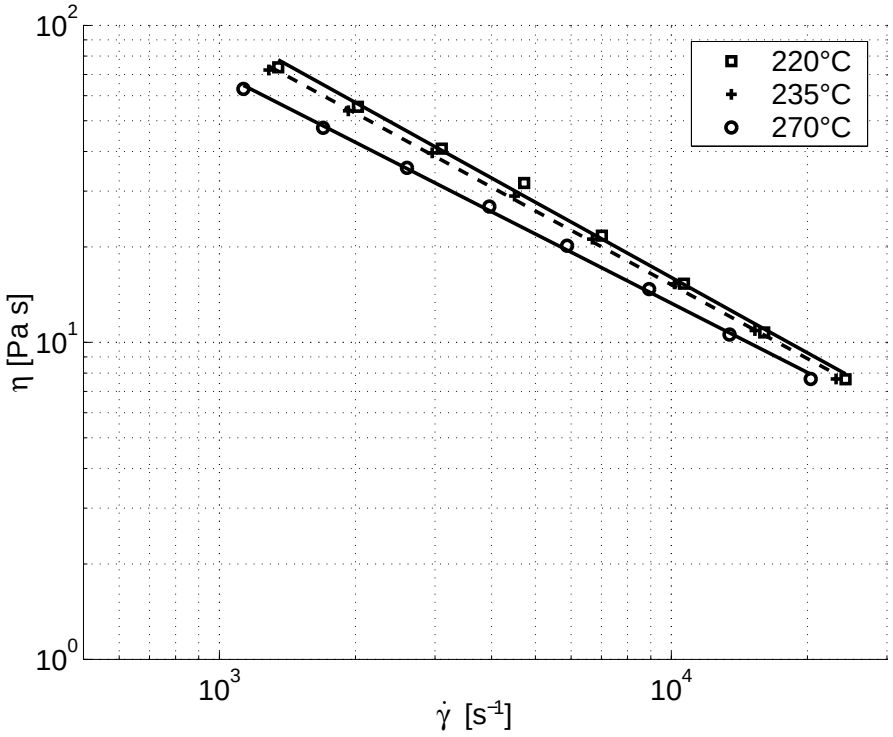

Figure 3.14: Shear viscosity versus temperature, PP-LGF50

The extensional viscosity of PP-LGF50 (fig. 3.15) is also affected by melt temperature. With an increase in temperature from 220^{o}C to 235^{o}C and 270^{o}C, the extensional viscosity declines by 7% and 21%, respectively.

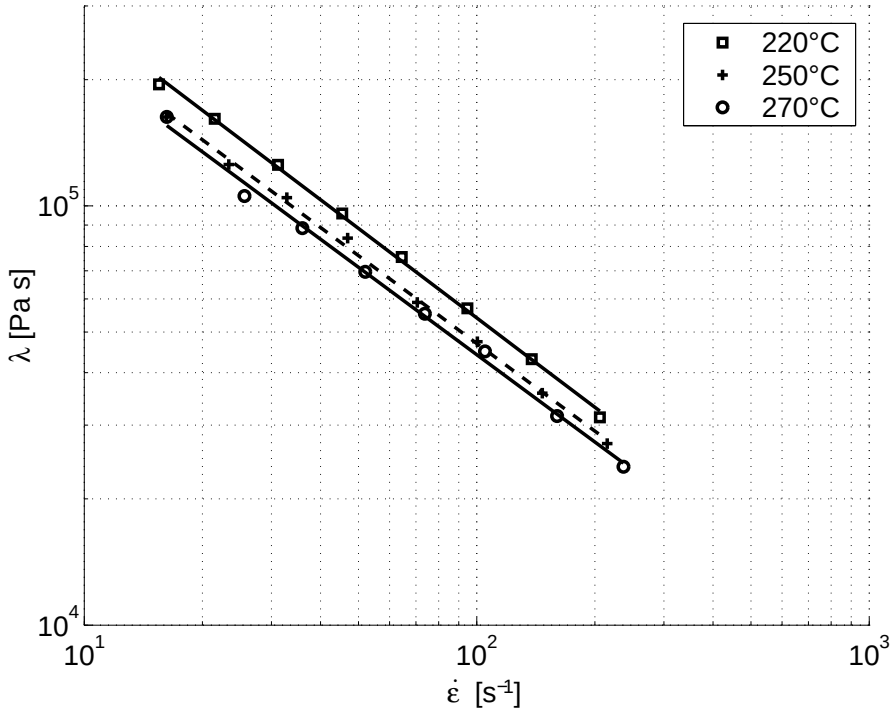

Figure 3.15: Extensional Viscosity versus temperature, PP-LGF50

With decreasing fiber fraction, the temperature dependence of extensional viscosity is also declining. For instance, the same temperature variation from 220^{o}C to 235^{o}C and 270^{o}C, causes a decrease in extensional viscosity of PP-LGF30 in the order of 3% and 10%, respectively.

3.4.1.3 Pressure

At elevated strain rates ($\dot{\gamma} > 10^3$ s^{-1}), viscosity strongly depends on pressure which drives the flow [176]. Carter [177] found, that the viscosity of polypropylene doubled with an increase of the hydrostatic pressure from 0 to 60MPa. Binding [178] examined the dependence of shear and extensional viscosity of neat thermoplastics within a range of deformation between 50 and 2500 s^{-1} and a pressure range from 1 to 70MPa. It was found that the dependence of viscosity, especially extensional viscosity, for PP is greater than for PE but less pronounced than for PS. Based on a power-law type relation between viscosity and pressure,

$$\eta = \eta_0 \cdot e^{\alpha_\eta \cdot p} \qquad \lambda = \lambda_0 \cdot e^{\alpha_\lambda \cdot p} \tag{3.3}$$

Binding [178] derived the values for pressure coefficients for both shear and extensional viscosity of neat PP as listed in table 3.3.

T [^{o}C]	α_η [1/GPa]	α_λ [1/GPa]
190	7.6	19.3
200	6.4	17.9
230	6.9	15.5

Table 3.3: Pressure coefficient for shear and extensional viscosity of neat PP

The dependence of viscosity appeared to be insensitive to changes in temperature. However, Binding's results are in good agreement with Crowson [36] who found similar values for neat PP (α_η = 5.8 1/GPa). With the setup used in this study, the results listed in table 3.4 were obtained. Generally, the results are in agreement with Binding's and Crowson's results. However, α_η rises with temperature but decreases with fiber fraction.

α_η [1/GPa]	T[^{o}C]			
ψ [%]	220	235	250	270
0	5.60	7.17	10.42	10.62
30	3.99	4.95	6.22	8.07
40	4.31	5.05	5.96	5.94
50	3.60	3.83	4.59	4.98

Table 3.4: Pressure coefficient for shear viscosity of fiber reinforced PP

3.4.2 Materials

3.4.2.1 Fiber fraction

A substantial increase in shear viscosity with the addition of long fibers is observed at low shear rates, as depicted in fig. 3.16. Shear thinning at high rates of deformation becomes more significant with increasing fiber fraction. For instance, the power-law coefficient n decreases from 0.28 for neat PP to 0.24 for PP-LGF50. The effect of fiber fraction on shear viscosity becomes less pronounced with increasing temperature.

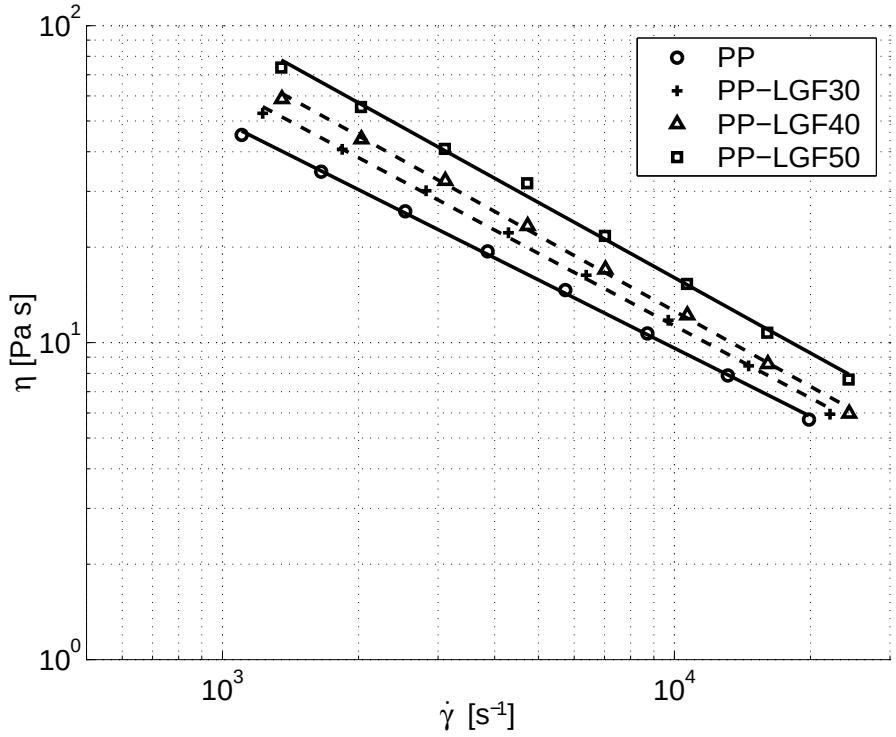

Figure 3.16: Shear Viscosity vs. fiber fraction, 220^{o}C

For neat PP, the extensional viscosity could not be derived since the entrance pressure drop was too low using the current setup. However, varying fiber mass fraction from 30% to 50% (fig. 3.17) yields an increase in extensional viscosity in the order of 55%.

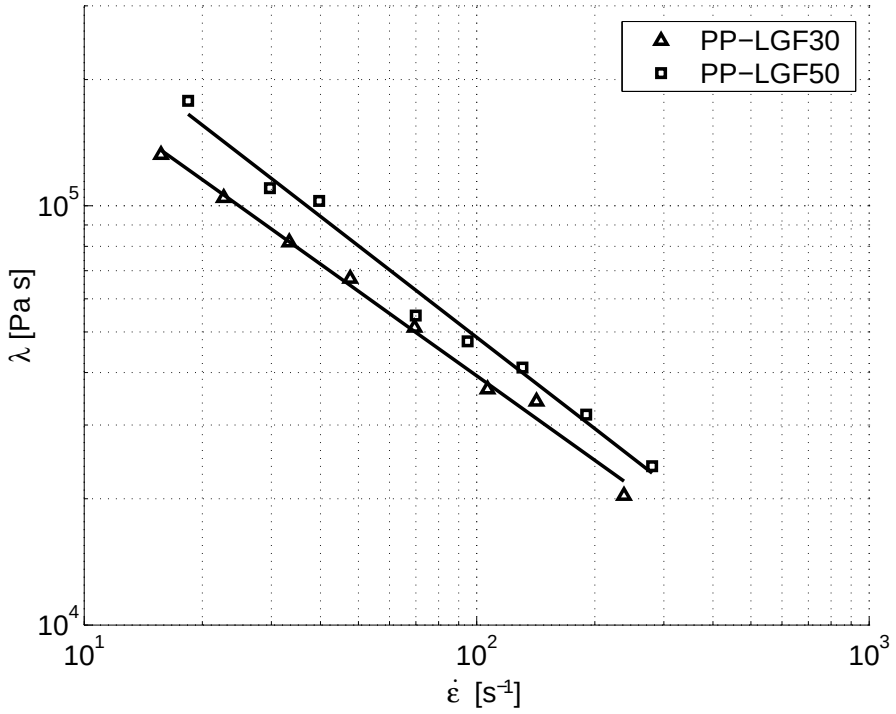

Figure 3.17: Extensional Viscosity vs. fiber fraction, 220^{o}C

As observed for shear viscosity, the difference in extensional viscosity for different fiber fractions decreases at elevated melt temperature. The thinning behavior with rate of extension is not as pronounced for extensional flow as in shear flow and does not vary significantly with fiber fraction. The power-law coefficient for extensional viscosity ranged from 0.31 to 0.3.

3.4.2.2 Fiber length

A substantial growth in shear viscosity was found with increasing initial fiber length from 10mm to 12mm, as depicted in fig. 3.18. Reflecting the results obtained at different values for melt temperature, an average increase in shear viscosity by 50% is observed at low shear rates. Shear-thinning is more pronounced while the temperature dependence of viscosity remains unchanged. In literature [29], an increase by a factor of four was found at low shear rates when fiber length was altered from 5mm to 20mm. While virtually no difference is found for a shear rate above 100 s^{-1}, PP filled with shorter fibers tends to newtonian flow behavior at low shear rates.

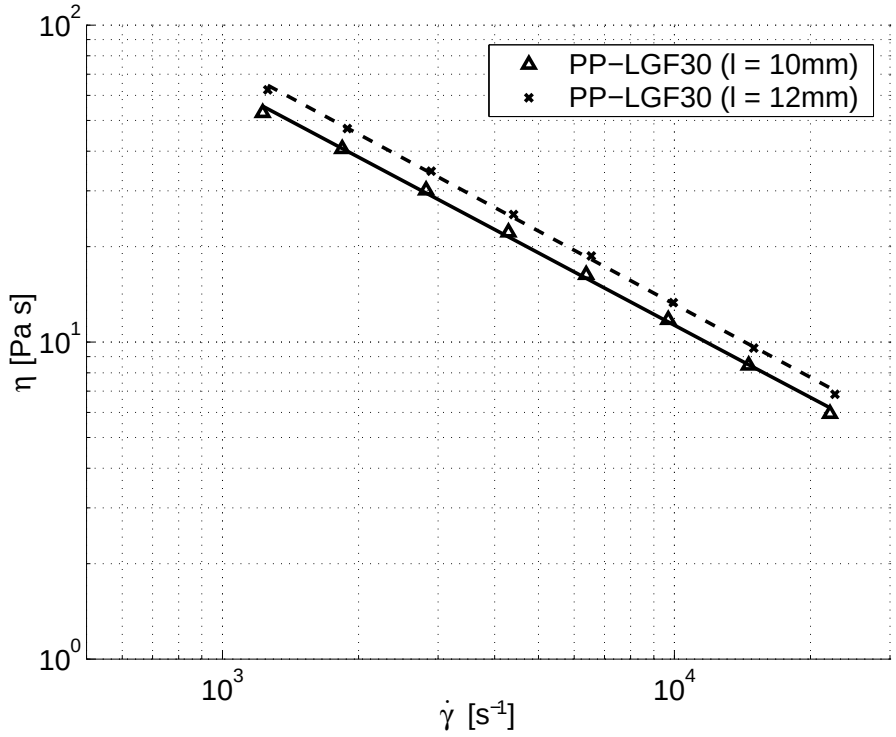

Figure 3.18: Viscosity vs. Fiber length, PP-LGF30, 220^{o}C

In previous studies [30], it was observed that the shear viscosity also depends on fiber length distribution. A broad distribution yields higher values of shear viscosity.
The difference in extensional viscosity almost diminishes if the fiber length is increased from 10 to 12mm. In earlier work [30], an increase of 50% and 170% was derived for PP-LGF with an increase in initial fiber length from 5mm to 6mm and 10mm, respectively.

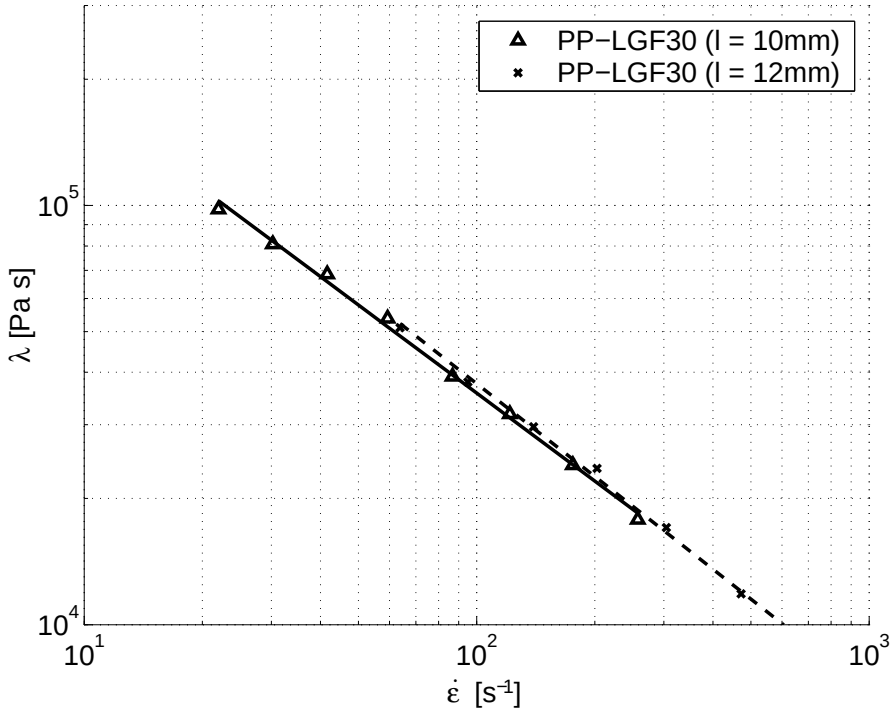

Figure 3.19: Extensional Viscosity vs. Fiber length, PP-LGF30, 220^{o}C

3.4.2.3 Sizing

For long fiber reinforced PP, a difference in shear viscosity was observed depending on the surface treatment of the glass fibers. A standard silane sizing of the glass fibers for thermoplastics leads to significantly lower values when compared to a sizing optimized for PP (fig. 3.20). At low shear rates, the difference is approximately 20%. Again, the difference reduces at higher shear rates but not as rapid as observed when varying fiber fraction.

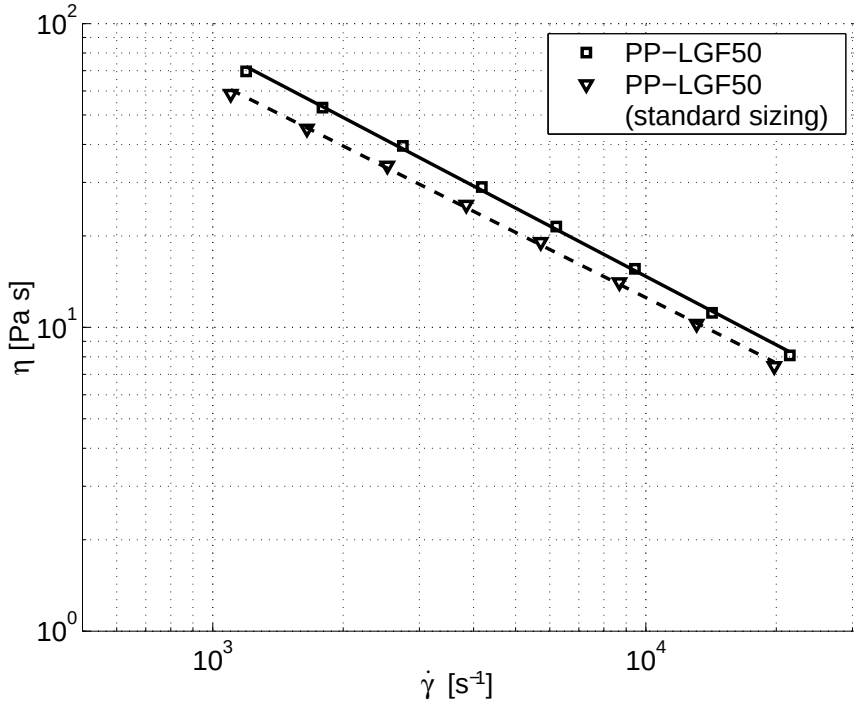

Figure 3.20: Shear Viscosity vs. Sizing, PP-LGF50, 220^{o}C

While the dependence of flow properties on the finish of fibers has received little attention, the sensitivity of mechanical properties of glass fiber filled polypropylene on the composition of coupling agents has been reported. For example, the bending strength of PP-GF with a standard silane finish of the glass fiber is less than half of that obtained by surface treatment of the fibers with silane modified with maleic-anhydride [179].

The effect of fiber sizing on extensional viscosity is depicted in fig. 3.21. Evaluating the values for extensional viscosity derived at different levels of melt temperature, an optimized fiber sizing yields an increase by one third when compared to PP-LGF50 with a standard finish of the glass fibers.

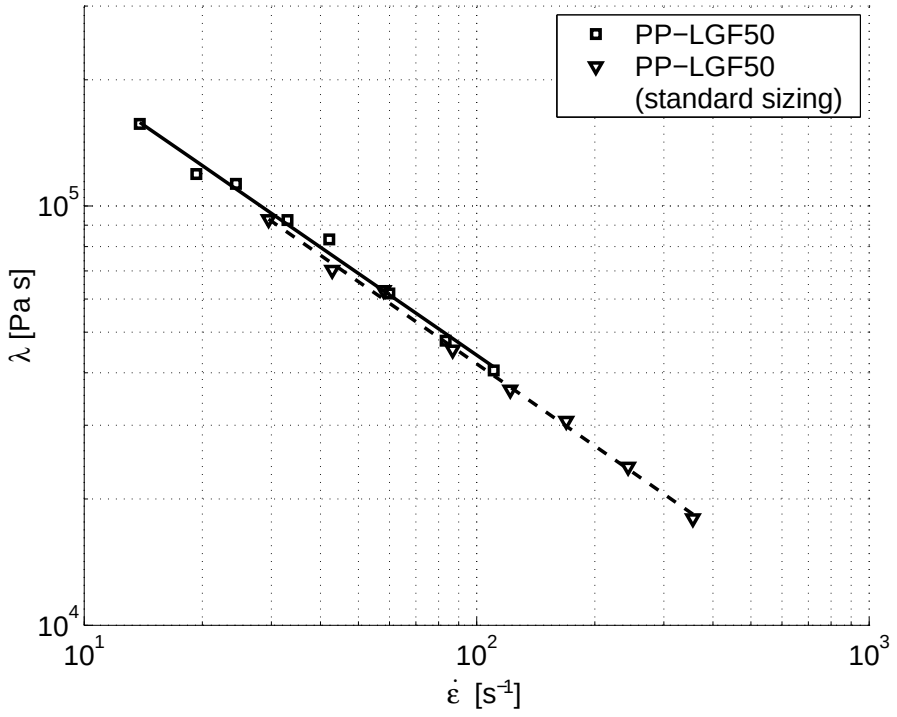

Figure 3.21: Extensional Viscosity vs. Sizing, PP-LGF50, 250^{o}C

3.4.3 Channel geometry

3.4.3.1 Slit flow versus capillary flow

In order to evaluate the influence of rheometer type and channel dimensions, the shear viscosity of neat PP measured using the slit die were validated versus the results obtained using a capillary rheometer (L = 30mm, D = 1mm). As depicted in fig. 3.22, good agreement in apparent shear viscosity is found in the evaluated range of shear rate.

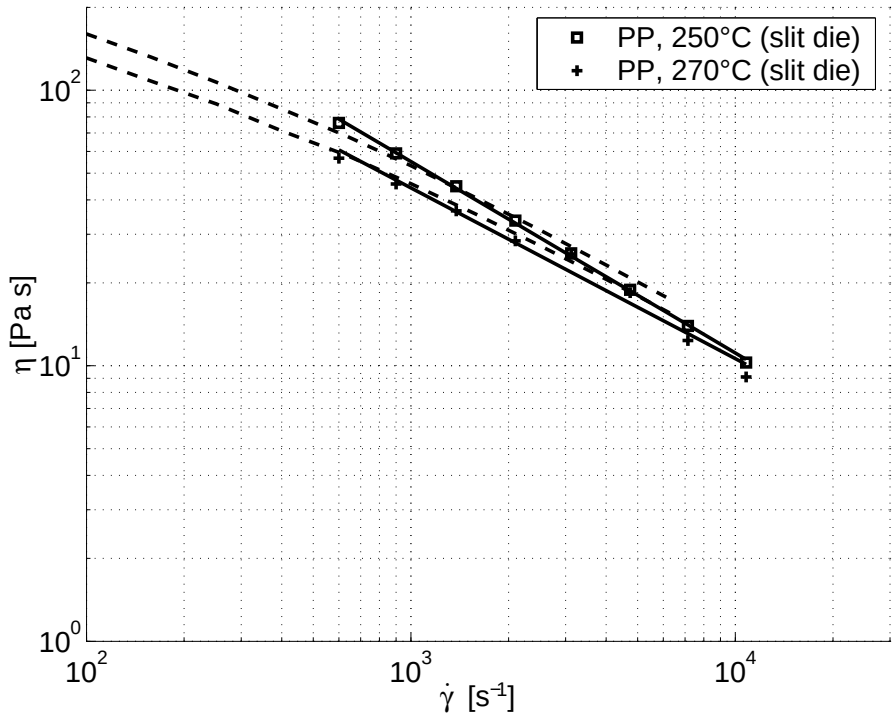

Figure 3.22: Shear Viscosity of PP at 250 and 270 ^{o}C, capillary versus slit die

From capillary rheometry it is observed, that the curves for 250 and 270 ^{o}C remain parallel and that shear viscosity deviates from a power-law behavior for shear rates below 500s^{-1}. Shear viscosity obtained using the slit die yields lower values than those derived from capillary rheometry. At higher shear rates, the curves appear to yield similar values implying a higher degree of shear-thinning.

3.4.3.2 Channel height

While there was virtually no difference between the results obtained using slit dies with different height for neat PP, higher values for shear viscosity with increasing channel height were found for fiber filled PP (fig. 3.23). For instance, the shear viscosity of PP-LGF40 increases by roughly 8% when varying the cavity height from 2mm to 3mm.
In capillary rheometry, shear viscosity was found to increase by approximately 10% when decreasing the capillary diameter from 2mm to 1mm (s. table 3.7).

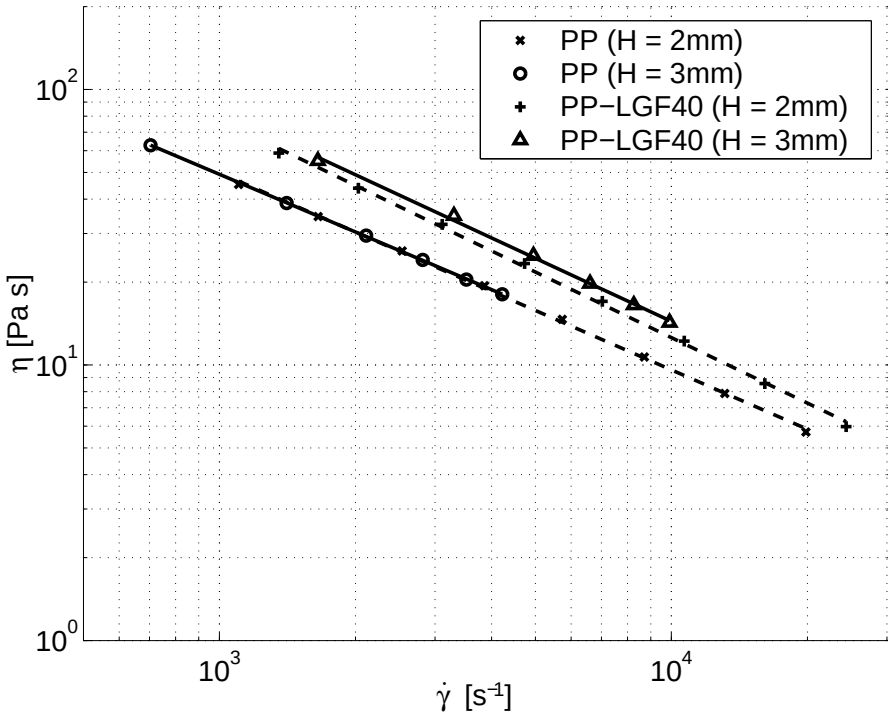

Figure 3.23: Shear Viscosity versus channel height, PP and PP-LGF40, 220^{o}C

In extensional flow, the dependence of flow properties on channel height becomes more pronounced. Higher values in extensional viscosity with an increase of roughly 14% are observed when the channel height is increased from 2 to 3mm (fig. 3.24).

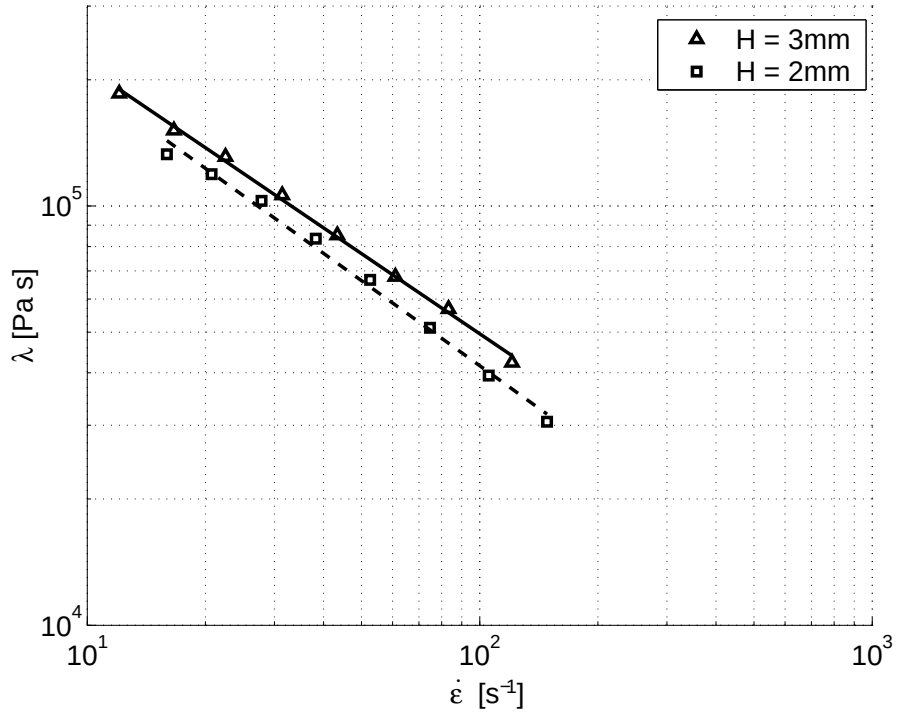

Figure 3.24: Extensional Viscosity vs. Channel height, PP-LGF40, 220^{o}C

In capillary rheometry, the effect of channel dimensions on extensional viscosity measurement has also been reported [30]. However, the extensional viscosity of PP-LGF50 was found to be more than two times higher using a capillary with a diameter of D = 1mm when compared to the results obtained with a capillary diameter of D = 2mm.

3.4.3.3 Contraction ratio

The contraction ratio of the converging die also influences the extensional viscosity, as depicted in fig. 3.25. Using a slit die with a higher contraction ratio yields higher values of extensional viscosity. The difference in extensional viscosity for different ratios of contraction was found to grow with fiber fraction and rate of extension as well as with declining temperature. A maximum difference of approximately 20% was observed.

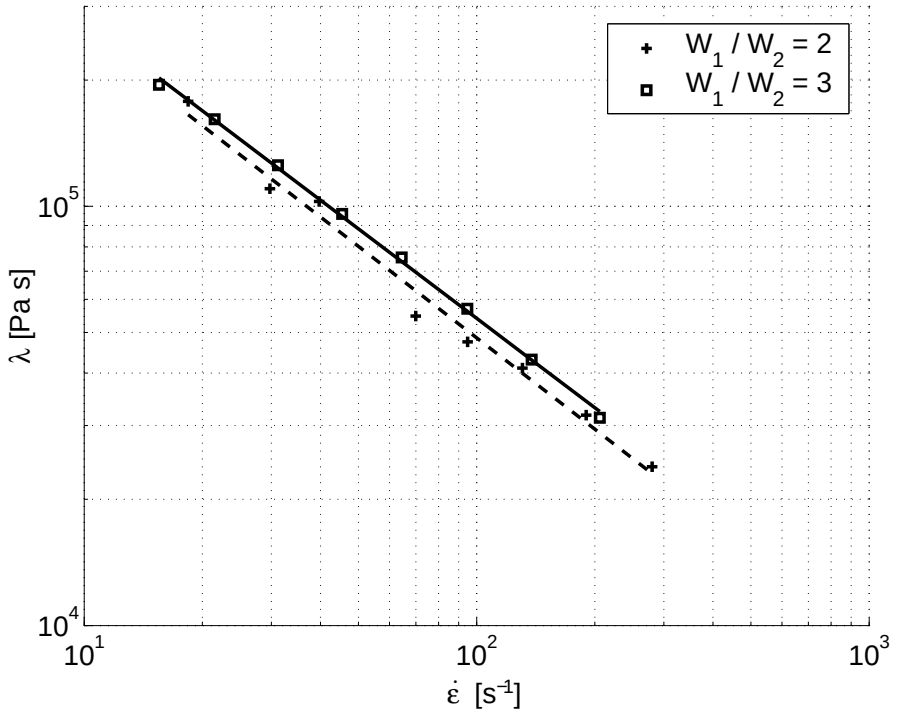

Figure 3.25: Extensional viscosity versus Contraction ratio, PP-LGF50, 220^{o}C

Using a die with a smaller contraction ratio, higher rates of extension were achieved but less reliable results were obtained. However, the dependence of extensional viscosity on rate of deformation is not significantly affected by the contraction ratio.

3.5 Modelling of Flow properties

3.5.1 Orthotropic constitutive law

The difference in resistance to shear and extensional deformation is described using the trouton ratio of extensional viscosity and shear viscosity. While for neat thermoplastics a trouton ratio between 8 and 9 is typical, the difference becomes substantial for long fiber reinforced thermoplastics with a trouton ratio of 60 and higher.
In contrary to solid mechanics, the anisotropic behavior of composite materials during flow has not received very much attention. To the author's knowledge, extensional viscosity has yet not been subject to profound numerical simulations of polymer processing since it implies the modification of the Navier-Stokes equations. Simplified approaches [180] were derived in order to account for extensional viscosity by modifying shear viscosity.
Gibson [60] proposed an orthotropic constitutive law

$$\begin{Bmatrix} \dot{\epsilon}_{11} \\ \dot{\epsilon}_{22} \\ \dot{\epsilon}_{33} \\ \dot{\gamma}_{23} \\ \dot{\gamma}_{31} \\ \dot{\gamma}_{12} \end{Bmatrix} = \begin{bmatrix} \frac{1}{\lambda} & \left(\frac{1}{2\lambda} - \frac{1}{\lambda_\perp}\right) & -\frac{1}{2\lambda} & 0 & 0 & 0 \\ \left(\frac{1}{2\lambda} - \frac{1}{\lambda_\perp}\right) & \frac{1}{\lambda_\perp} & -\frac{1}{2\lambda} & 0 & 0 & 0 \\ -\frac{1}{2\lambda} & -\frac{1}{2\lambda} & \frac{1}{\lambda} & 0 & 0 & 0 \\ 0 & 0 & 0 & 0 & 0 & \left(\frac{4}{\lambda_\perp} - \frac{1}{\lambda}\right) \\ 0 & 0 & 0 & \frac{1}{\eta} & 0 & 0 \\ 0 & 0 & 0 & 0 & \frac{1}{\eta} & 0 \end{bmatrix} \begin{Bmatrix} \sigma_{11} \\ \sigma_{22} \\ \sigma_{33} \\ \sigma_{23} \\ \sigma_{31} \\ \sigma_{12} \end{Bmatrix} \tag{3.4}$$

where η and λ denote shear and extensional viscosity, respectively. The difference between in-plane and out-of-plane extensional viscosity is captured by $\lambda_\perp$. Since it is difficult to obtain $\lambda_\perp$ experimentally, the use of the value for extensional viscosity of the neat thermoplastics is proposed.

3.5.2 Power-law coefficients

The use of a power-law type relationship for both shear and extensional viscosity has lead to good agreement with experimental results. If the temperature-invariant form

$$\eta = k \cdot e^{\beta_\eta (T - T_0)} \cdot \dot{\gamma}^{n-1} \tag{3.5}$$

$$\lambda = l \cdot e^{\beta_\lambda (T - T_0)} \cdot \dot{\epsilon}^{t-1} \tag{3.6}$$

is introduced, the coefficients listed in table 3.5 are derived with T_0 = 175^{o}C:

ψ	k_0	β_η	n	l_0	β_λ	t
[1]	[10^4 Pa s^n]	[1/K]	[1]	[10^6 Pa s^t]	[1/K]	[1]
0	1.0135	-0.0045	0.2831			
0.3	1.3327	-0.0049	0.2829	1.0853	-0.0021	0.3027
0.4	2.1430	-0.0060	0.2547	1.2502	-0.0037	0.3188
0.5	2.7873	-0.0057	0.2447	1.6943	-0.0048	0.3019
0.3 [1]	1.9387	-0.0045	0.2531	0.9672	(0.00042)	0.2871
0.5 [2]	2.0202	-0.0057	0.2607	1.2520	-0.0036	0.3246

Table 3.5: Power-law coefficients for shear and extensional viscosity

The error by introducing a power-law type relationship for the dependency of both shear and extensional viscosity on rate of deformation and temperature is listed in table 3.6. The standard deviation is higher for extensional viscosity since the coefficients for shear viscosity are included in the calculation.

ψ [1]	σ_η [%]	σ_λ [%]
0	4.59	-
0.3	2.94	6.82
0.4	4.04	7.58
0.5	2.88	7.36
0.3[1]	2.41	2.38
0.5[2]	2.51	2.75

Table 3.6: Standard deviation of power-law relationship

[1] l = 12mm
[2] standard sizing

3.6 Discussion of results

3.6.1 Comparison with previous results

The results obtained for shear and extensional viscosity were compared to values found in literature (s. table 3.7). For PP, the amount of data available is not as plenty as for other thermoplastics, e.g. PA6.6.

	ψ [%]	l_0 [mm]	T [^{o}C]	k_0 [Pa s^n]	n [1]	l_0 [Pa s^t]	t [1]	source
PP	10	10	180	1685	0.483			[42]
	20	10		2303	0.447			
	30	10		3092	0.414			
	40	10		4365	0.404			
	50	10		9307	0.303			
PP	0		200	785	0.58	6.63 $\cdot 10^4$	0.61	[30][1]
	50	5		1284	0.58	6.5 $\cdot 10^5$	0.56	
	50	6		1558	0.54	9.62 $\cdot 10^5$	0.58	
	50	6		2403	0.47	1.07 $\cdot 10^5$	0.62	
	50	10 [3]		1472	0.56	4.98 $\cdot 10^5$	0.56	
	50	10 [4]		1194	0.58	1.15 $\cdot 10^6$	0.57	
	50	10		1311	0.57	1.7 $\cdot 10^6$	0.58	
PP	50	10 [3]	200	1570	0.57	3.06 $\cdot 10^5$	0.554	[30][2]
	50	10		1208	0.56	7.48 $\cdot 10^5$	0.57	
PP	20	6	200	3200	0.50			[27]
PP	30	15	210	3780	0.346	1.0 $\cdot 10^5$	0.346	[181]
PP	0		230	9357	0.30			[31]
	5	4.5		11083	0.27			
	10	4.5		11925	0.26			
	20	4.5		13787	0.25			
	30	4.5		16959	0.21			
PP	50	10	235	954	0.528	1.03 $\cdot 10^5$	0.564	[182]

Table 3.7: Power-law coefficients for shear and extensional viscosity, from literature

[1] Capillary, diameter D = 1mm
[2] Capillary, diameter D = 2mm
[3] passed trough cutter, $l \leq$ 10mm
[4] passed trough injection molding machine

It should also be noted that the data was obtained at one specific melt temperature using different instruments, such as capillary or squeeze flow rheometers. Comparing the results is very difficult since fiber fraction as well as initial fiber length are deviating.
Power-law coefficients for the shear viscosity of neat PP with different molecular weight are listed in table 3.8. The shear viscosity, measured using a capillary rheometer, can differ by a factor of 4 depending on molecular weight. A deviation in shear-thinning behavior is also observed. However, the flow exponent is within a range between n = 0.275 and n = 0.386, confirming the values derived in this work

M_W	k_0	n
	[Pa s^n]	[1]
1171	23511[1]	0.262
534	23070	0.275
407	11048	0.333
316	6802	0.372
222	11074	0.294
179	5146	0.386

Table 3.8: Power-law coefficients for shear viscosity for PP with different molecular weights, T = 200^{o}C

Throughout all different sources, the trend of declining power-law index for shear viscosity with increasing fiber fraction is observed and confirmed by the results of this study.
For extensional viscosity, the results obtained were compared to the data derived by Binding [30] and McClelland [182] for PP-LGF50 with an initial fiber length of l = 10mm. Both studies were carried out using a capillary rheometer supplied with melt from a piston-cylinder system.

[1] T = 255^{o}C

In fig. 3.26, the results for PP-LGF50 obtained in this work using a slit rheometer are extrapolated to a melt temperature of 200^{o}C and then plotted versus the results of Binding obtained for different capillary diameter.

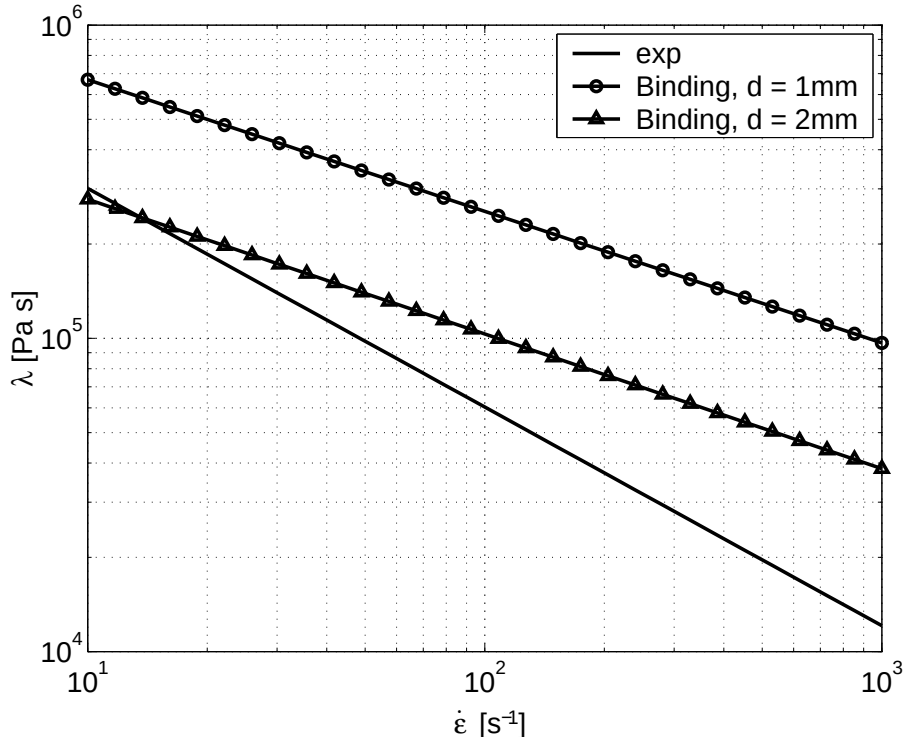

Figure 3.26: Extensional viscosity of PP-LGF50, T = 200^{o}C

The results derived from capillary rheometry are higher than the values obtained using a slit rheometer. Based on a higher bandwidth of rate of extensions (up to 10^4 s^{-1}), the thinning behavior was found to be less pronounced in capillary rheometers. However, an increase in capillary diameter from D = 1mm to D = 2mm lead to a reduction in extensional viscosity in the order of 57%, whereas shear viscosity was not significantly altered (minus 8%).

The results of McClelland were obtained using the same rheometer as used by Binding, but with a capillary diameter of D = 4mm. For this diameter, the results of McClelland yielded values lower than those obtained using slit rheometry (s. fig. 3.27).

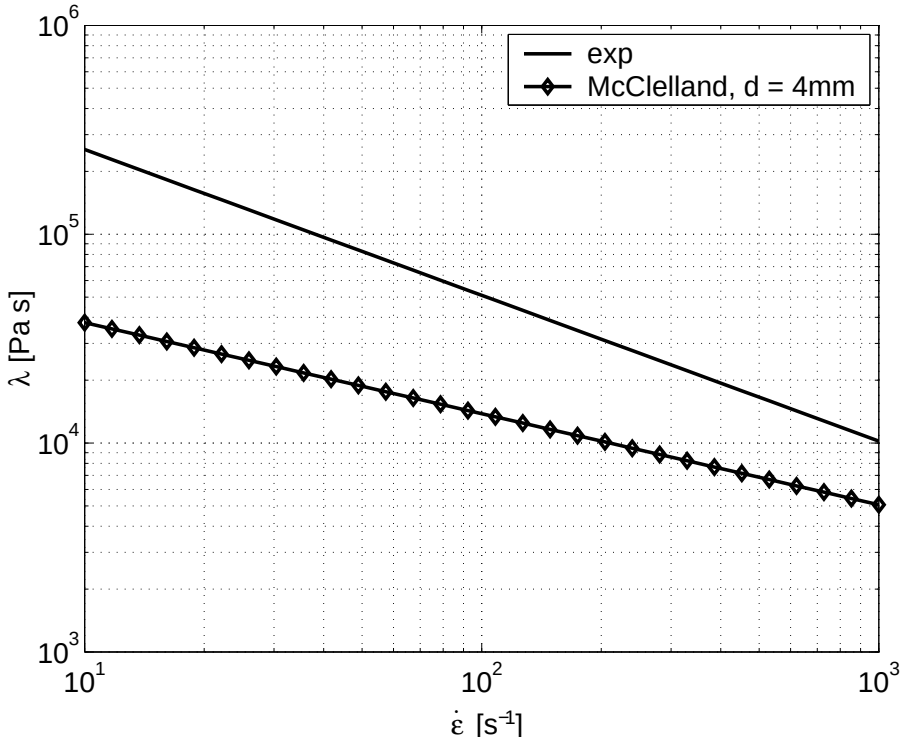

Figure 3.27: Extensional viscosity of PP-LGF50, T = 235^{o}C

Comparing the experimental results with the results of Binding and McClelland, it was found that the results obtained using the slit rheometer yielded the values for the capillary die with a small diameter (D = 2mm) at low rates of extension, at higher rates the results obtained for a diameter of D = 4mm.
While the absolute values for extensional viscosity are in the same range, a substantial deviation in thinning behavior is observed. The decline of extensional viscosity is strongly related to the shear-thinning behavior of the melt. The absolute values for extensional viscosity of neat PP was found to increase with molecular weight by a factor of 7 [52].

3.6.2 Error in pressure measurement

The reliability of pressure data is affected by the accuracy of the sensor, the pressure fluctuation during processing and the error in interpolation of the pressure profile along the die. Since each pressure sensor is calibrated with the amplifier and the signal is digitally compensated, the accuracy of the pressure sensor is very high. In order to minimize this error, the sensor were located along the die with respect to the operating range of the sensor and the expected pressure value at that location. The standard deviation in calculation of shear viscosity due to pressure fluctuation and interpolation is depicted in fig. 3.28.

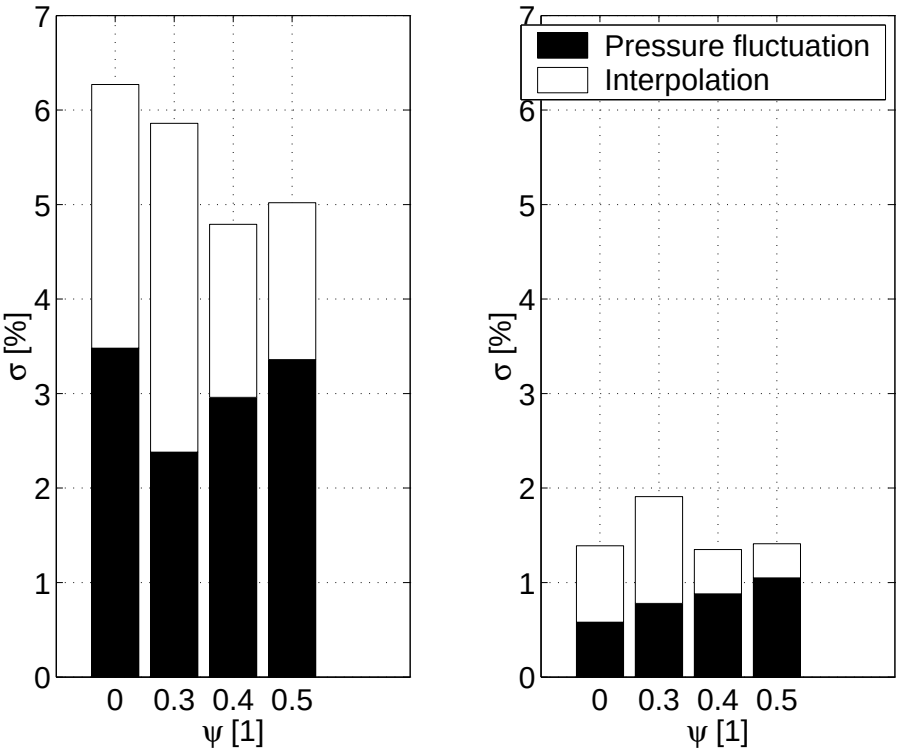

Figure 3.28: Maximum (left) and mean standard deviation (right) in shear viscosity calculation

Adding the error in pressure measurement and the error in deriving the constitutive law proposed for long glass fiber reinforced polypropylene, a maximum standard deviation of approximately 10% and 14% for shear and extensional viscosity, respectively, is derived.

3.6.3 Error in temperature measurement

Suspensions with high viscosity may generate substantial heat near the cavity walls at high shear rates. This heat will lower the viscosity in the vicinity of the wall and therefore make the melt appear more shear thinning.
Since temperature has a substantial effect on viscosity, it is essential to know at which temperature the measurement took place. It is also mandatory to validate the temperature measurement of the different sensor types.
In order to analyze the temperature profile along the die, the temperature signals were compared by replacing the piezo-resistive sensor close to the entrance (x = 0mm) and to the exit of the die (x = 105mm) by the infrared sensor. With these two setups, three exemplary flow rates were applied and the difference in temperature recorded.

			ΔT [^{o}C]					
ψ	T	$\dot{\gamma}$	piezoresistive sensor			infrared sensor		
[1]	[^{o}C]	[s^{-1}]	entrance	exit	total	entrance	exit	total
0	220	600	2.60	3.06	-0.45	4.60	6.96	2.36
		4740	2.94	5.32	-2.39	7.14	13.12	5.98
		10800	3.26	5.59	-2.32	8.44	17.28	8.84
0	250	600	1.68	1.07	0.61	-2.03	2.11	4.15
		4740	2.29	3.60	-1.31	1.00	7.32	6.31
		10800	2.35	4.05	-1.70	2.41	11.01	8.60
0.5	220	600	4.97	6.26	-1.29	12.34	13.27	0.92
		4740	7.58	9.70	-2.12	17.44	23.26	5.52
		10800	7.05	10.08	-3.03	19.81	27.50	7.69
0.5	250	600	3.57	4.23	-0.65	6.16	10.94	4.78
		4740	5.17	7.62	-2.45	11.56	18.19	6.63
		10800	6.13	8.38	-2.25	12.91	23.94	11.04

Table 3.9: Temperature rise as measured for PP and PP-LGF50

It is observed, that the melt entering the die has already been subject to an increase in temperature which is in the order of magnitude of the actual increase along the die. Comparing the temperature signal recorded using the piezo-resistive and the infrared sensor, respectively, a significant difference is found.
Using the temperature output of the piezo-resistive sensor, the level of temperature is substantially lower compared to the recording of the infrared sensor. The most significant feature is that a temperature drop along the die is recorded. The sensor does not capture the melt temperature, but the temperature within the ambience of the sensor.
In polymer processing, substantial increase in temperature during flow has been reported. Crowson [36] observed an increase in temperature of 73^{o}C during extrusion of neat PP at a shear rate of 3·10^5 s^{-1}, corresponding to a pressure drop of 1400 bar.
In order to determine the temperature rise analytically, Crowson used a simplified thermal analysis based on the assumption of adiabatic and incompressible flow. The change in temperature consists of two fractions. On one hand, dissipation leads to a significant rise with increasing flow length. On the other hand, temperature declines due to the pressure drop along the die. The change in temperature can then be calculated as a function of pressure drop using

$$\Delta T = \frac{\Delta p}{\rho c_p} \cdot (1 - \alpha T) \tag{3.7}$$

The first term accounts for the temperature rise due to dissipation which is caused by shear deformation. The second term describes the temperature drop resulting from the pressure drop along the die. Since the pressure decreases, the melt expands and therefore temperature decreases.
The amount of dissipation in shear flow can also be calculated from the energy balance equation. For one-dimensional, quasi-isothermal flow one derives

$$\rho c_p \cdot \frac{\partial T}{\partial x} = \eta \dot{\gamma}^2 \tag{3.8}$$

Using the thermal properties for PP and PP-LGF50 (s. appendix C), the temperature rise along a distance Δx due to dissipation can be calculated as a function of viscosity using

$$\frac{\Delta T}{\Delta x} = \frac{1}{\rho c_p v_x} \cdot \eta \dot{\gamma}^2 \tag{3.9}$$

Fig. 3.29 depicts the temperature rise for neat PP measured using the piezo-resistive sensor ('PR') and the infrared sensor ('IR') versus the predictions based on the energy balance and the assumption of incompressibility, respectively.

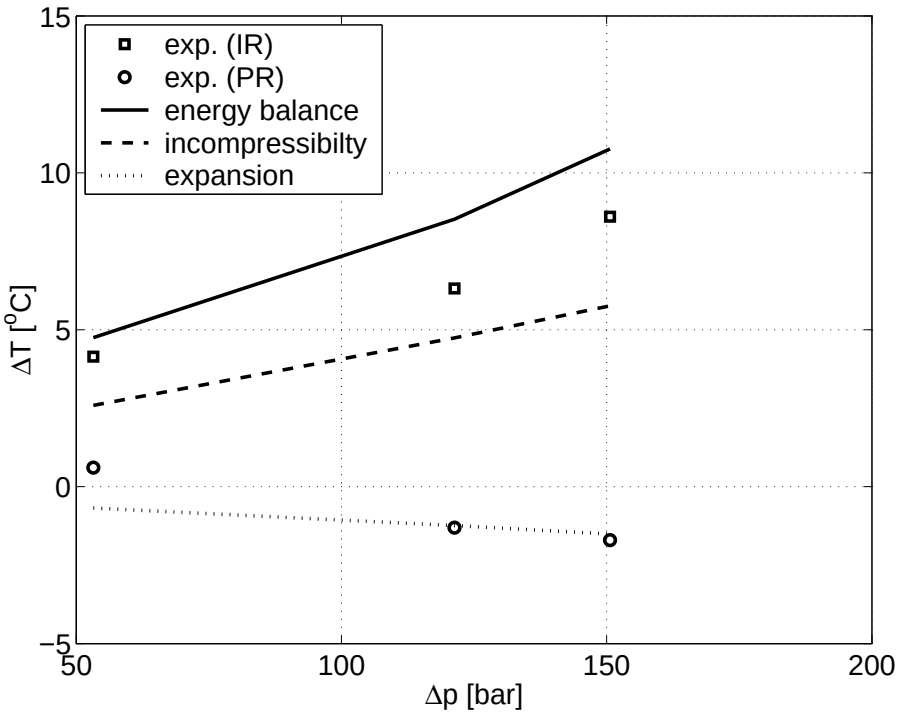

Figure 3.29: Temperature Profile, PP, 250 ^{o}C

The approach of incompressibility, due to the linear dependence of temperature rise on pressure drop, does not capture the non-linear temperature rise accurately. Adding the temperature drop caused by the expansion of the melt increases the difference.
However, the prediction based on the energy balance equation shows good agreement with data obtained using the infrared sensor, especially considering the temperature drop due to expansion which has to be added.

For PP-LGF50, the temperature rise predicted using the energy balance equation exceeds the experimentally recorded data (fig. 3.30). Again, the data recorded the piezo-resistive sensor yields the temperature drop predicted.

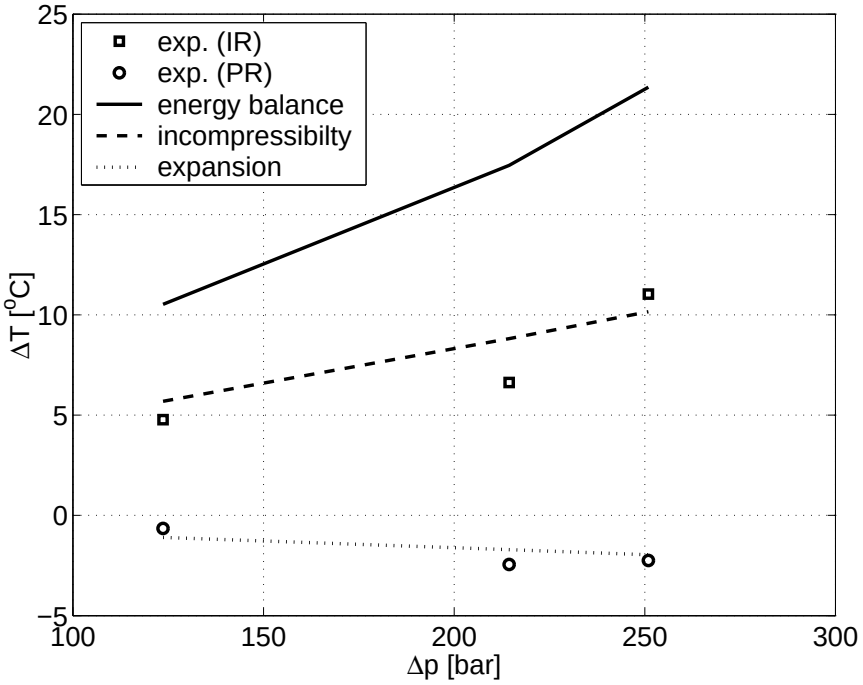

Figure 3.30: Temperature Profile, PP-LGF50, 250 ^{o}C

From the results above, it is deducted that the piezo-resistive sensors are not adequate for reliable measurement of temperature. The results obtained using the infrared sensor yielded good agreement with predictions for neat PP.
For fiber filled thermoplastics, the difference between prediction and experimental data became evident. The infrared sensor was statically calibrated for the fiber filled material, the flow of the fiber suspension and re-orientation of the fibers may induce errors due to refraction. It is also noteworthy, that the infrared sensor detects radiation emitted by a melt volume determined by the penetration depth of radiation, as discussed in section 3.1.2.2 and appendix A.

The importance of dissipation can be estimated using the Nahme-Griffith number which equates heat generated by viscous dissipation to heat conduction

$$Na = \frac{-\beta h^2 \tau \dot{\gamma}}{k} \tag{3.10}$$

For neat PP and PP-LGF50, Na is listed in table 3.10 at the lowest and highest melt temperature applied during processing.

ψ [1]	T [^{o}C]	β [1/^{o}C]	τ [MPa]	$\dot{\gamma}$ [s^{-1}]	k [W/mK]	Na [1]
0	220	-0.0045	0.113	21240	0.196	221
0	270	-0.0045	0.091	16790	0.168	164
0.5	220	-0.0057	0.186	24710	0.403	260
0.5	270	-0.0057	0.156	20400	0.382	190

Table 3.10: Nahme-Griffith number for PP and PP-LGF50

The typical range of Na for neat polymers is $0 < Na < 200$, which is exceeded here at low temperature levels and high fiber fractions. For $Na < 0.5$ [183] or $Na < 1$ [26], the viscosity is considered to be unaffected by dissipation. Hence it must be concluded that the reliability of results obtained for shear and extensional viscosity is affected by dissipation.
In order to improve the accuracy of rheological measurements, a numerical solution of the momentum and energy equations must be performed. The dependence of viscosity on temperature, shear rate and pressure must be accounted for. Heat conduction and convection must be considered as well as heat transfer from the melt to cavity walls. A detailed analysis is beyond the scope of this work. An analysis of thermal effects in extrusion dies is given by Pittman and Sander [184].

4 Microstructure

4.1 Techniques

The microstructure of thermoplastics filled with fibers is induced by flow and affected by fiber-fiber interaction and is therefore non-homogeneous. For long fibers, interaction with the cavity walls also affects the orientation. In order to have a complete description of the microstructure, information about the spatial distribution of fiber alignment, dispersion and length is required.
However, there is no technique allowing for a one-step, non-destructive spatial evaluation of microstructure. Three-dimensional information on morphology is either based on a moving detector applying the principle of tomography which was proposed by Radon [185] and originally applied by Cormack [186] and Hounsfield [187]. The second approach is a semi-destructive method where the part is sectioned, images are taken and then re-assembled in order to obtain the three-dimensional microstructure.
In order to detect the heterogeneous microstructure of fiber filled thermoplastics, several techniques have been employed. These techniques are either destructive or non-destructive and may account for two-dimensional or three-dimensional fiber orientation. The suitability of any technique for the evaluation of three-dimensional microstructure is determined by the size of volume to be detected and resolution of detection.
Optical techniques have been employed since the mid 1970s. Using the optical reflection technique, samples are sectioned and polished and then evaluated using light microscopy. For glass fiber filled polymers, the lack of contrast due to matching refractive index, requires sputtering of fibers. The two-dimensional microstructure of fiber filled polymers has been examined in a number of studies [188–192].
Using tracer fibers, three-dimensional evaluation of fiber orientation in transparent thermoplastics based on the optical reflection technique has been performed by McGrath and Wille [193, 194]. The resolution of optical reflection techniques is not smaller than 1μm [195] while the technique is limited to samples with a cross-section.
Confocal laser scanning microscopy (CLSM) has been applied to polymer composites by Clarke and Davidson [196]. The three-dimensional structure of polymer composites is evaluated using laser light by placing the focal plane at different depths. Both axial and lateral resolution of CLSM is in the order of 0.3μm. At high fiber volume fraction (ψ=0.5), the penetration depth and hence the sample thickness is approximately 40μm, while the sample area is 1mm by 1mm.

In optical coherence tomography (OCT), depending on the coherence length of the light source an axial resolution of 5μm and a transverse resolution 10 to 30 μm, determined by the focal spot size can be achieved using a light source of wavelength λ = 20 to 200 nm [197].

In the case of non-optical techniques, ultrasound imaging offers the potential of large-scale, truly non-destructive examination of composite structures. It has been applied to glass-fiber reinforced PP [198], where a spatial resolution greater than 100 μm was achieved.

Nuclear magnetic resonance (NMR) tomography, also termed as magnetic resonance imaging (MRI), allows for three-dimensional reconstruction of morphology and has become a standard procedure in medical applications. The resolution varies from 10 to 100 μm, depending on the frequency of scanning. NMR is based on the method of measuring relaxation times, i.e. the response time of an atom when its spin is aligned by an external magnetic field and then released. The harder the materials are, it becomes more difficult to evaluate its microstructure since the response time decreases and is therefore less detectable. Specimens of injection-molded PP-LGF50 have been examined at the Fraunhofer Institute for Chemical Technology (ICT). Although the specimen is heated up to a temperature of 80^{o}C in order to increase relaxation time, no useable results could be obtained. It has been found that the contrast strongly depends on the additives to the PP. With increasing fraction of softeners the contrast between fibers and matrix becomes more pronounced and valuable results can be obtained.

X-ray imaging with a resolution between 5 and 15 μm is a widely used technique for the two-dimensional evaluation of microstructure in polymer composites, e.g. [199,200]. While conventional x-ray imaging relies on the detection of contrast between phases due to absorption, information on three-dimensional structure is provided measuring both contrast and phase of the radiation transmitted [201].

4.2 Two-dimensional microstructure

Photographs were taken of the injection molded samples using X-ray imaging (FEINFOCUS FXS-100:10, 100kV, 0,4mA) and then digitized by scanning (MICROTEK) with 600dpi and 2000dpi, respectively. The fiber orientation was evaluated using the image processing software FIBORAS, developed at IVW [199, 202]. Each specimen was divided into 5 regions in flow direction and 5 biased sections in width direction yielding a total number of 25 sections. The data was then visualized by contour plots using MATLAB.

4.2.1 Fiber orientation

4.2.1.1 Fiber orientation versus fiber fraction

The fiber orientation, averaged in thickness direction and represented by the a_{11} component of the orientation tensor, is depicted in fig. 4.1. At the wall, high alignment in the flow direction with $a_{11} \geq 0.9$ is observed. In the center section of the image, the orientation is dominated by random orientation. With increasing fiber fraction, the orientation is less random since the mobility of the fibers declines and the probability of fiber collisions reduces.

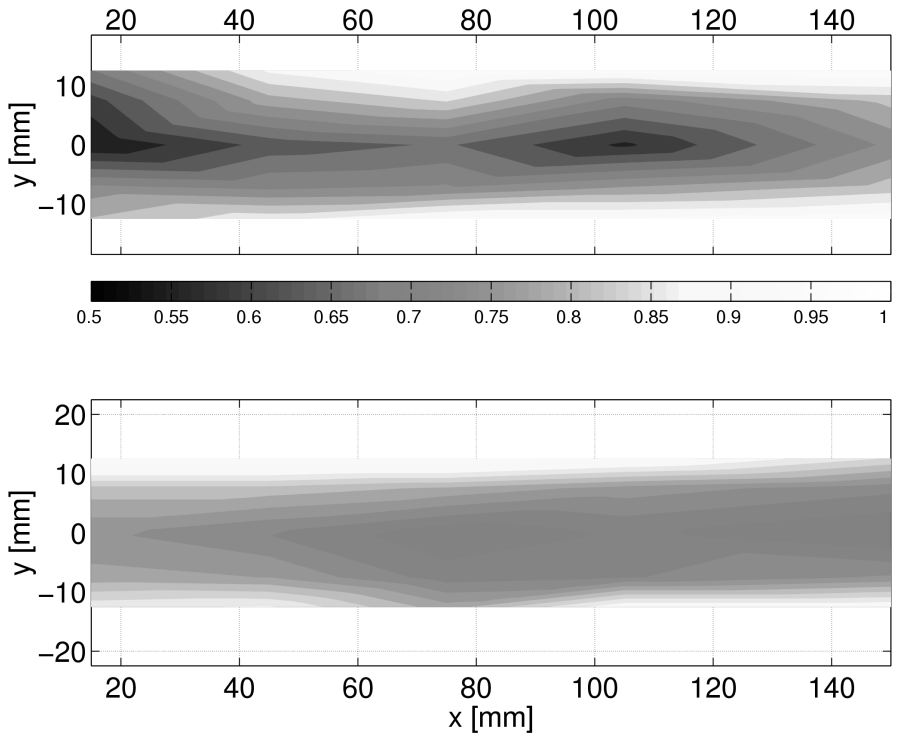

Figure 4.1: Fiber orientation tensor component a_{11} for PP-LGF at fiber fractions of 30% (top) and 50% (bottom), T = 250^{o}C

4.2.1.2 Fiber orientation versus fiber sizing

The interface between fibers and the surrounding suspension affects fiber orientation (s. fig. 4.2). Since the transferrable shear stress at the interface is reduced and the possibility of slip is increased, a non-optimized fiber sizing leads to an orientation state shifted towards random.

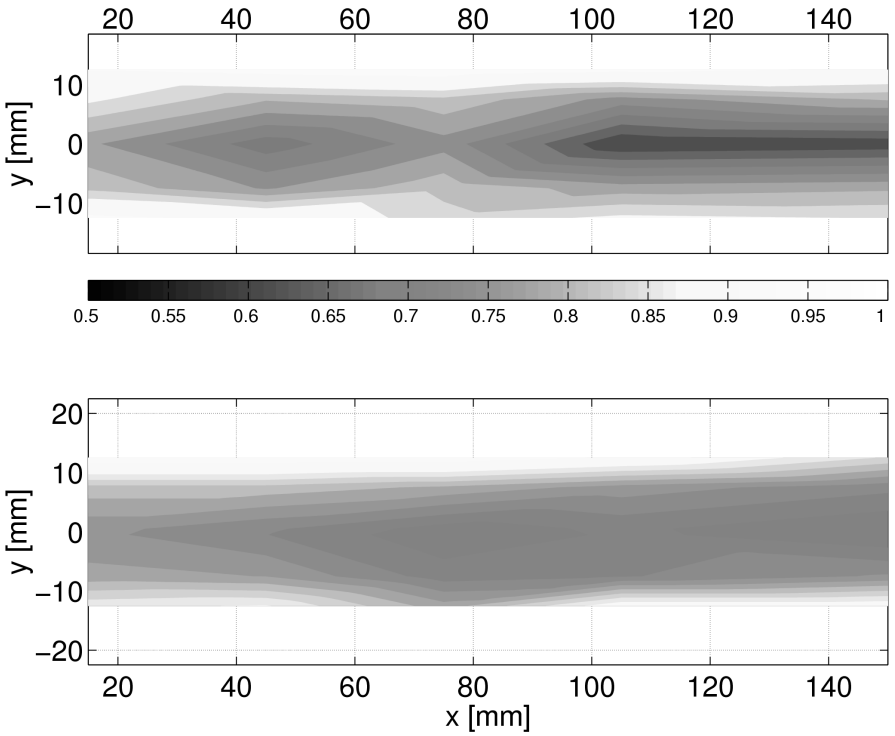

Figure 4.2: Fiber orientation tensor component a_{11} for PP-LGF50 with standard sizing (top) and optimized sizing (bottom), T = 250^{o}C

4.2.1.3 Fiber orientation versus flow rate

The effect of flow rate on fiber orientation is depicted in fig. 4.3. Increasing the apparent shear rate by a factor of 2 substantially affects the alignment of the fibers in the main direction of flow in the wide section of the converging die. In the narrow section, after the melt has passed the convergence, a further increase in fiber alignment is evident while the difference in fiber orientation tensor component a_{11} declines. The higher degree of alignment is due to a doubled shear rate in the narrow section and to the aligning effect of converging flow. Contraction flow appears to have a more pronounced effect on fiber alignment than shear rate and hence the difference in fiber orientation for different shear rates decreases.

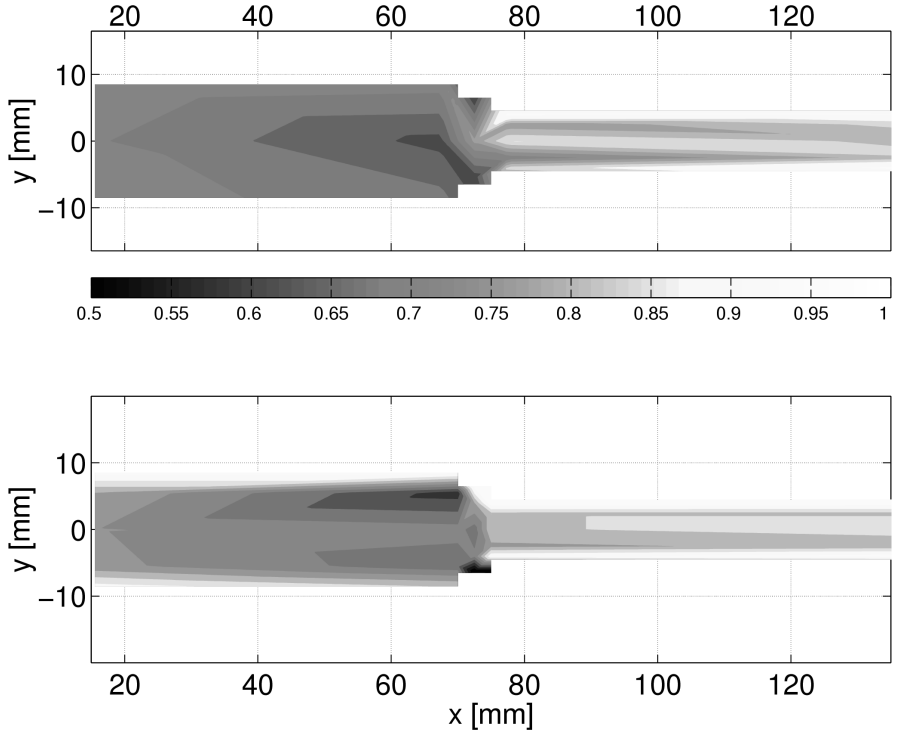

Figure 4.3: Fiber orientation tensor component a_{11} for PP-LGF50 at Q = 90 cm^3/s (top) and Q = 180 cm^3/s (bottom), T = 250^{o}C

It also appears that convergent flow has an effect on fiber orientation upstream

from the contraction. At the lower flow rate, fiber orientation is enhanced in a section with a length of roughly 5mm upstream of the actual contraction. At higher shear rates, the formation of recirculating zones in the contraction appear to become evident.

4.2.1.4 Fiber orientation versus melt temperature

Melt temperature and therefore viscosity strongly affects fiber orientation, as depicted in fig. 4.4. Increasing the melt temperature from T = 220^{o}C to T = 250^{o}C randomizes fiber orientation in the core zone. This effect is caused by a reduction in shear stress imposed on the fiber due to a viscosity lower by the order of 20%.

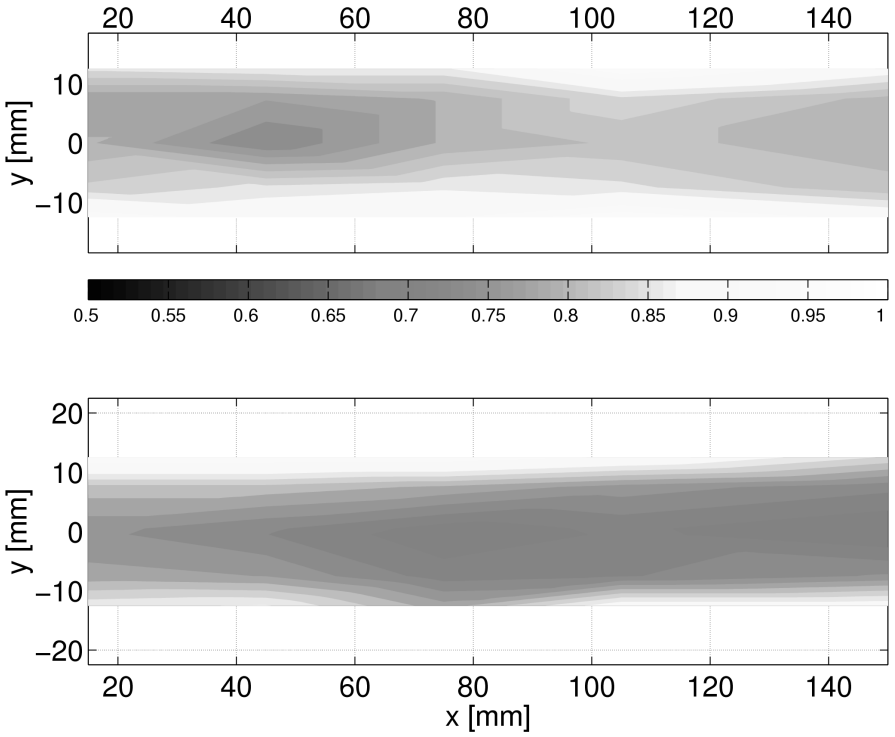

Figure 4.4: Fiber orientation tensor component a_{11} for PP-LGF50 at T = 220^{o}C (top) and T = 250^{o}C (bottom)

4.2.1.5 Fiber orientation versus channel height

In contrary to previous publications, it was observed that with decreasing cavity height the average fiber orientation becomes more random suggesting that the thickness of the core increases. For a cavity height of H = 3mm, fiber orientation in the main direction of flow is increasing and the center region of the melt with a lower degree of alignment narrows with decreasing distance from the convergence.
However, for the cavity with H = 2mm, a higher degree of random orientation in the center region is evident upstream from the convergence. It also appears that the state of randomness increases with decreasing distance from the convergence due to jamming of the fibers at the convergence affecting orientation on both sides of the contraction.

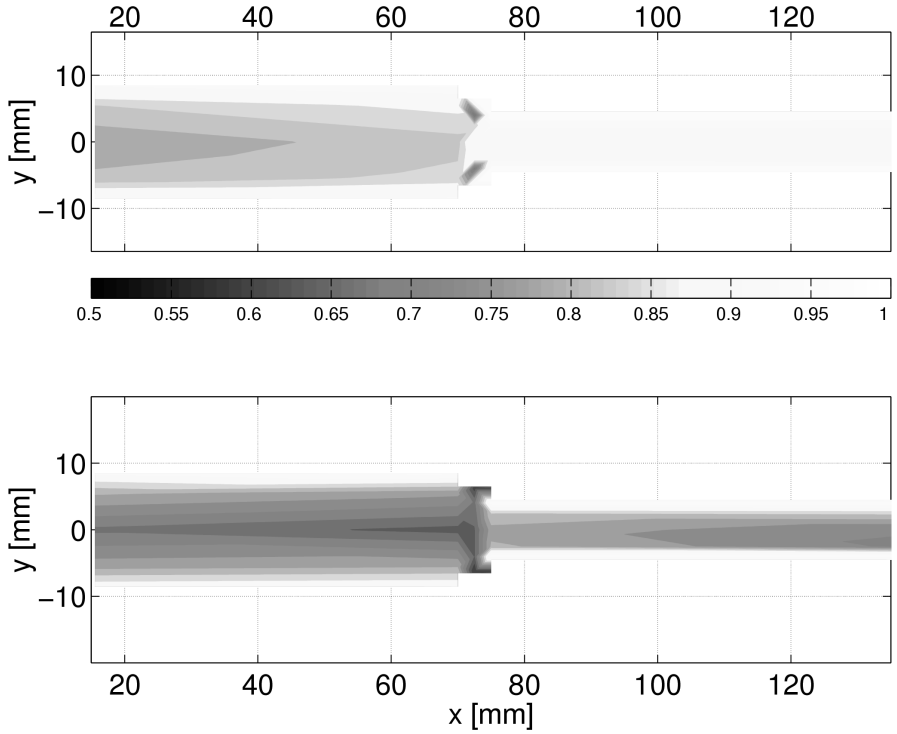

Figure 4.5: Fiber orientation tensor component a_{11} for PP-LGF50 using a slit height H = 3mm (top) and H = 2mm (bottom), T =220^{o}C

4.2.2 Fiber length

While for short fiber reinforced thermoplastics, good agreement is achieved between values predicted and measured for extensional viscosity, the models over-estimate extensional viscosity of long fiber reinforced thermoplastics, as previously reported in [34].
The theoretical approaches were used to estimate the effective aspect ratio of the fibers. From the measurements of extensional viscosity, the values for the aspect ratio listed in table 4.1 are calculated for different melt temperature using the model of Goddard and Batchelor (eqn. 2.20) as well as the theory by Coffin and Pipes (eqn. 2.21). The theoretical aspect ratio is derived from initial fiber length (l = 10mm) and diameter of a single glass fiber (d = 17μm).

	a_r [1]					
T [^{o}C]	220			270		
ψ [1]	0.3	0.4	0.5	0.3	0.4	0.5
theoretical	588.24	588.24	588.24	588.24	588.24	588.24
Goddard / Batchelor	139.11	74.21	60.25	154.99	80.98	62.36
Coffin / Pipes	122.25	72.52	63.44	136.20	79.15	65.67

Table 4.1: Effective aspect ratio

The aspect ratio decays with increasing volume fraction but increases with melt temperature and the values predicted using both theories slightly differ. The theoretical aspect ratio calculated from initial fiber length is more than four times higher than the values derived. In a previous study on PP-LGF40, an effective aspect ratio of 60 was found [203], underlining the suitability of both theories.

4.2.3 Extrudate analysis

Die swell is a measure for elastic recovery of polymer melts but it also depends on temperature distribution. For long fiber reinforced thermoplastics, extrudate analysis is difficult to perform since the strand is very inhomogeneous and the borders are irregular.
Using two different samples exemplarily for each configuration of parameters, height and width of the strand were measured at three and five locations, respectively, and then averaged (s. table 4.2). The width and height of the cavity was B = 25mm and H = 2mm, respectively.

Generally, die swell in width and height direction declines with increasing shear rate due to the higher degree of alignment in the main direction of flow. For a lower melt temperature, the increase in width and height of the strand is reduced since the viscosity of the matrix is higher.

ψ [1]	T [^{o}C]	$\dot{\gamma}$ [s^{-1}]	b [mm]	b/B[1]	h [mm]	h/H [1]
0.5	220	600	37.22	1.49	7.23	3.62
		4740	35.87	1.43	6.01	3.00
		10800	33.81	1.35	9.46	4.73
0.5	250	600	38.21	1.53	8.71	4.36
		4740	36.61	1.46	8.92	4.46
		10800	36.62	1.46	7.67	3.84
0.5[1]	250	600	40.00	1.60	5.30	2.65
		4740	38.40	1.54	4.00	2.00
		10800	38.50	1.54	3.70	1.85
0.3	250	600	38.42	1.54	4.07	2.04
		4740	38.90	1.56	3.50	1.75
		10800	38.80	1.56	3.55	1.78
0.3[2]	250	600	36.50	1.46	4.30	2.15
		4740	34.50	1.38	4.30	2.15
		10800	36.10	1.44	3.40	1.70

Table 4.2: Die swell, PP-LGF50 and PP-LGF30

For a standard treatment of the glass fiber surface, an increase in die swell in width direction and decrease in height direction is observed. Hence, the out-of-plane orientation must be reduced but the in-plane orientation is shifted towards a random state. However, the total increase in volume is reduced when compared to PP-LGF50 with an optimized fiber sizing.

Die swell in width direction slightly increases at lower fiber fraction whereas the swell in height direction is substantially reduced suggesting the same effect as observed for fiber sizing. Increasing fiber length reduces die swell in width direction while the change in height direction remains unaltered. It is also notable that the effect of shear rate at lower fiber fraction is not as pronounced as observed at high fiber fraction.

[1] standard sizing
[2] l = 12mm

4.2.4 Effect of microstructure on viscosity

During the rheological characterization of long fiber reinforced PP it was generally found that extensional viscosity exceeds shear viscosity by up to two decades. Addressing the effect of process parameters on viscosity, thinning with rate of deformation, characterized by the flow exponent n and t, respectively, is observed in both shear and extensional flow. While t roughly remains constant for extensional viscosity, n decreases for shear viscosity with increasing fiber fraction. Therefore shear thinning increases with increasing fiber fraction. From the x-ray image (fig. 4.3) and extrudate analysis, a higher degree of alignment in flow direction is derived.
The explanation is found in the flow behavior of the suspension and the orientation of fibers during flow across the channel height. The velocity profile of neat and fiber filled PP in capillary flow was evaluated by Crowson [29]. At low shear rates, the velocity profile is almost parabolic. A large fraction of the melt will be subject to shear flow. Although shear flow induces a high degree of alignment, the fibers tend to rotate periodically by 180^o and the probability of fiber collisions rises yielding a high contribution of the fibers to the bulk viscosity.
However, at high shear rates, the velocity profile becomes blunter, with a trend towards plug flow with increasing fiber fraction. Hence, most of the shearing takes place in the shell layer of the melt. A high degree of alignment is therefore found in the vicinity of the wall while fiber orientation in the core zone is not altered. The contribution of fiber orientation to shear viscosity reduces.
For the second process parameter, an increase in melt temperature yields a fiber orientation state generally shifted towards randomness, as depicted in fig. 4.4. The shear viscosity of the matrix declines and the torque acting on the fibers is reduced. Although the degree of alignment in flow direction is reduced, the velocity profile becomes more parabolic and a growing portion of the melt is subject to shear flow and hence the chance of fiber collisions declines. The decline of viscosity with increasing melt temperature has a more pronounced effect in shear flow rather than in extensional flow. However, it was observed that the temperature effect increases with fiber fraction. The difference in viscosity for different fiber fraction reduces with temperature, more pronounced for shear viscosity rather than extensional viscosity.

For the effect of materials parameters on viscosity it was found, that the trouton ration, $Tr = \lambda/\eta$, declines from 81 to 60 when the fiber fraction is increased from 30% to 50%. Therefore fiber fraction has a more pronounced effect on shear viscosity rather than on extensional viscosity. The effect is more pronounced at low shear rates and declines with increasing shear rate. The explanation is given by the velocity profile.
Increasing fiber length induces a growth in shear viscosity whereas extensional viscosity is not significantly altered by increasing the initial fiber length from 10 to 12mm. From extrudate analysis, it is found that die swell in the width direction is reduced indicating a lower degree of transverse orientation. Applying the models for prediction of extensional viscosity to the viscosity experimentally derived yields an increase in remaining average fiber length with temperature and a decrease with fiber fraction.
Fiber sizing does affect microstructure and hence the rheological properties of the melt. In terms of fiber orientation it is observed that the degree of alignment is reduced for a poor fiber interface. From examination of die swell, an increase in width direction and a decrease in height direction is observed, indicating a more random orientation or more intensive fiber bending in width direction. The out-of-plane orientation and bending appears to be reduced. Although a more random orientation would yield higher values for viscosity, the shear stress transmitted via the fiber interface is expected to be lower. The probability of slip during flow is increasing.
Although the dispersion has not been subject of the experimental investigation, it is notable that there is a substantial effect on viscosity. With increasing degree of dispersion, both shear and extensional viscosity of PP-LGF were found to grow with a more pronounced effect than fiber length [29, 30].
From the experimental observations it is evident that shape and dimensions of the flow channel affect both microstructure and rheology. With increasing cavity height, a higher degree of alignment was found. While shear viscosity was not altered, a substantial increase in extensional viscosity is found.

4.3 Three-dimensional microstructure

In order to evaluate the three-dimensional microstructure including fiber orientation, length and dispersion, a technique similar to x-ray tomography was developed.
Instead of using a moving x-ray source and detector which implies substantial effort, the samples were sliced parallel and transverse to the flow direction according to fig. 4.6.

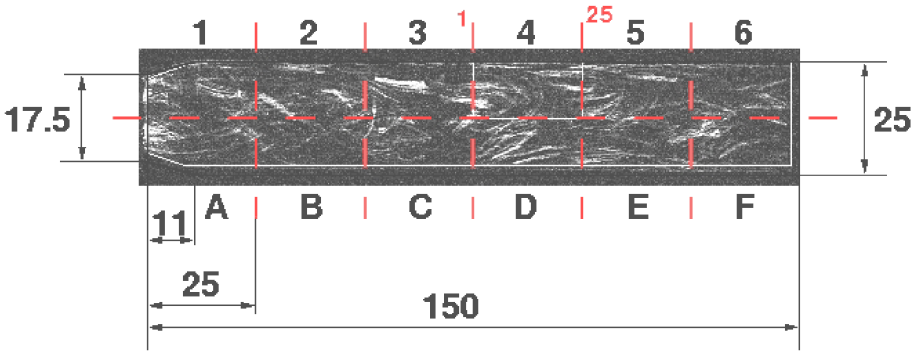

Figure 4.6: X-ray image of sample, PP-LGF50

The section with a length of 25mm and width of 12.5mm is then embedded in resin in order to ease further handling. The slices were produced using a microtome (Leica). With a minimum cut thickness of 0.3mm, sections with a thickness of 0.7mm were obtained.
A similar method was proposed in [204, 205]. Based on microscopic images of polished cross-sections, the three-dimensional fiber orientation of short and long fibers was evaluated. While cut images of a short fiber yield an ellipsis, evaluation of the orientation of long fibers became difficult due to curvature yielding irregular cut images. The method is also limited with respect to fiber fraction and sample size.
The x-ray image of section 4 (s. fig. 4.6) and the corresponding cross-sectional images are depicted in fig. 4.7, counterclockwise rotated by 90^o.

The images clearly show, that fiber bundles remain intact in the core zone. Bundles aligned with the flow direction as well as transverse orientation of fibers with parabolic shape due to bending is observed. Fiber dispersion is found at the mold walls only. The closer the bundles are located to the mold wall, the more flattened the cross-section of the bundles.

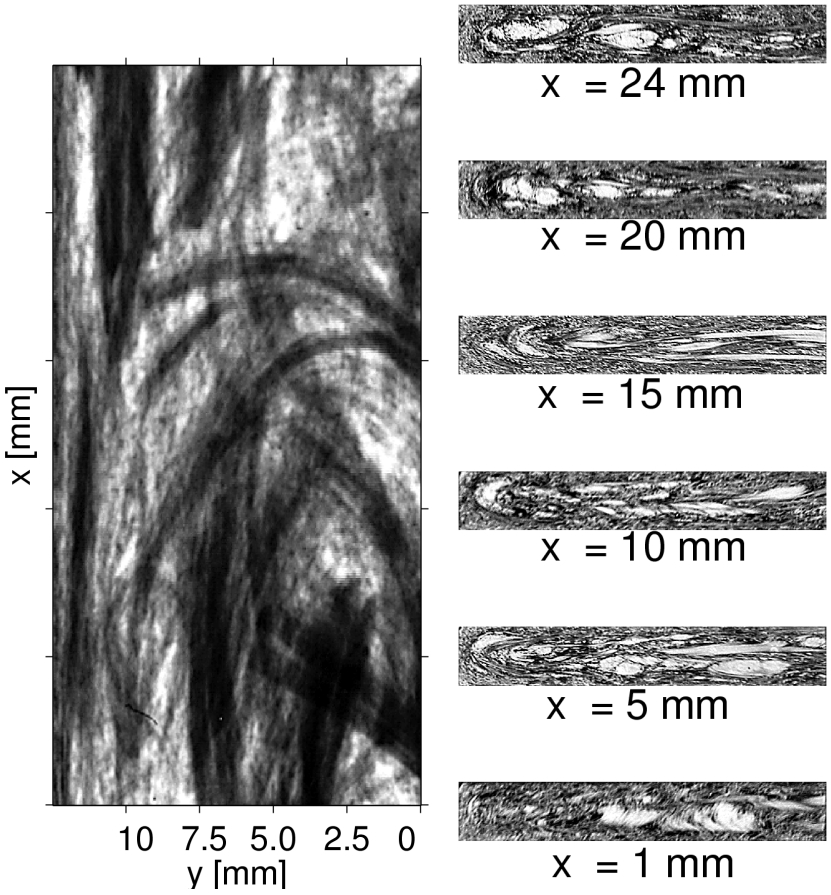

Figure 4.7: X-ray image of section evaluated transverse to the main direction of flow

Assembling the images of the cross-sections leads to the data structure based on gray-scale values as visualized in fig. 4.8. For the scans, a resolution of 600dpi is sufficient reducing the computational effort.

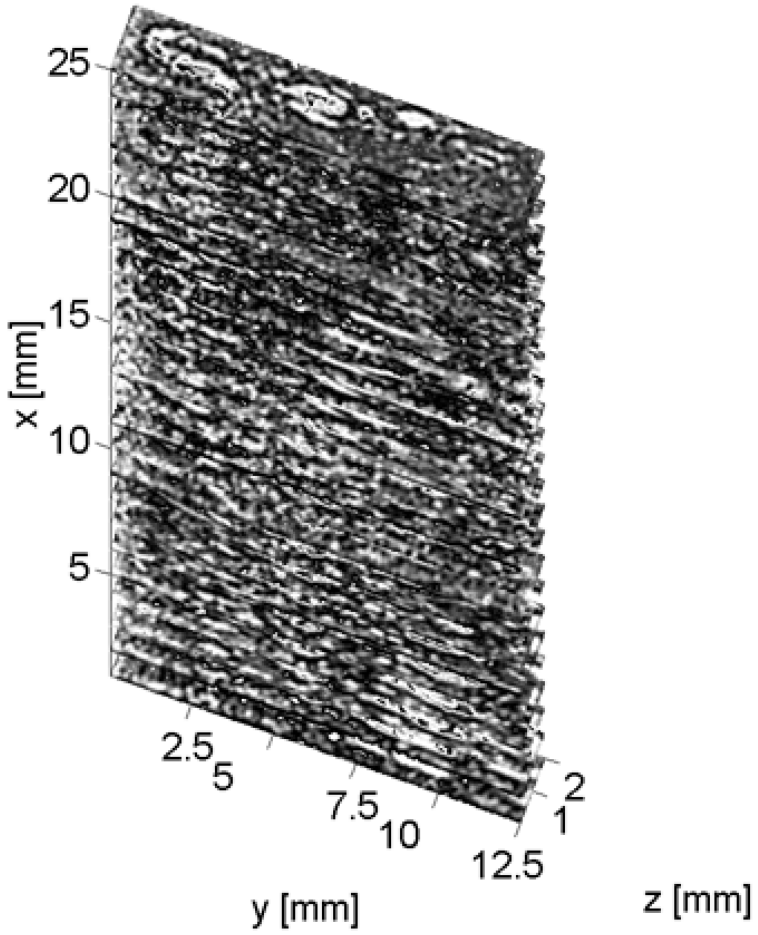

Figure 4.8: Sequence of x-ray images, PP-LGF50, transverse to the main direction of flow

The three-dimensional microstructure is finally obtained by calculating iso-surfaces with equal gray-scale values. For better visualization, only fiber bundles are shown and single fibers omitted. Due to length of the fibers and the distance between two following cross-sections, good results are obtained for fibers aligned with the flow direction.

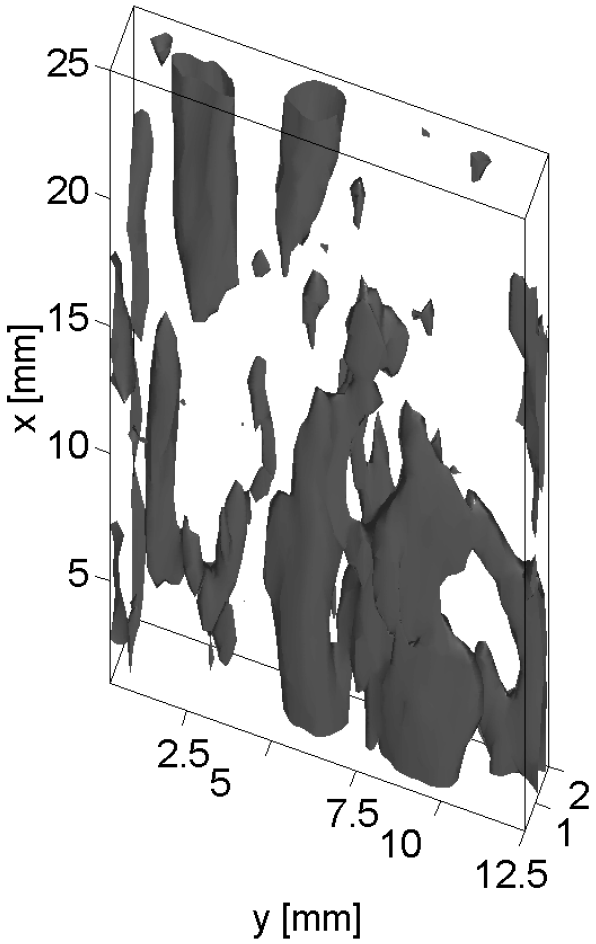

Figure 4.9: 3d Fiber orientation, PP-LGF50, transverse to the main direction of flow

However, for fibers aligned in the plane of slicing, the technique does not deliver reliable results. Decreasing the distance between two following cross-sections would help to overcome this problem.

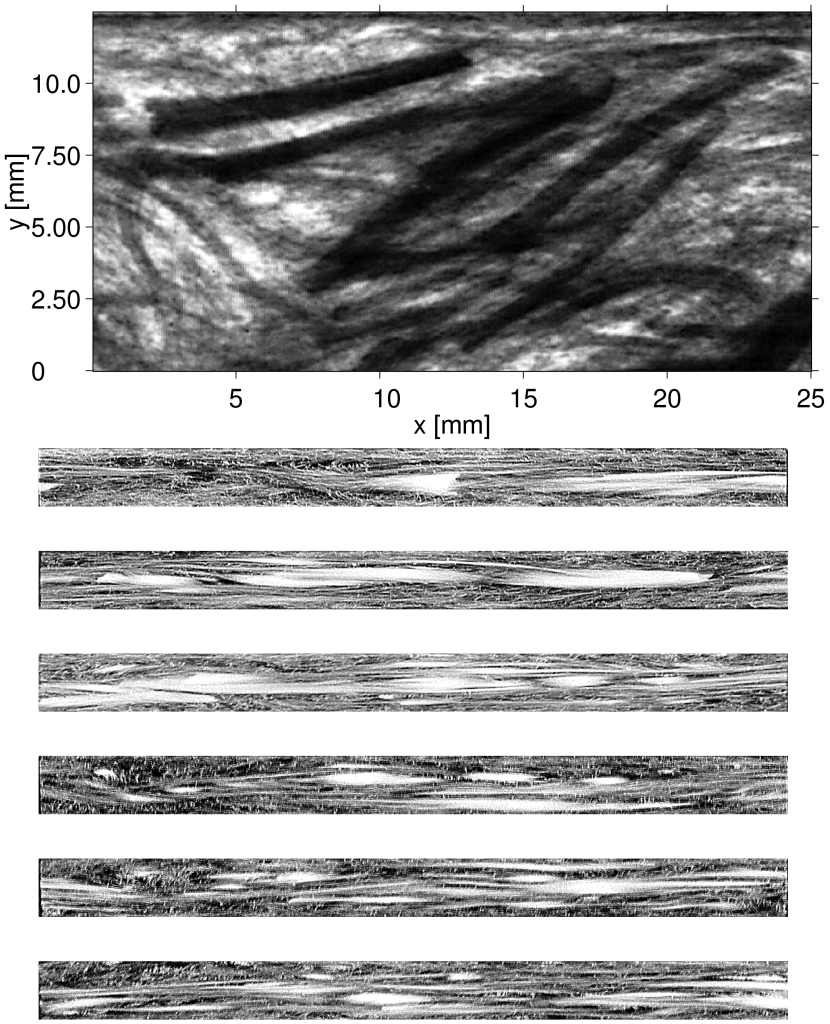

Figure 4.10: X-ray image of section evaluated parallel to the main direction of flow

With the technique proposed, the structure of long fiber reinforced thermoplastics was rebuild. The advantage of evaluating large samples is connected with a trade-off in resolution. Therefore a characterization as a mesostructural technique would be more appropriate. However, it seems possible to evaluate parts of industrial size.
Based on the three-dimensional image, it is possible to derive orientation and curvature of fibers as well as fiber length. The essential advantage of the technique is the evaluation of fiber dispersion in terms of clustering, shell-core structure and spatial variation of concentration at different locations of the finished part.
Although time consuming preparation (e.g. polishing) is not required, the technique requires accuracy in terms of image processing prior to reconstruction. All images must have the same size and differences in contrast will yield errors in fiber orientation.
The technique is still destructive, but so called non-destructive methods with adequate accuracy for capturing three-dimensional microstructure are either limited in sample size or penetration depth.
However, the technique is promising. Accuracy in capturing the microstructure could be enhanced by reducing the thickness of the cross-sections and increasing the scanning resolution. Reconstruction would also be eased by using x-ray images the cross-sections and the total image of the sample.

5 Modelling of fiber orientation dynamics

5.1 Fluid-fiber interaction

5.1.1 Motion of a single particle

The classic work on fiber orientation in shear flow originates from Jeffery [131], who studied the motion of a single, rigid, ellipsoidal particle immersed in a Newtonian fluid. Based on the assumption that inertia and gravity are small compared to friction and the presence of a constant velocity gradient in the vicinity of the particle, Jeffery stated that the particle would adopt an orientation state with minimum energy dissipation. By integrating the shear forces acting on the surface of the particle, a purely kinematic relation was derived for the particle motion.

$$\frac{D\mathbf{p}}{Dt} = -\mathbf{\Omega} \cdot \mathbf{p} + \lambda \left[\mathbf{E} \cdot \mathbf{p} - (\mathbf{p}^T \cdot \mathbf{E} \cdot \mathbf{p})\mathbf{p}\right] \tag{5.1}$$

The left-hand side of eqn. 5.1, the substantial derivative of $\mathbf{p}$ describes the translation of the centroid of the particle with the fluid

$$\frac{D\mathbf{p}}{Dt} = \frac{\partial \mathbf{p}}{\partial t} + \mathbf{v}\frac{\partial \mathbf{p}}{\partial \mathbf{x}} \tag{5.2}$$

The rotation of the particle, which is described by the right-hand side of eqn. 5.1, is driven by the velocity gradient, i.e. the vorticity tensor $\mathbf{\Omega}$ and the rate-of-deformation tensor $\mathbf{E}$. The vorticity tensor is given by

$$\mathbf{\Omega} = \frac{1}{2}\left(\nabla \mathbf{v} - \nabla \mathbf{v}^T\right) \tag{5.3}$$

while the rate-of-deformation tensor is defined as

$$\mathbf{E} = \frac{1}{2}\left(\nabla \mathbf{v} + \nabla \mathbf{v}^T\right) \tag{5.4}$$

λ depends on the geometry of the particle described by the aspect ratio $a_r = l/d$ of fiber length l and diameter d

$$\lambda = \frac{{a_r}^2 - 1}{{a_r}^2 + 1} \tag{5.5}$$

Since fibers are typically slender, a_r approaches infinity and λ yields unity. Tucker and Advani [128] showed, based on analytical solutions to Jeffery's equation, that in simple shear flow the fiber rotates quickly but periodically while remaining aligned in the main direction flow throughout the largest part

of the period. In uniaxial elongational flow, the fiber aligns in the stretching direction. Shanker modified Jeffery's equation for simulation of fiber orientation in non-homogeneous flow [206].
In order to to increase efficiency and stability of the numerical procedure, Linn [207] re-arranged eqn. 5.1 by introducing the effective velocity gradient

$$\mathbf{M} = \left(\frac{\lambda+1}{2}\right)\nabla\mathbf{v} + \left(\frac{\lambda-1}{2}\right)\nabla\mathbf{v}^T \tag{5.6}$$

This leads to the simplified but equivalent Jeffery equation

$$\frac{D\mathbf{p}}{Dt} = \mathbf{M}^T \cdot \mathbf{p} + \left(\mathbf{p}^T \cdot \mathbf{M} \cdot \mathbf{p}\right)\mathbf{p} \tag{5.7}$$

5.1.2 Macroscopic modelling of fluid-fiber interaction

In the case of processing long fiber reinforced thermoplastics with pellet dimensions of l = 10mm length and a diameter of d = 3mm, yielding a pellet volume of approximately V = 70mm^3, a total number of 8100 fibers are present given a fiber volume fraction φ = 0.26 (ψ = 0.5). A typical part volume is V = 100cm^3 which leads to a number of 11.6 million fibers which are present in the mold. Such a part made of thermoplastics filled with short fibers (l = 0.1mm to 0.5mm) would contain 200 to 1000 times more fibers.
Instead of describing the motion of each fiber on a microscopic level, it is required to model the fiber orientation dynamics macroscopically. Assuming a constant concentration of fibers, spatial homogenization leads to a distribution Ψ of fiber orientation. The Fokker-Planck equation for the distribution function then replaces the equations of motion of single particles

$$\frac{D\mathbf{\Psi}}{Dt} = \frac{\partial}{\partial\mathbf{p}} \cdot \left(\Psi\frac{D\mathbf{p}}{Dt}\right) \tag{5.8}$$

where $\frac{D\mathbf{p}}{Dt}$ represents Jeffery's equation (eqn.5.1).
The orientation of multiple fibers could be described using a probability distribution of orientation state (eqn. 5.8). A more effective way to describe fiber orientation using an orientation tensor, which could also be used in evolution equations, was introduced by Advani and Tucker [208].
The orientation tensor represents a volume averaging method and it is calculated from the product of unit vectors $\mathbf{p}$ weighted by the probability distribution Ψ, which describes the probability for a fiber oriented within a angle segment delimited by $\mathbf{p}$ and $\mathbf{p} + d\mathbf{p}$. The second-order orientation tensor $\mathbf{A}$ is defined as

$$\mathbf{A} = \oint_{S^2} \mathbf{p} \otimes \mathbf{p} \cdot \Psi \, d\mathbf{p} \tag{5.9}$$

where S^2 denotes the unit sphere. The orientation tensors are related to the coefficients in an (infinite) series expansion of the distribution function $\Psi(\mathbf{p})$. Truncating the series by using the second-order tensor $\mathbf{A}$ and the $\mathbb{A}$ was found to yield an appropriate approximation [128].
However, fiber orientation tensors are symmetric and connected to the physical orientation state. The eigenvectors of A identify the preferred orientation directions, and the eigenvalues indicate the relative probability of orientation in each of the principal directions. For example, total alignment of fibers in the x-direction ($p_2 = p_3 = 0$) yields

$$\mathbf{A} = \begin{bmatrix} 1 & 0 & 0 \\ 0 & 0 & 0 \\ 0 & 0 & 0 \end{bmatrix} \tag{5.10}$$

5.2 Fiber-fiber interaction

Jeffery's equation is only valid for a single particle and therefore limited to very low fiber fraction. In polymer processing, fiber mass fraction typically ranges between 20% to 50%. With the addition of particles, the probability of interaction between particles increases.
The effect of interaction between particles has been extensively examined in the case of rotary Brownian motion. Brownian motion describes the effect of collisions of particles in a suspension with the molecules of the fluid and the randomizing effect on particle orientation. Fibers are elongated particles and large compared to the size of molecules, hence the effects of Brownian motion on fibers is small. However, the model has been applied to the problem of fiber-fiber interaction by Hinch and Leal [209]. The evolution of orientation distribution with time is then modelled using the following Fokker-Planck equation

$$\frac{D\mathbf{\Psi}}{Dt} = \frac{\partial}{\partial \mathbf{p}} \cdot \left(\Psi \frac{D\mathbf{p}}{Dt} - D_r \frac{\partial \mathbf{\Psi}}{D\mathbf{p}} \right) \tag{5.11}$$

The interaction among fibers is taken into account using the rotary diffusivity D_r. Folgar and Tucker [210] proposed

$$D_r = C_I \cdot |\dot{\gamma}| \tag{5.12}$$

with the magnitude of the rate-of-deformation tensor and the interaction coefficient C_I. Mutel and Kamal [211] proposed a model with a constant D_r leading towards randomness when there is no deformation. With the assumption made in eqn. 5.12, orientation only changes with the presence of deformation. The interaction coefficient has to be determined empirically, for example by matching numerical predictions to experiments [91, 212]. For semi-dilute suspensions ($\dot{\phi}(L/D) > 1$), the interaction coefficient is supposed to increase with fiber fraction [210]. Ranganathan and Advani [113, 213] proposed the inverse of the average inter-fiber spacing as measure of the interaction coefficient in dilute suspensions.
However, in polymer composites, i.e. at high volume fractions, the interaction coefficient decreases with increasing fiber fraction. For short fibers ($l \leq$ 0.5mm), Bay [214] found that C_I declines with increasing fiber fraction or fiber length according to

$$C_I = 0.0184 \cdot e^{-0.7148 \cdot \varphi \cdot (l/d)} \tag{5.13}$$

In the case of long fiber reinforced thermoplastics, direct interaction between fibers ceases but hydrodynamic interaction increases [215].
With eqn. 5.12, the Fokker-Planck equation 5.11 becomes

$$\frac{D\mathbf{\Psi}}{Dt} = \frac{\partial}{\partial \mathbf{p}} \cdot \left[\Psi \frac{D\mathbf{p}}{Dt} - C_I |\dot{\gamma}| \frac{\partial \mathbf{\Psi}}{\partial \mathbf{p}} \right] \tag{5.14}$$

Using the effective velocity gradient (eqn. 5.6) one obtains

$$\frac{D\mathbf{\Psi}}{Dt} = \frac{\partial}{\partial \mathbf{p}} \cdot \left[\Psi \{ \mathbf{M}^T \cdot \mathbf{p} - \left(\mathbf{p}^T \cdot \mathbf{M} \cdot \mathbf{p} \right) \mathbf{p} \} - C_I |\dot{\gamma}| \frac{\partial \mathbf{\Psi}}{\partial \mathbf{p}} \right] \tag{5.15}$$

The evolution equation for the second-order fiber orientation tensor $\mathbf{A}$, also known as Folgar-Tucker equation, is then derived using the effective velocity gradient [207] as

$$\frac{D\mathbf{A}}{Dt} = \mathbf{A} \cdot \mathbf{M} + \mathbf{M} \cdot \mathbf{A} - \left(\mathbf{M} + \mathbf{M}^T \right) : \mathbb{A} + 2 C_I |\dot{\gamma}| \left[\mathbf{I} - 3\mathbf{A} \right] \tag{5.16}$$

From eq. 5.16 follows, that computation of the orientation tensor $\mathbf{A}$ requires an approximation of the fourth-order tensor $\mathbb{A}$. Advani [215] introduced the hybrid approximation, whereas Cintra and Tucker [216] and Dupret and Verleye [217] obtained more accurate results while spending more computational effort using an orthotropic closure and a natural closure, respectively.

5.3 Fiber-wall interaction

Figure 5.1 depicts fiber motion in Poiseuille flow near a solid wall based on theoretical equations and experimental results. Jeffery's equation, a continuum approach, assumes that the fiber rotates through the surface (figure 5.1a). Observed during experiments [141] is a *pole-vaulting* motion of a fiber near a solid wall (figure 5.1b).

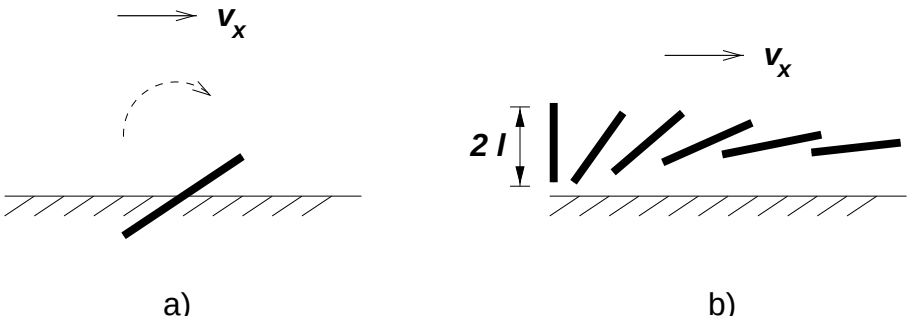

Figure 5.1: Fiber motion near a solid wall

Fiber motion near a planar wall was investigated using a planar shear flow apparatus (s.fig. 5.2). Jeffery's equations were verified in the absence of wall effects for different gap-widths. Experimental data were in excellent agreement with theoretical predictions when the fiber is located greater than a fiber length from the wall.
In regions less than a fiber length and greater than a fiber diameter, the fiber experienced an increased rate of rotation which can be modelled as a logarithmic increase in effective shear rate with decreasing separation distance. This effective shear rate is a function of the fiber's aspect ratio and its distance from the wall. Decreasing the distance of separation, or increasing the aspect ratio of the fiber, increases the wall effect.
Once the fiber aligned in the flow direction, it ceased to rotate within the field of view. In this orientation, the wall had a stabilizing effect on the fiber; here, it is suggested that the effective shear rate felt by the fiber was not as high as when the fiber was perpendicular to the wall, so it did not rotate as quickly. No fiber migration was observed for any location in the flow field. Results suggest that higher aspect ratio fibers rotate faster near the wall than those with lower aspect ratio.

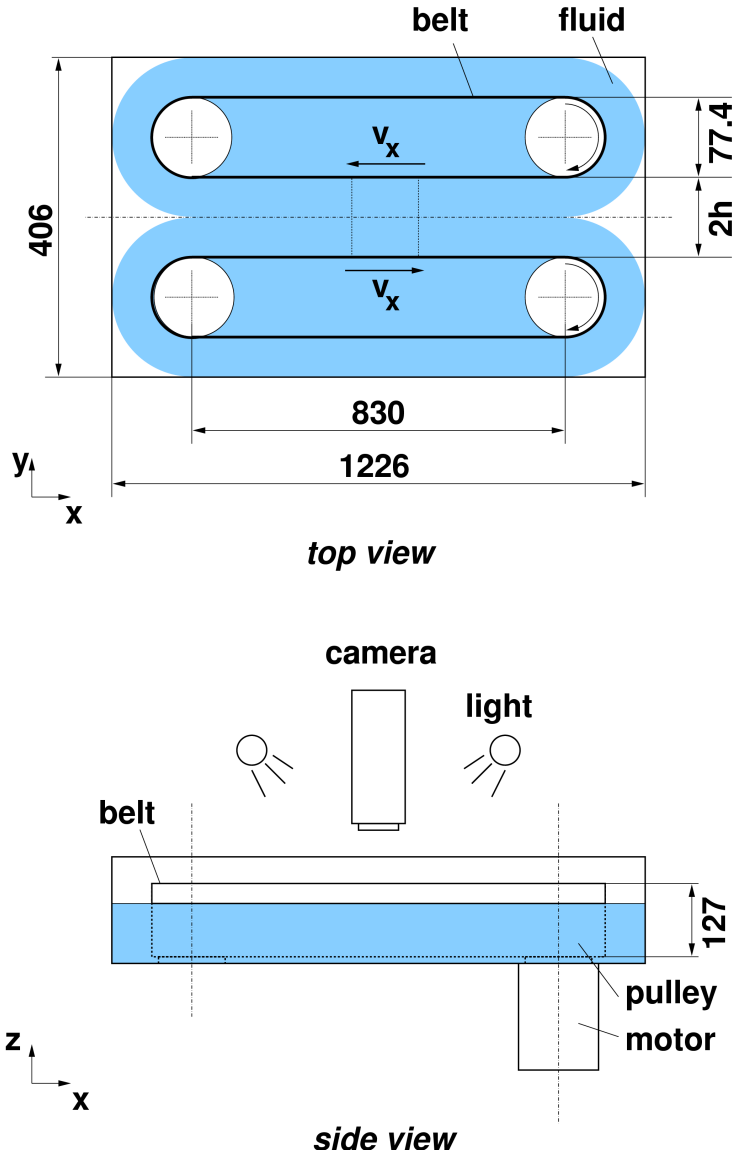

Figure 5.2: Shear flow apparatus for investigation of fiber motion near a solid wall

In order to provide further insight into the increased shear rate experienced by a fiber when it is located within a fiber length of a solid wall, fiber-wall interactions were modelled analytically. A translation model [218] was used to justify that a fiber oriented perpendicular to the wall experiences a higher effective shear rate than a fiber oriented parallel to the wall at the same separation distance. From this model, it is evident that the orientation of the fiber determines the angular velocity it experiences as it is placed closer to a solid wall; a fiber perpendicular to the wall rotates faster than a fiber parallel to the wall. Increasing the aspect ratio of the fiber causes an increase in the rate of rotation of the fiber and also increases the effective shear rate. Since the translation model considers the extreme cases of parallel motion of a fiber near a planar wall, it can be concluded that the wall effect is small for a fiber moving parallel to a wall at any orientation when its center of mass is greater than a fiber length away from the wall. Indeed, these qualitative trends were observed experimentally.

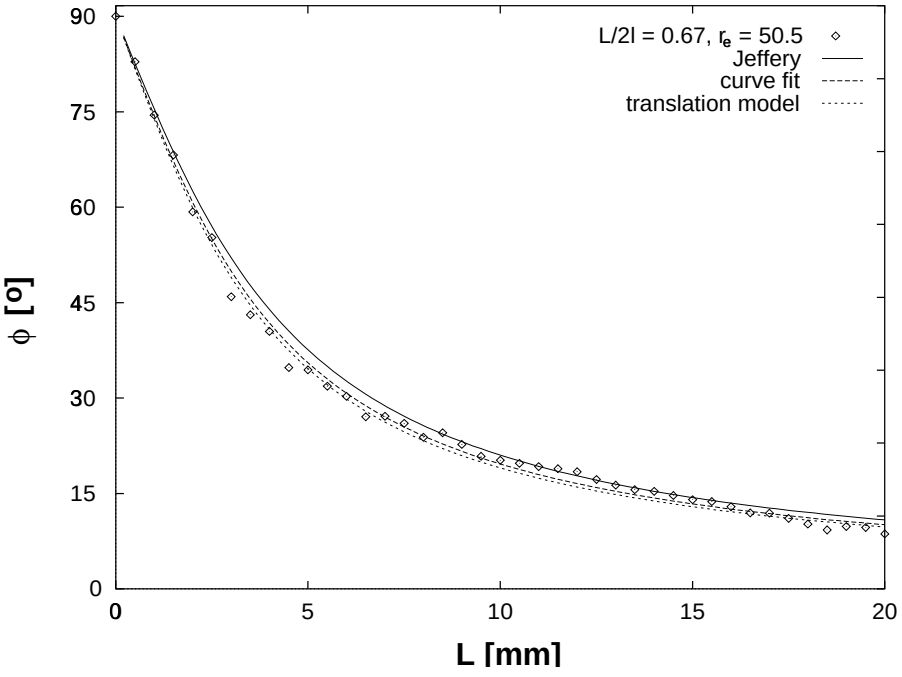

Figure 5.3: Evolution of experimental and predicted fiber orientation

When compared to experimental data, the translation model provides a very good estimate of the increased shear rate experienced by the fiber when it is located closer than two third of a fiber length from a planar wall (fig. 5.3). When applied outside this region, the model under-predicts the shear rate experienced by the fiber because it does not account for the presence of two walls bounding the fluid. Also, the model may not be applied when the fiber is within a few radii of the wall, since the flow in this region cannot be determined accurately enough by a line distribution of Stokeslets. The translation model is not universal; the limitations of this model must be considered before it is applied to various geometries.

In conclusion, based on the experimental investigation it was found that wall effects could be modelled using Jeffery's equation if an increased effective shear rate is used. The translation model allows one to quantify the increase in shear rate experienced by the fiber due to the presence of a wall in the flow field.

6 Three-dimensional simulation of the injection molding process

6.1 Modelling of the injection molding process

6.1.1 Mold filling

Simulation of mold filling in injection molding requires the numerical solution of the equations for mass conservation, momentum balance and energy balance simultaneously. The pattern of these equations depends on the rheological properties of the suspension.
For nearly incompressible fluids, mass conservation is given as

$$\nabla \cdot \mathbf{v} = 0 \tag{6.1}$$

The momentum balance is expressed

$$\rho \frac{D\mathbf{v}}{Dt} = -\frac{\partial p}{\partial \mathbf{x}} + \frac{\partial}{\partial \mathbf{x}} \cdot \left(\eta(T, \dot{\gamma}) \frac{\partial}{\partial \mathbf{x}} \otimes \mathbf{v} \right) \tag{6.2}$$

The energy balance equates heat convection on the left-hand side to the heat conduction and a source term which accounts for dissipation

$$\rho c_p \frac{DT}{Dt} = \frac{\partial}{\partial \mathbf{x}} \cdot \left[k \frac{\partial T}{\partial \mathbf{x}} \right] + \eta \dot{\gamma}^2 \tag{6.3}$$

Due to the presence of the viscosity depending on both shear and temperature, the problem becomes non-linear. For mold filling a commercial package, SIGMASOFT® by SIGMA Engineering GmbH, Aachen [165], is used. The solver is fully three-dimensional. Free-surface flow is accounted for using a Volume-of-Fluid technique.

6.1.2 Fiber orientation

A simulation module, based on the model proposed by Folgar and Tucker, has been developed for calculating the three-dimensional fiber orientation at the Institute for Applied Mathematics (ITWM, [207]). The module accesses the variables computed by the mold filling package via an application programmer's interface (API).

The fourth-order fiber orientation tensor was calculated using the hybrid closure approximation. Fiber orientation simulation was performed based on an operator splitting scheme. First, the fiber motion due to convection is calculated and then orientation due to rotation is derived. Depending on the region of interest, different numerical schemes for the core zone (Euler) and the skin zone (Runge-Kutta) are employed. The normalized condition for the fiber orientation tensor in three-dimensional flow is satisfied using a penalty term.

6.2 Process simulation

6.2.1 Pre-processing

The model is either generated interactively, based on batch scripts or from CAD data via the STL interface. Mold and inlets can easily be modelled. The definition of sensors for pressure or temperature and tracer particle locations is also possible.
Mesh generation with octahedral elements is performed automatically. The use of a standard and an advanced modus allows for mesh refinement in regions of special interest. For both the standard and advanced algorithm, the preferred element size can be declared. Mesh quality can also be triggered by defining the ratio of dimensions between neighboring elements or within the element itself. The mold is also represented by octahedral elements, the meshing of the transition zone between part and mold can also be defined. Octahedral elements provide the element type and accuracy required by subsequent structural analysis [219].

6.2.2 Material properties

A major advantage of existing commercial packages, e.g. MOLDFLOW® is their extensive materials database where the properties of more than four thousand grades are stored [220]. For a preliminary analysis, the use of existing data is helpful and sufficient. With permanently emerging polymer grades and for a detailed analysis, especially for fiber reinforced materials, it is recommended to perform a rheological characterization on the material dedicated for processing.
The definition of temperature-dependent thermal and rheological properties, is essential for increasing the accuracy of the simulation. In the case of rheological properties, data for viscosity was available for different fiber fraction in a wide range of temperature, as pointed out in section 3.5. The rheological data was defined using a power-law type relationship for shear viscosity.

Thermal data such as specific heat capacity, thermal conductivity or pvT data was either measured or derived as a function of temperature (s. appendix C).

6.3 Comparison between simulation and experiment

6.3.1 Rheology

In a first step, the experimental results obtained by rheometry were validated by comparing pressure and temperature recorded during extrusion to the values obtained by simulation using the 3D simulation package. Transient simulation of the injection molding process with free surface was conducted using symmetric models based on the channel geometry as used during the experiments (s. fig 6.1). Pressure and temperature was recorded using control points at the sensor locations.

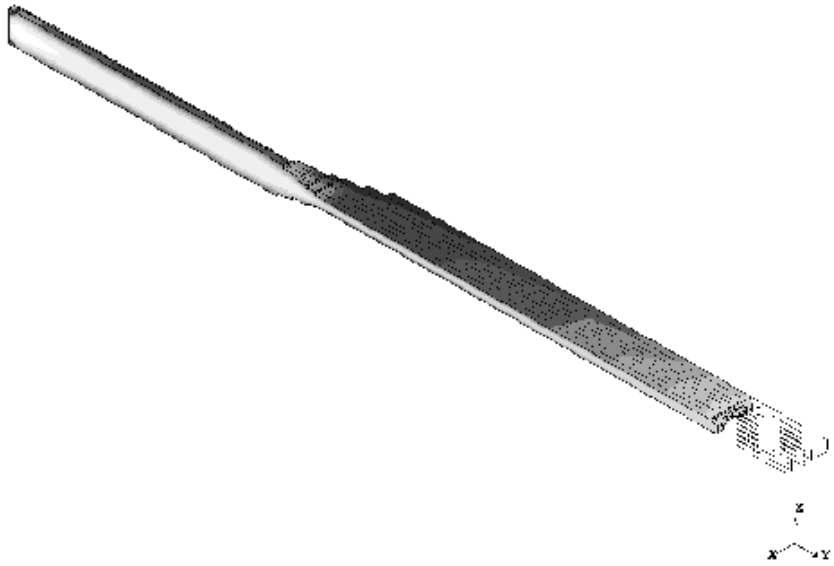

Figure 6.1: 3D mold filling of the rheometer (symmetry in yz-plane)

6.3.1.1 Temperature Profile

Results of the thermal analysis during simulation of mold filling deviate from the values experimentally derived with largest error found for PP-LGF50, as depicted in fig. 6.2. It was generally found that, at low shear rates, the temperature rise is under-predicted while at elevated shear rates, results obtained by simulation yield higher values than measured.

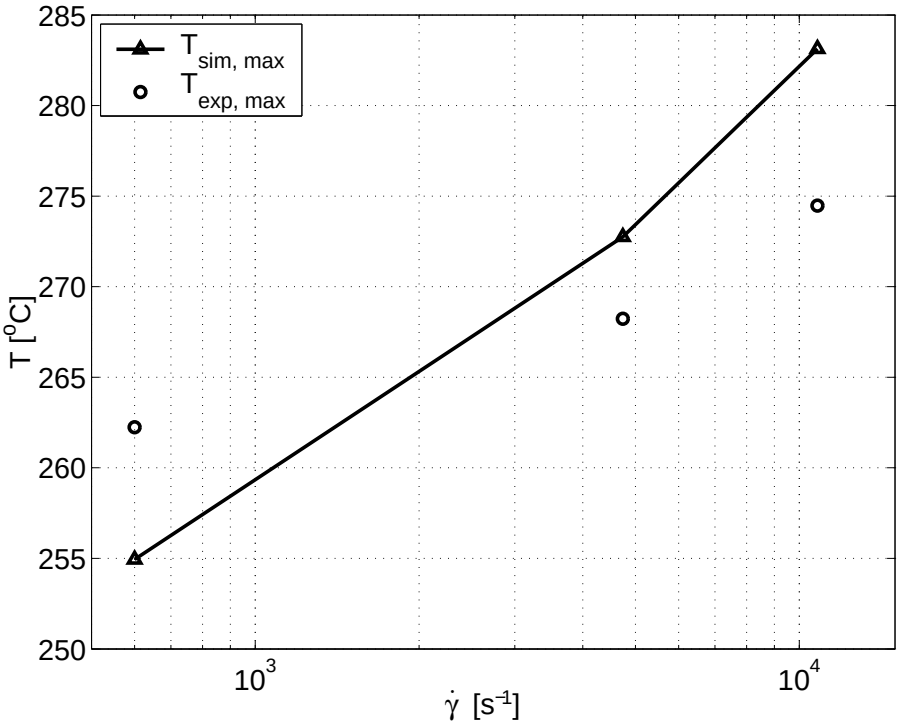

Figure 6.2: Temperature profile, PP-LGF50, T = 250^{o}C

As discussed in section 3.6.3, the temperature rise is over-predicted using the energy balance equation indicating that the viscosity values derived were too high. However, an uncertainty remains in terms of heat transfer coefficient between the melt and the cavity walls. The error in calculation of the temperature distribution induces subsequent errors.

6.3.1.2 Pressure Profile

Comparing the pressure values obtained for both experiment and simulation shows good agreement for PP-LGF50 at high shear rates (fig. 6.3). At low shear rates, the results of the simulation yield lower values than experimentally recorded. For a lower melt temperature, the accuracy of the results obtained from simulation declines. This mainly due to the error in thermal analysis induced by dissipation which is more pronounced for low melt temperature and high viscosity. For neat polypropylene, the agreement between simulation and experiment improves further with exactly matching results obtained at intermediate flow rate.

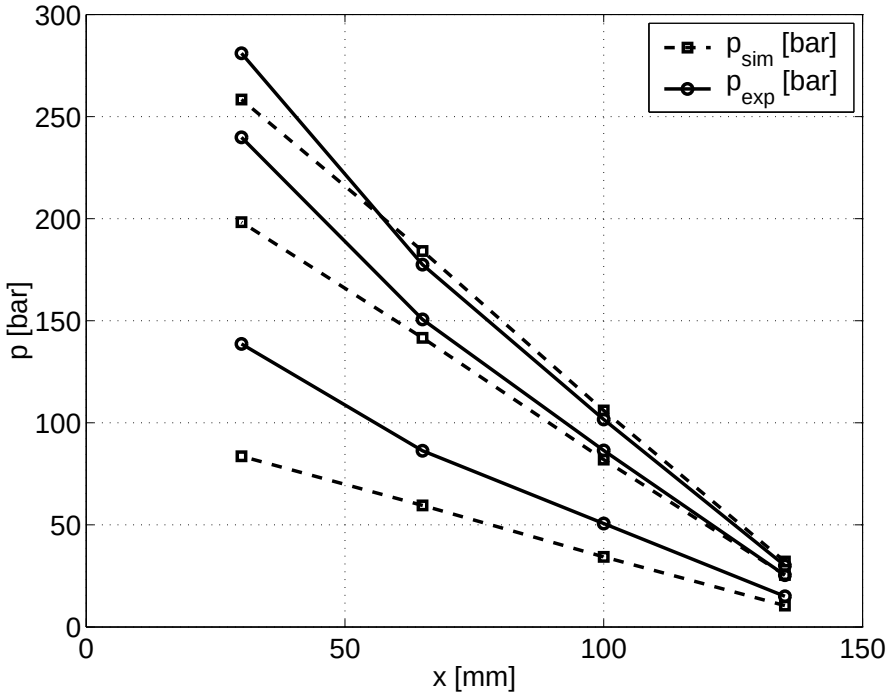

Figure 6.3: Pressure profile, PP-LGF50, T = 250^{o}C

It is evident that entrance pressure drop is not captured, with error growing with fiber fraction. At the entrance, stretching occurs transverse to the main direction of flow. Therefore fiber orientation and extensional viscosity become important.

6.3.2 Microstructure

6.3.2.1 Verification of fiber orientation prediction

The accuracy of the numerical predictions are typically verified using different flow fields for which the analytical solution of the probability density function (denoted as DFC) is known. An extensive comparison of different closure approximations to the analytical solution is available in [216]. Since the hybrid closure approximation (HYB) is used here for prediction of fiber orientation [207], we compare it with the analytical solution as well as with results former obtained using the hybrid closure (HYB', [208]). In all calculations, a value of C_I = 0.01 is used.

6.3.2.1.1 Simple shear flow

The first test example is simple shear flow ($v_x = G, v_y = v_z = 0$) between two parallel walls. The evolution of fiber orientation tensor components a_{11} and a_{22} is plotted versus normalized time $G \cdot t$ (s. fig. 6.4).

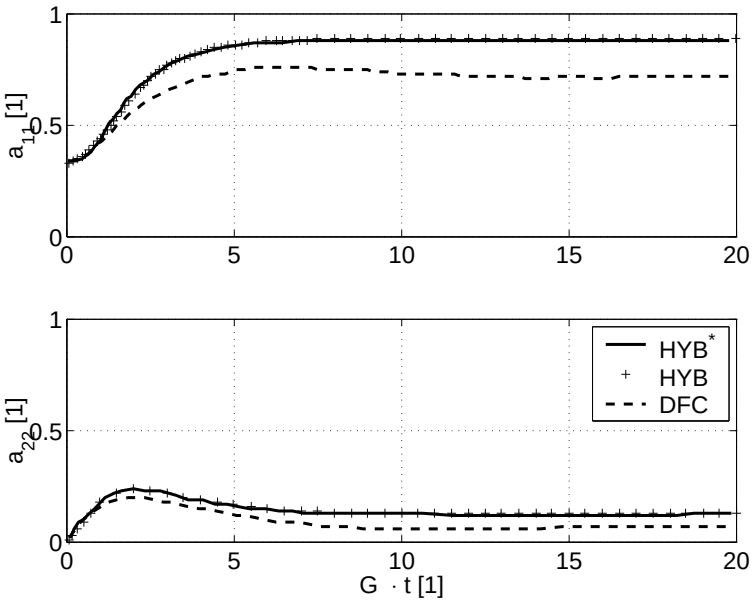

Figure 6.4: Tensor component a_{ij} in simple shear flow

The predictions with the currently developed code match exactly the results found in literature for the hybrid closure. Good agreement with the analytical solution is achieved. However, the values obtained for both a_{11} and a_{22} are higher than the results of the analytical solution, leading to an over-predicted degree of alignment.

6.3.2.1.2 Shearing and planar stretching flow

The second test example is a combination of shear flow in the xz-plane superposed by planar stretching (magnitude E in the xy-plane ($v_x = -Ex+Gz, v_y = -Ey, v_z = 0$) with G/E = 10.

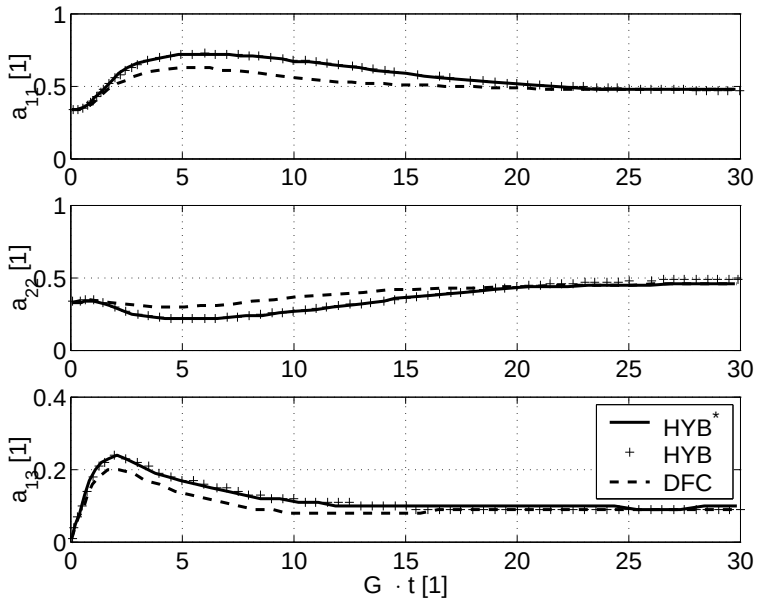

Figure 6.5: Tensor component a_{ij} shear and planar stretching flow

As depicted in fig. 6.5, good agreement is achieved. In this case a_{11} and a_{13} are over-predicted while a_{22} is lower than the analytical solution. The difference between analytical solution and hybrid closure approximation diminish with time.

6.3.2.1.3 Center gated disk

The third example is flow in a disk with a gate located at the center of the disk. The flow field is dominated by radial flow.

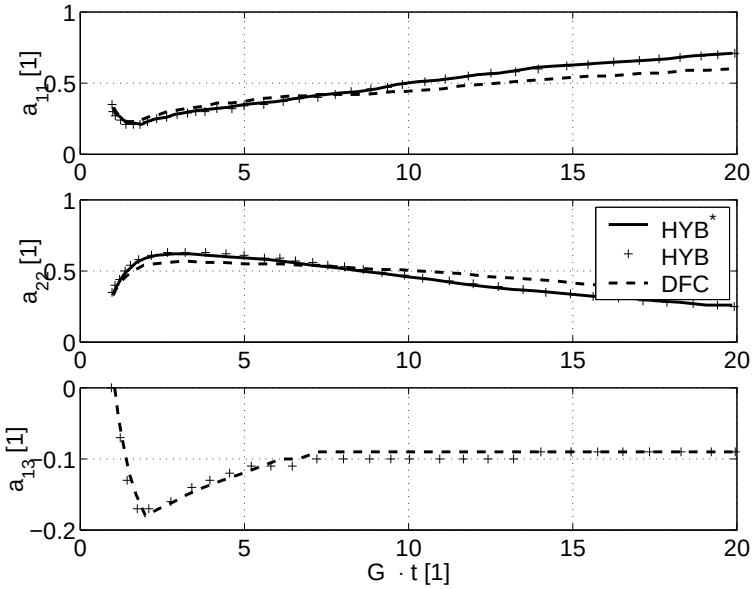

Figure 6.6: Tensor component a_{ij} for flow in a center gated disk

The hybrid closure again yields higher values for a_{11} and a_{13}. For a_{22}, the analytical solution is under-predicted but then over-predicted with time. Generally, it is found that the hybrid closure approximation tends to yield a degree of alignment which is slightly higher than the predictions obtained using the analytical solution. This effect could be alleviated using higher values of C_I.

6.3.2.2 Influence of C_I on 3D fiber orientation

The three-dimensional fiber orientation in the modular die as calculated using an interaction coefficient of C_I = 0.01 is depicted in fig. 6.7. The plot is symmetric with respect to xz- and the xy-plane so the core zone is located in the lower front section of the plot.

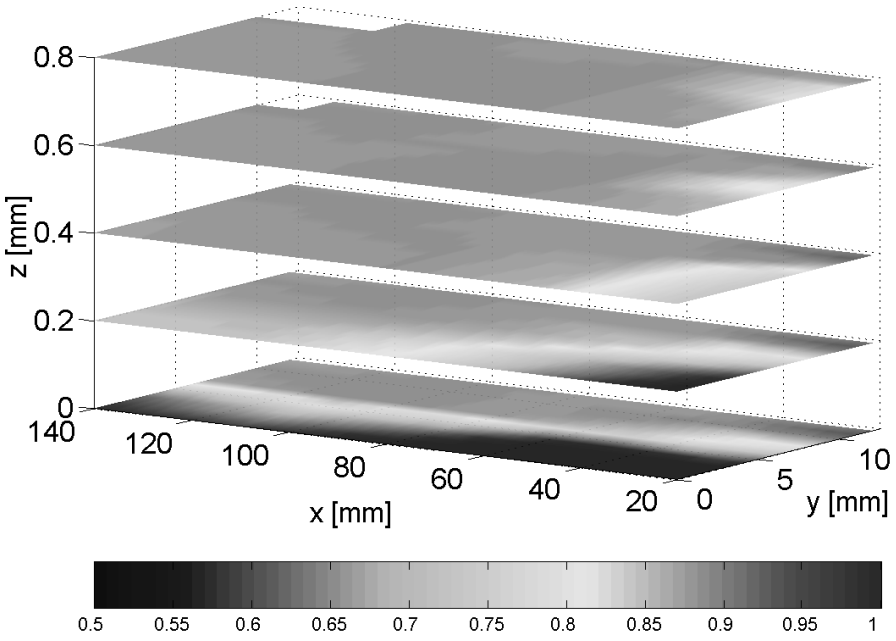

Figure 6.7: Tensor component a_{11} for interaction coefficient C_I = 0.01

Preferred alignment in the flow direction (x axis) is calculated with a maximum of $a_{11} \simeq 0.9$. In the core zone, which accounts for only one fifth of the total cavity height, random orientation with $a_{11} \approx 0.5$ is observed.

Reducing the interaction coefficient from C_I = 0.01 to C_I = 0.001 leads to perfect alignment in the main direction of flow whereas the random orientation in the core zone remains.

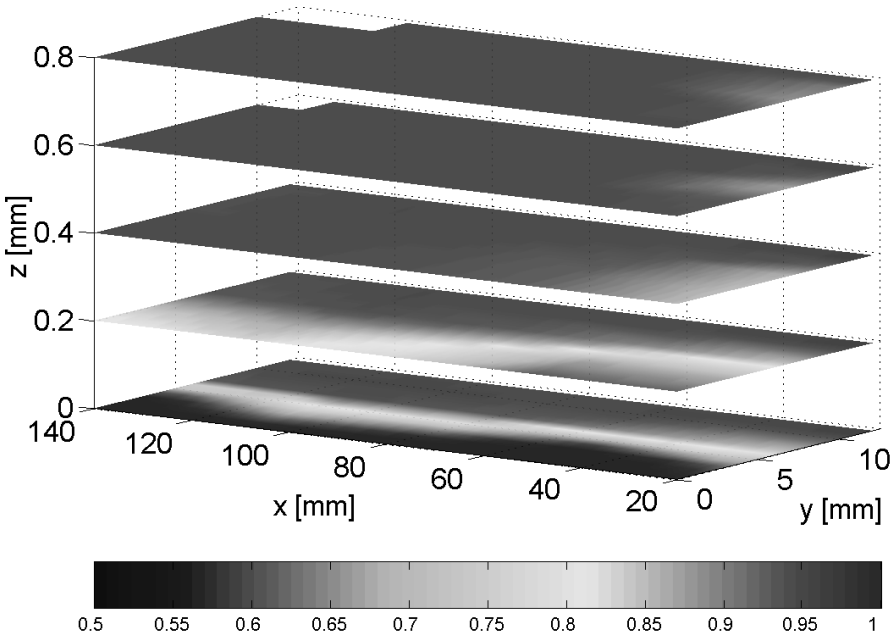

Figure 6.8: Tensor component a_{11} for interaction coefficient C_I = 0.001

6.3.2.3 Interaction coefficient for PP-LGF

The interaction coefficient is an empirical parameter which has to be determined by comparing experimental to calculated results. A total number of 150 control points, given by 25 control points in-plane and 6 across the thickness is used during simulation. Fiber orientation values were averaged through the thickness, since experimental results for fiber orientation from x-ray images were available as two-dimensional data only. The specimens were divided into 25 areas in the xy-plane with a bias from the center to the wall. The 2D fiber orientation was then evaluated by image processing. The standard deviation σ_{a_11} in fiber orientation (i.e. a_{11}) is then derived from the difference between simulation and experiment at 25 points.
The effect of the interaction coefficient on fiber orientation for fiber fractions of 30% and 50% is depicted in fig. 6.9.

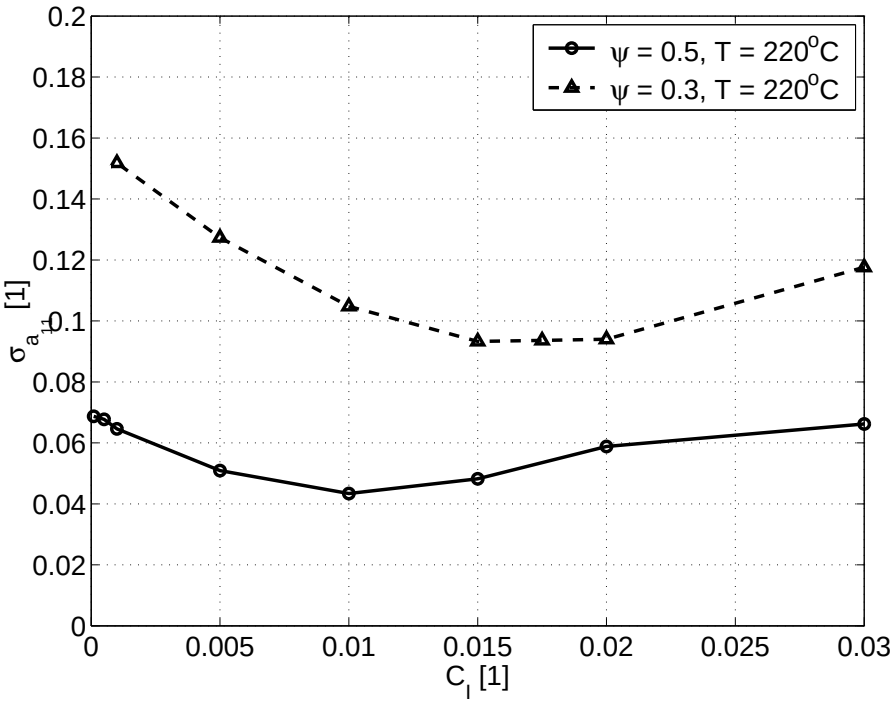

Figure 6.9: Standard deviation between simulation and experiment in tensor component a_{11} versus interaction coefficient C_I and fiber fraction ψ

For PP-LGF50, an interaction coefficient 0.05 $\leq C_I \leq$ 0.15 provides good agreement in mean fiber orientation between simulation and experiment. For a fiber fraction of 30% a best value between 0.15 and 0.2 is found. Using these values, a standard deviation in fiber orientation between simulation and experiment in the order of 5% and 9% can be achieved.
Increasing melt temperature and hence reducing viscosity requires an adjustment of the interaction coefficient. For a melt temperature of 250^{o}C, an interaction coefficient between 0.15 and 0.25 would yield a standard deviation in the order of 10% (s.fig.6.10).

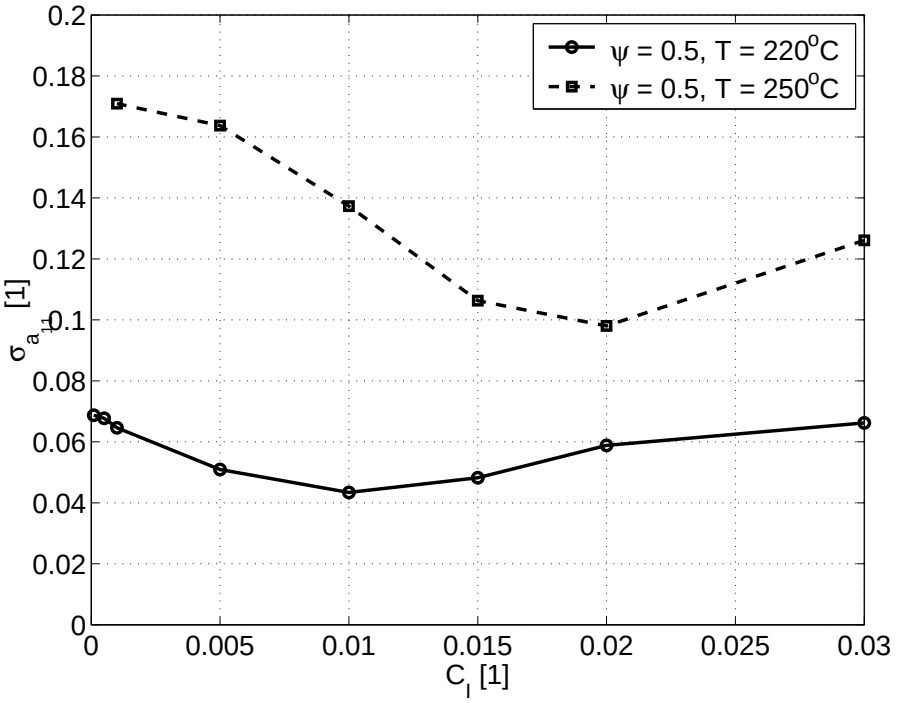

Figure 6.10: Standard deviation between simulation and experiment in tensor component a_{11} versus interaction coefficient C_I and melt temperature T

The results of these exemplary comparison are compiled in 6.1. The interaction coefficient increases with temperature and declines with fiber fraction. Hence, the interaction coefficient does not only depend on materials parameters but also on processing conditions. This affirms the statement of Tucker and Advani [221] that the rotary diffusivity, i.e. the interaction coefficient, is a material property depending on the size of the particles and on the viscosity and temperature of the surrounding fluid.

ψ [1]	T [^{o}C]	C_I [10^{-2}]
0.5	220	0.005 - 0.015
0.3	220	0.015 - 0.020
0.5	250	0.015 - 0.025

Table 6.1: Interaction coefficient vs. fiber fraction and melt temperature

The increase in interactions at intermediate fiber fraction when compared to high volume fraction is a well-known effect since the degree of freedom in orientation declines with decreasing inter-fiber spacing. Especially for long fibers, parallel orientation is the only possibility to achieve high volume fractions.

The effect of melt viscosity on fiber-fiber interaction is also plausible. Since the viscosity of polymer decreases with temperature, fibers are subject to a limited force and torque and therefore the aligning effect of shear flow is reduced.

6.3.2.4 Effective aspect ratio for PP-LGF

Since the fiber aspect ratio a_r is explicitly used in terms of $\lambda = ({a_r}^2 - 1)/({a_r}^2 + 1)$ during the simulation of fiber orientation, the effect of fiber length on fiber orientation was examined. Vice versa, the aspect ratio can be estimated for a best match between experimental and numerically predicted fiber orientation. The effective aspect ratio is derived as minimum aspect ratio, at which no further improvement in standard deviation of the fiber orientation tensor components is achieved.

From simulation it is found, that the standard deviation declines significantly with increasing values of λ. For PP-LGF50, lowest values are obtained at λ = 0.9995, which corresponds to an aspect ratio of a_r = 63. This calculated aspect ratio yields the lower bounds of the aspect ratio as derived from the prediction and comparison of extensional viscosity.

6.4 Application

6.4.1 3D effects in injection molding

In order to demonstrate three-dimensional effects in injection molding of fiber reinforced thermoplastics, a plaque with ribs parallel and transverse with respect to the main direction of flow was chosen corresponding to previous studies [91, 159, 212]. In this example, PC filled with short glass fibers by a weight fraction of 30% is injected at a melt temperature of 321^{o}C into the mold with a constant temperature of 90^{o}C. The temperature distribution during mold filling is depicted in fig. 6.11. Symmetry is assumed with respect to the xz-plane.

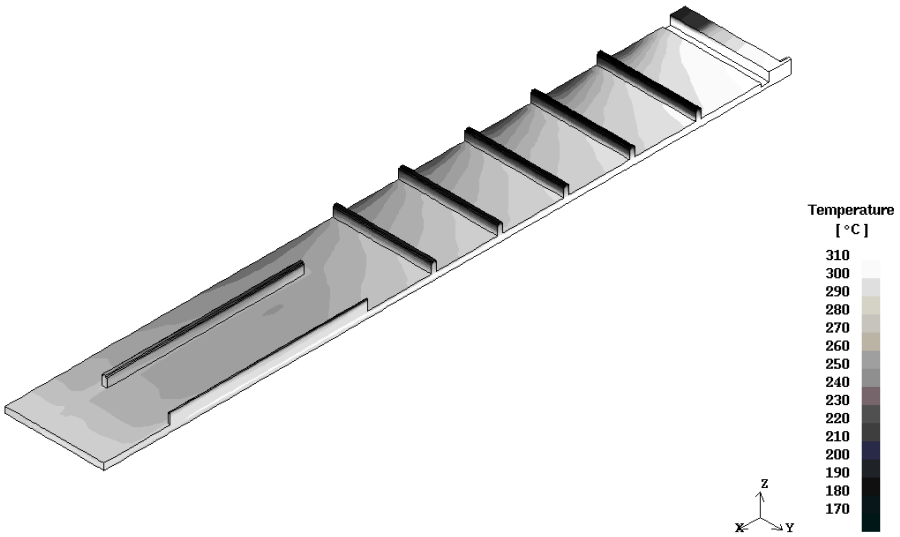

Figure 6.11: Temperature distribution, rib plaque

The materials data was taken from the original publication [212]. For the suspension, a carreau-type constitutive law was assumed. The interaction coefficient was C_I = 0.0035.

During mold filling, the melt enters the mold at the gate (top right), hits the wall and recirculates, especially in the corners, in the distribution chamber. Once the chamber is filled, the melt enters the actual cavity with a quasi-parallel flow front. The flow front is quickly disturbed due to freezing of the melt at the mold surface (top, bottom and side) and the diverging flow at the rib locations.
The shear rate distribution (fig. 6.12) shows the interaction between thermal boundary conditions and flow properties.

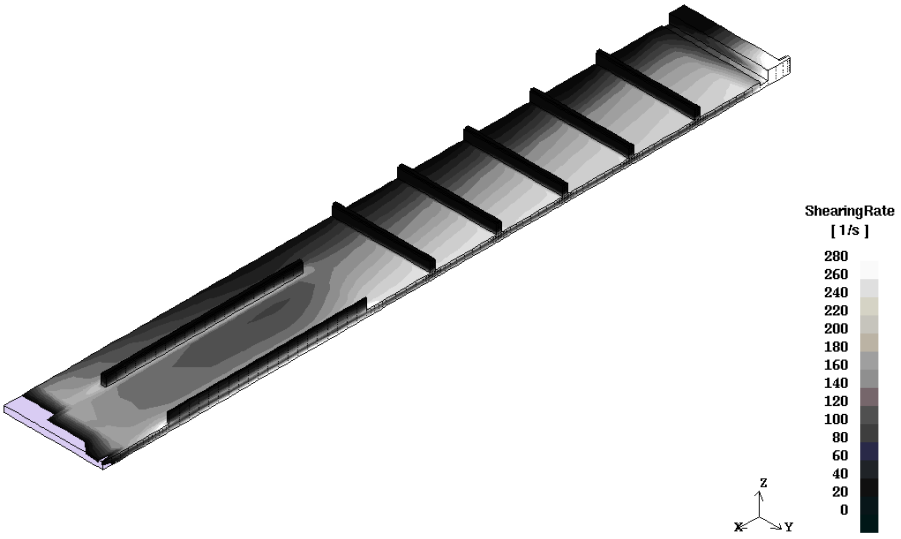

Figure 6.12: Shear rate distribution, rib plaque

As the cooling rate is highest in the ribs, due to the small ratio of melt volume to mold surface the melt is already frozen and flow is limited to the planar section.
The distribution of shear rate leads to the fiber orientation depicted in fig. 6.13. In the panel, the typical skin-core structure is observed with high alignment in the flow direction in the skin zone ($a_{11} \simeq 1$). Random orientation ($a_{11} \simeq 0.5$) with slightly increased transverse alignment is observed in the center of the transverse ribs, the core of the flow front and at the top and center of the distribution chamber.
In the remaining sections with random alignment, the transverse ribs (side and top section), the tips of the parallel ribs and the core of the distribution chamber, fiber orientation is dominated by the a_{33} component (fig. 6.14).

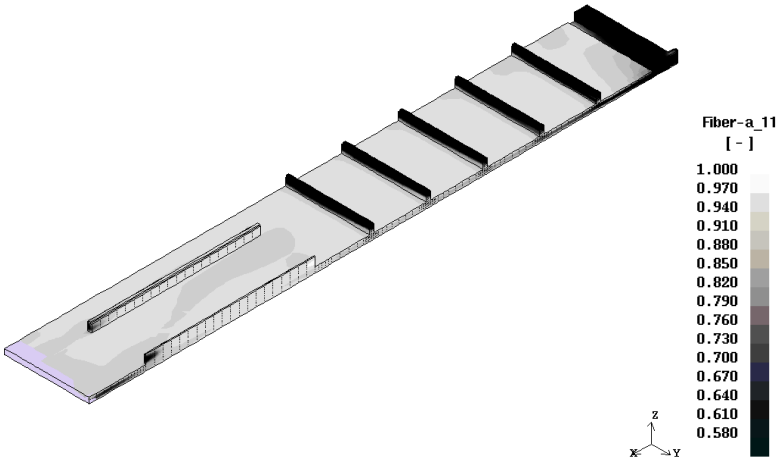

(a) Fiber orientation tensor, component a_{11}

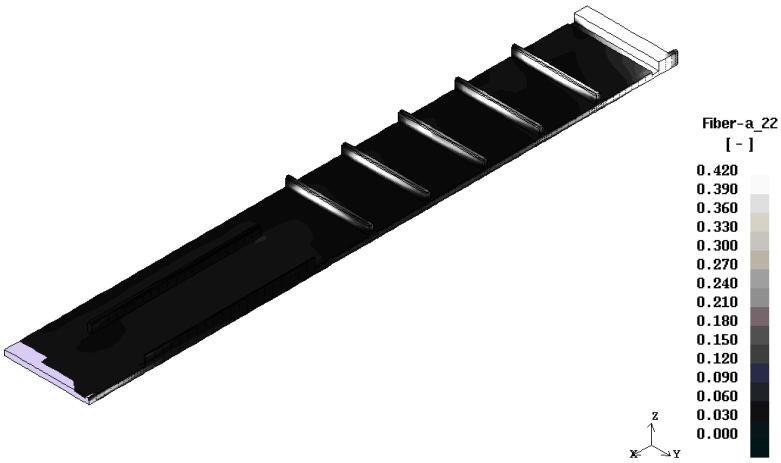

(b) Fiber orientation tensor, component a_{22}

Figure 6.13: Fiber orientation tensor, component a_{11} and a_{22}

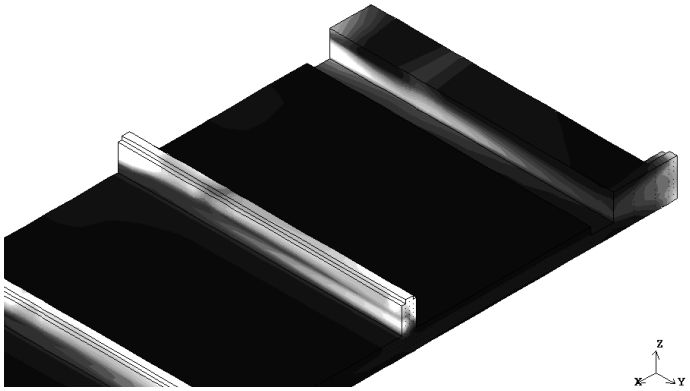

(a) Fiber orientation tensor, tensor component a_{33}, transverse rib

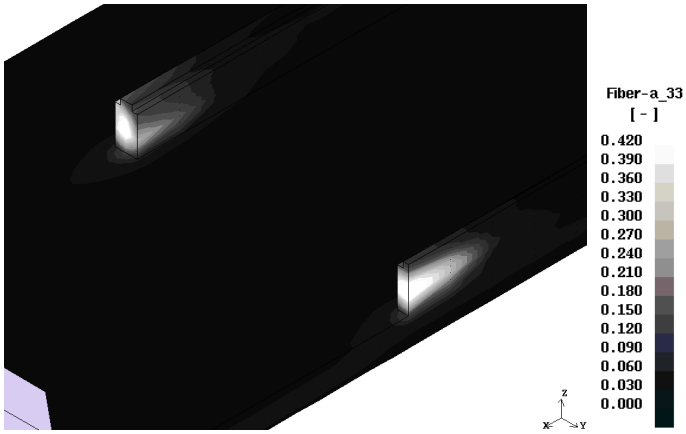

(b) Fiber orientation tensor, tensor component a_{33}, flow direction rib

Figure 6.14: Fiber orientation tensor, tensor component a_{33}

6.4.1.1 Fountain flow

During mold filling, the typical skin-core structure in shear rate distribution is not found at the flow front. While the no-slip boundary condition holds at the cavity walls, the melt surface is free of shear stress at the flow front, and the melt recirculates resulting in fountain flow [222]. Fountain flow typically occurs in regions which yield the dimensions in the order of the cavity height [223]. Fountain flow is also important when tracking weld-lines, especially for fiber filled materials. The effect is enhanced by the freezing melt layer at the cavity wall (s. fig.6.15).

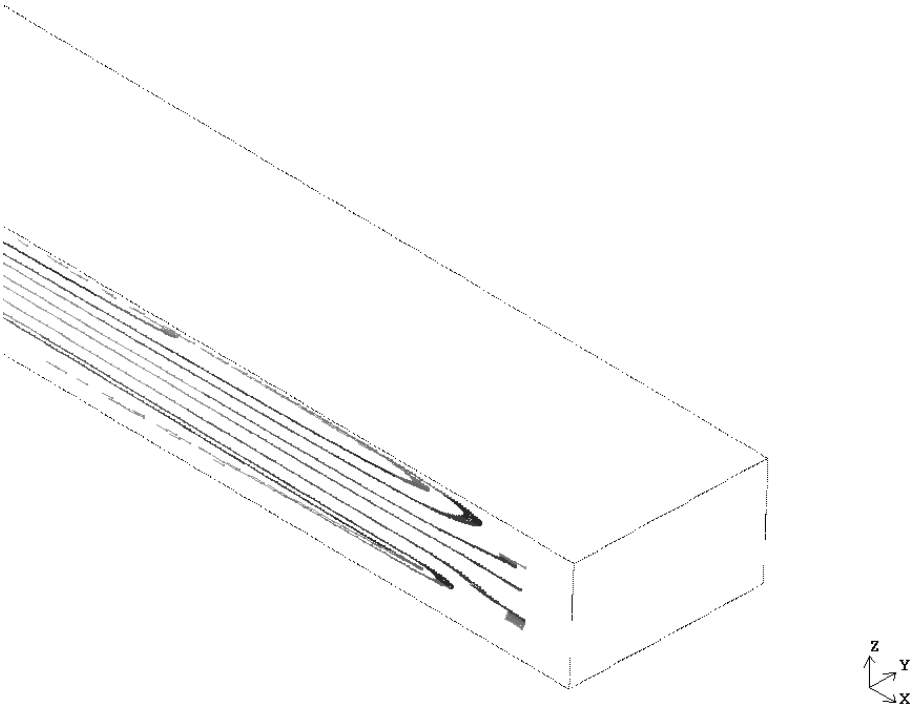

Figure 6.15: Fountain flow

6.4.1.2 Edge effect

At the edges of the ribs parallel to the flow direction (s. fig. 6.16), the shear rate is higher than in the surrounding sections. This edge effect is due to a reduction in heat transfer. Two-dimensional simulation with shell elements does not capture this effect resulting in errors in warpage prediction. For example, the error in predicting the angle between base and rib using 2D simulation can yield values up to 25% [219].

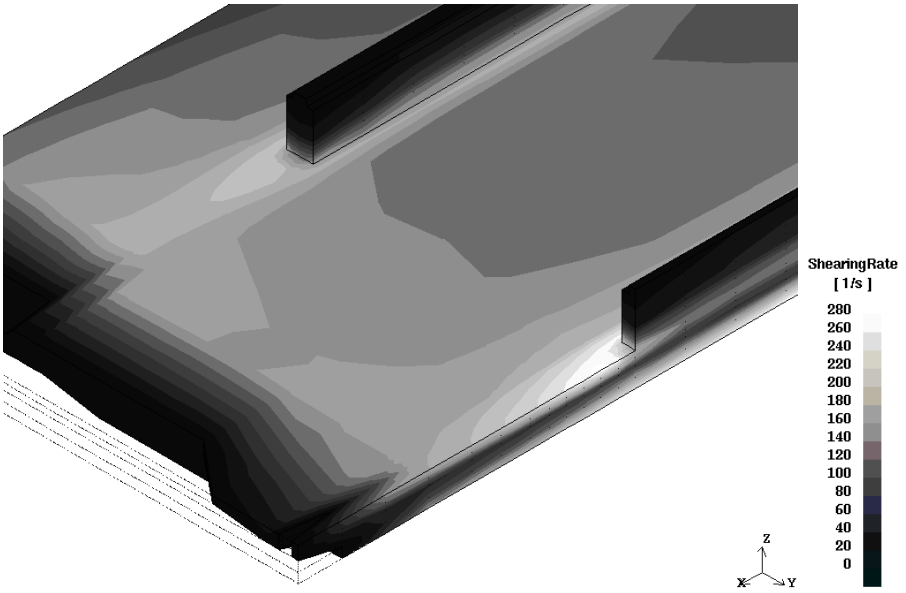

Figure 6.16: Shear rate distribution, rib plaque

From fig.6.16, the distribution of shear rate across the cavity height, resulting in the skin-core structure with respect to fiber orientation in shear flow. While the shear rate is highest close to the mold walls, the shear rate declines substantially with decreasing distance from the center of the cavity. At the flow front, the shear rate yields zero.

6.4.1.3 Effect of Ribs

3d flow is also encountered at ribs and corners, at cross-section changes. A 2D analysis means a loss in accuracy when predicting pressure distribution, residence time and orientation [161, 224]. In 3D simulation of the transverse ribs, the core zone is shifted towards the rib (fig. 6.17(a) and (b)). There is no core zone at the base of the rib (s. fig 6.17(c)). In the panel, Random orientation is observed in the upper core section and the tip of the rib (fig 6.17(d)).

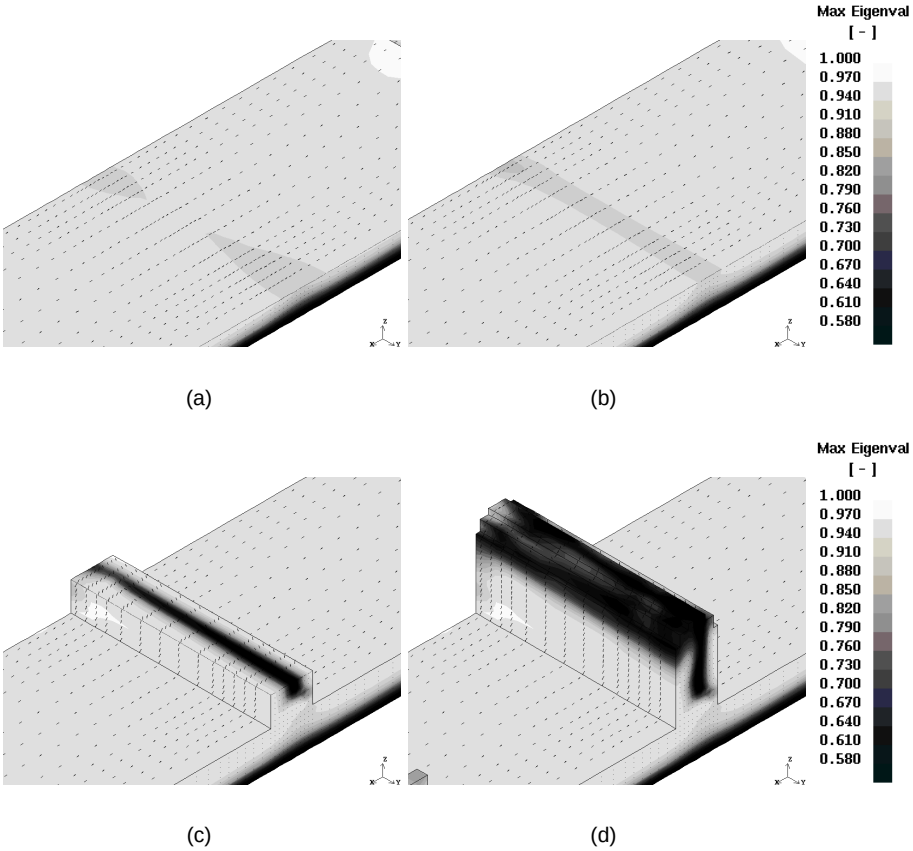

Figure 6.17: Maximum eigenvalue for fiber orientation in a transverse rib, cross-section parallel to the z-direction

From figs. 6.17 and 6.18, it can be observed that fiber orientation in a rib transverse to the main direction of flow (i.e. x) is neither symmetric with respect to the x- nor to the y-direction. The presence of the wall at $y = -W/2$, with W as the width of the plaque, counteracts against fountain flow leading to a slightly higher degree of alignment at the mold wall.

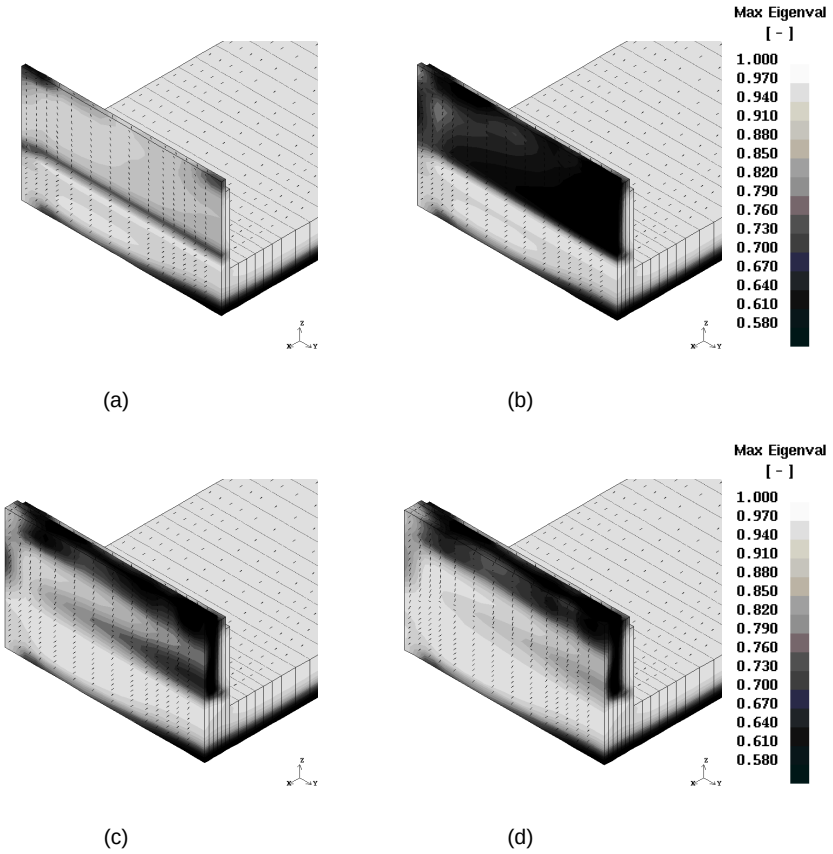

Figure 6.18: Maximum eigenvalue for fiber orientation in a transverse rib, cross-section parallel to the x-direction

Verweyst [212] compared the fiber orientation, obtained by 2D simulation (s. fig. 6.19), with experimental results [91]. Fundamentally, good agreement was achieved whereas the thickness of the core zone was underestimated.

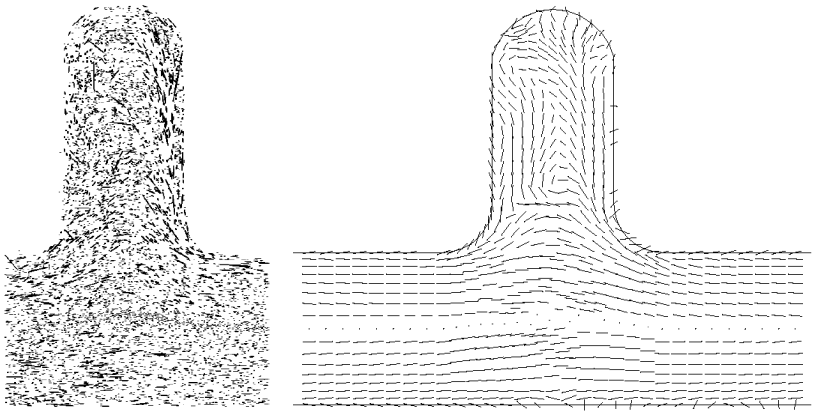

(a) Experimental fiber orientation

(b) Calculated fiber orientation

Figure 6.19: Fiber orientation in a transverse rib [91, 212]

Results obtained in this study show, that the fiber varied with increasing distance of the cross-section in the xz-plane from the side walls of the mold, as depicted in fig. 6.20(a-d). While there is virtually no core zone close to the mold wall (s. fig. 6.20(a)), the fibers in the core zone rotate until transverse orientation is obtained at the center of the mold (s. fig. 6.20(d)).
Basically, agreement with the experimental fiber orientation is also achieved. The thickness of the core zone is higher compared to the results obtained by VerWeyst. In the rib section, the fiber orientation at the base is non-symmetric but slightly shifted in the flow direction, which can also be observed in the experimental orientation. The fiber orientation in thickness direction at the base of the rib is not as strong as predicted by VerWeyst (influence of radius in meshing).

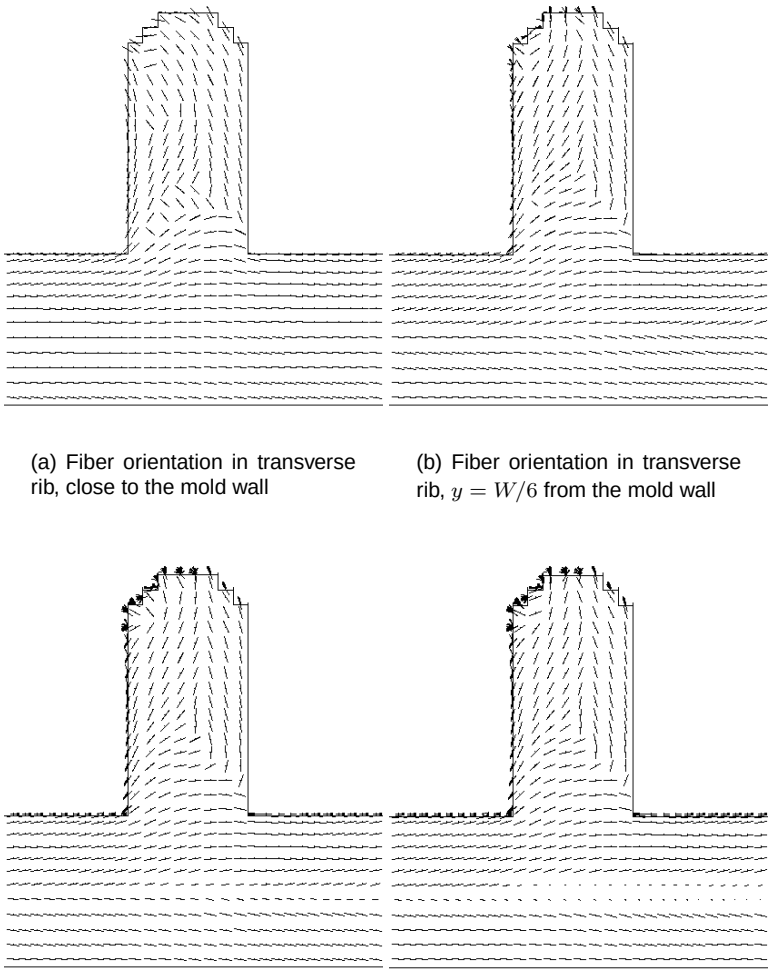

(a) Fiber orientation in transverse rib, close to the mold wall

(b) Fiber orientation in transverse rib, $y = W/6$ from the mold wall

(c) Fiber orientation in transverse rib, $y = W/3$ from the mold wall

(d) Fiber orientation in transverse rib, $W/2$ from the mold wall (center)

Figure 6.20: Fiber orientation versus wall distance

6.4.1.4 Parts with thick sections

Thick wall sections and abrupt changes in channel dimensions lead to recirculating flow [160, 165, 222, 223, 225]. Based on the distribution of shear rate (fig. 6.21(a)), a high level of alignment is obtained but at the flow front, the core zone of the panel, the rib and the distribution chamber (fig. 6.21(b)). Whereas the orientation in the core zone is dominated by a_{22} (fig. 6.21(c)), the orientation in the transverse rib and the tip of the parallel rib is mainly due to alignment in the thickness direction (fig. 6.21(d)). At the entrance, recirculating flow with transverse orientation is observed.

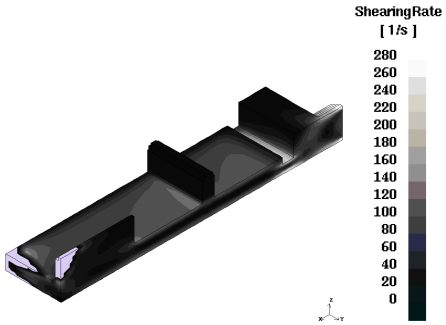

(a) Shear rate

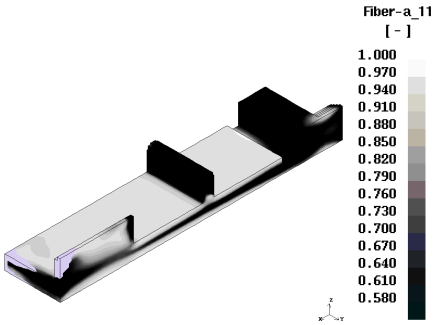

(b) Fiber orientation tensor, tensor component a_{11}

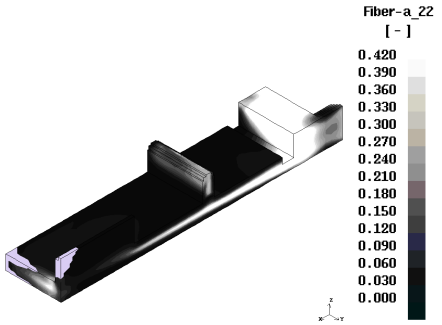

(c) Fiber orientation tensor, tensor component a_{22}

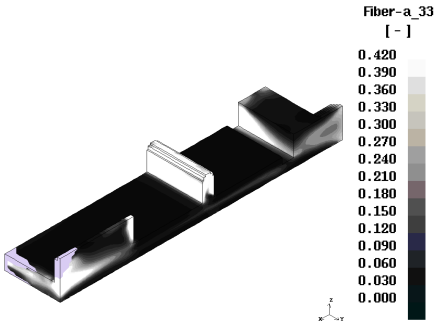

(d) Fiber orientation tensor, tensor component a_{33}

Figure 6.21: Fiber orientation in thick walled parts

6.4.2 Passenger seat component

In order to validate the suitability of the program to applications in terms of complexity and size of model, a passenger seat component formerly developed at IVW [226, 227] was chosen. The component was originally molded from PA6.6 reinforced by glass fibers (CELSTRAN® by TICONA) with an initial length of 10mm and fiber fraction of 50% and 60% by weight, respectively. The melt was injected at a barrel temperature of T = 305 ^{o}C whereas the mold was held at a temperature of T = 90 ^{o}C. For PP-LGF50 an injection temperature of T = 285 ^{o}C was chosen in coordination with the materials supplier. The diameter of the gate was D = 8.5mm at the entrance. While manufacturing of the actual part, a filling time of t = 2.1s with a maximum pressure of approximately p_{max} = 1100bar was observed.

Figure 6.22: Passenger seat component

The geometry of the component was transferred from CAD data to pre-processing using the STL interface of SIGMASOFT®. The total volume of the part with an average wall thickness of t = 2mm yielded V = 136.78 cm^3 and was represented in the finite element model by 98,370 part cells (s. fig. 6.23).
Automatic meshing was done within less than five minutes. Model size and simulation time was reduced by defining symmetric boundary conditions with respect to the xz-plane at the center gate. The mold was represented by 1,359,450 control volumes required for simulation of heat conduction, which is basically not performed in every cycle.

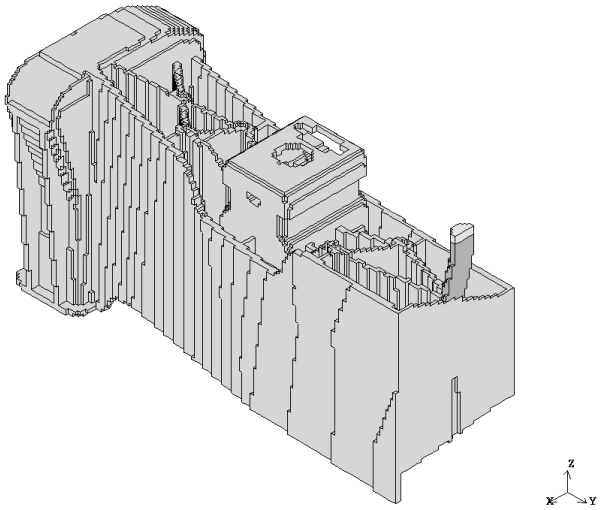

(a) STL model

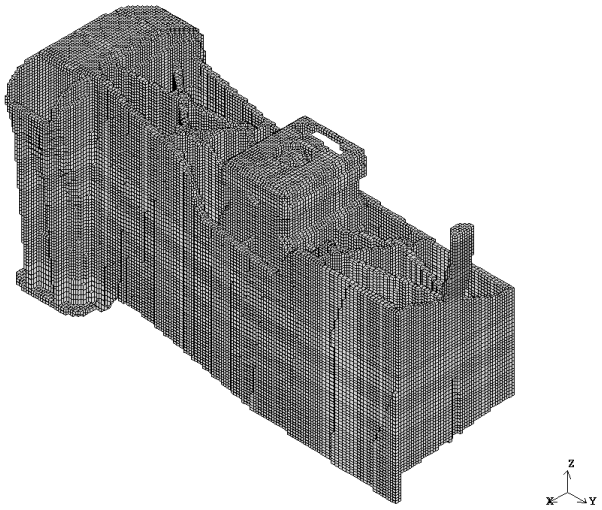

(b) Finite volume model

Figure 6.23: Model of passenger seat component, symmetry with respect to xz-plane

Although the average volume per part cell yielded 1.4mm^3, the mesh was still to coarse in order to model curved or diagonal sections of the part accurately. Either the use of different element types or increasing the number of part cells across the thickness would reduce the aliasing effect and chance of blocked fluid cells.
The fiber orientation for the passenger seat component is depicted in fig. 6.24. While a high degree of alignment was observed at the front and rear surface as well as in the diagonal ribs, a more random orientation was found in the ribs parallel to the x-direction and at the dome.

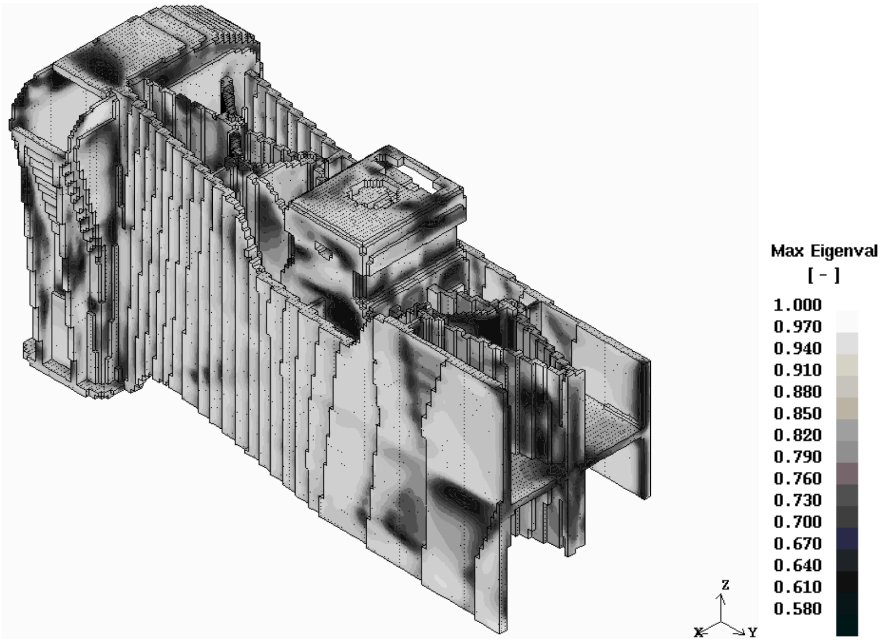

Figure 6.24: Maximum eigenvalue of fiber orientation, passenger seat component

A detailed examination in 3D simulation is provided by slicing the part in different directions, as depicted in fig. 6.25. Random orientation was found left from the dome and the dome itself (fig. 6.25(a)-(c)) and in the ribs oriented parallel to the x-direction (fig. 6.25(d)-(f)). The complex fiber orientation in the vicinity of the dome is depicted in fig. 6.26. One of the effect of three-dimensional flow is shown in fig. 6.27(c). A randomized orientation is predicted where the vertical ribs meet the horizontal mid-plane.

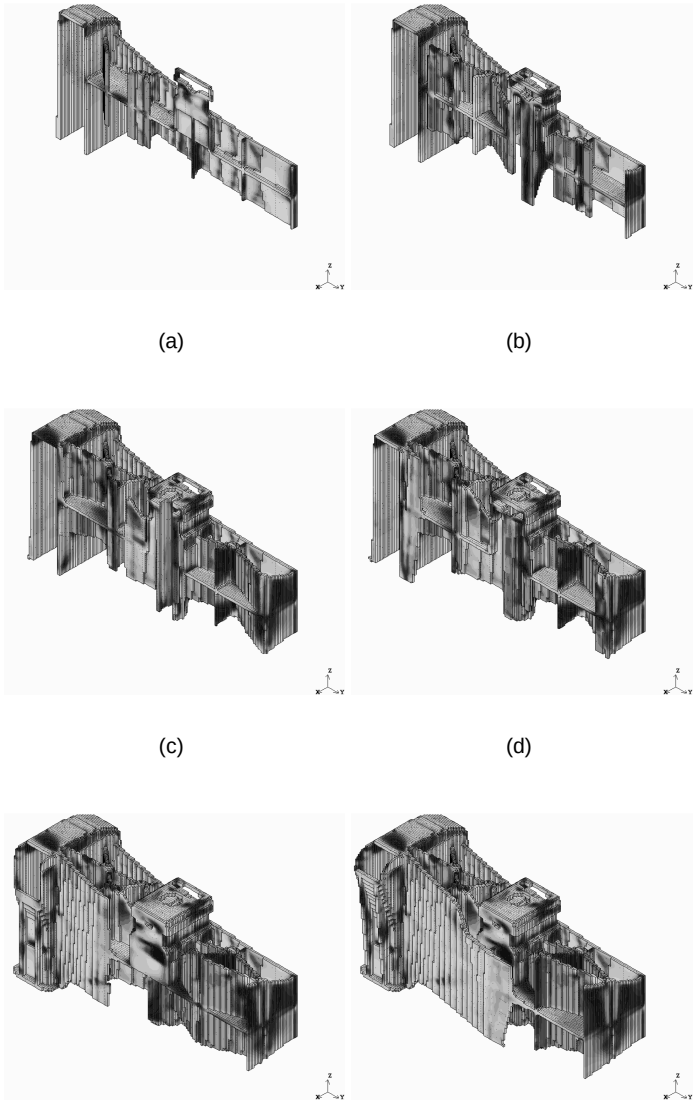

(a) (b)

(c) (d)

(e) (f)

Figure 6.25: Maximum eigenvalue of fiber orientation, passenger seat component, sections in yz-plane

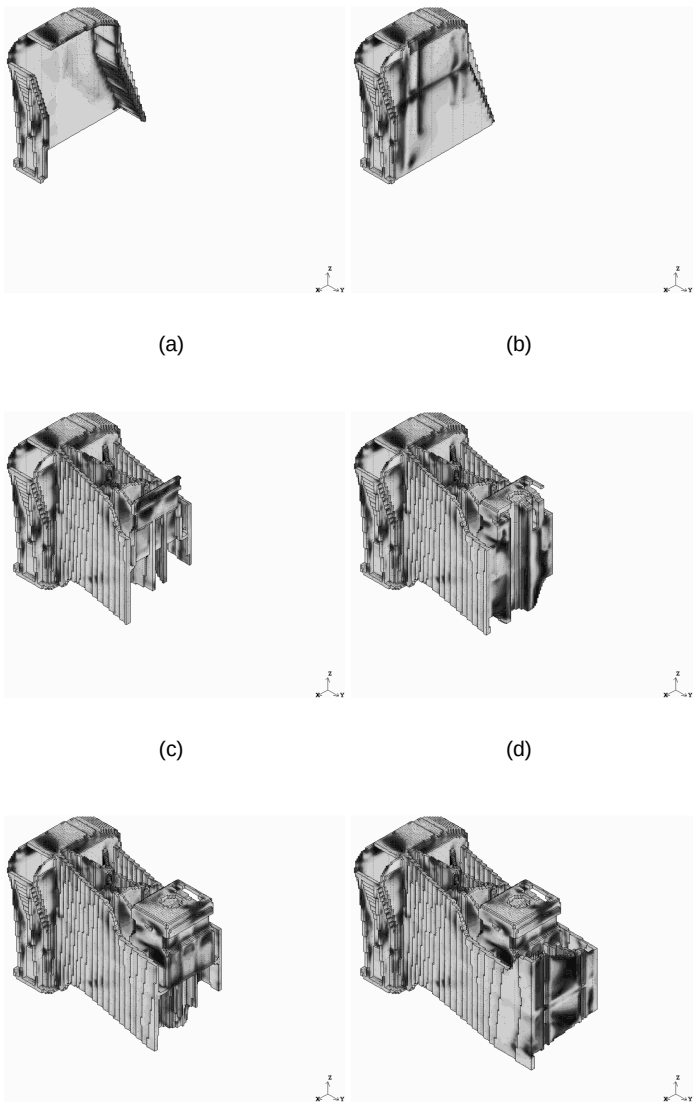

(a) (b)

(c) (d)

(e) (f)

Figure 6.26: Maximum eigenvalue of fiber orientation, passenger seat component, sections in xz-plane

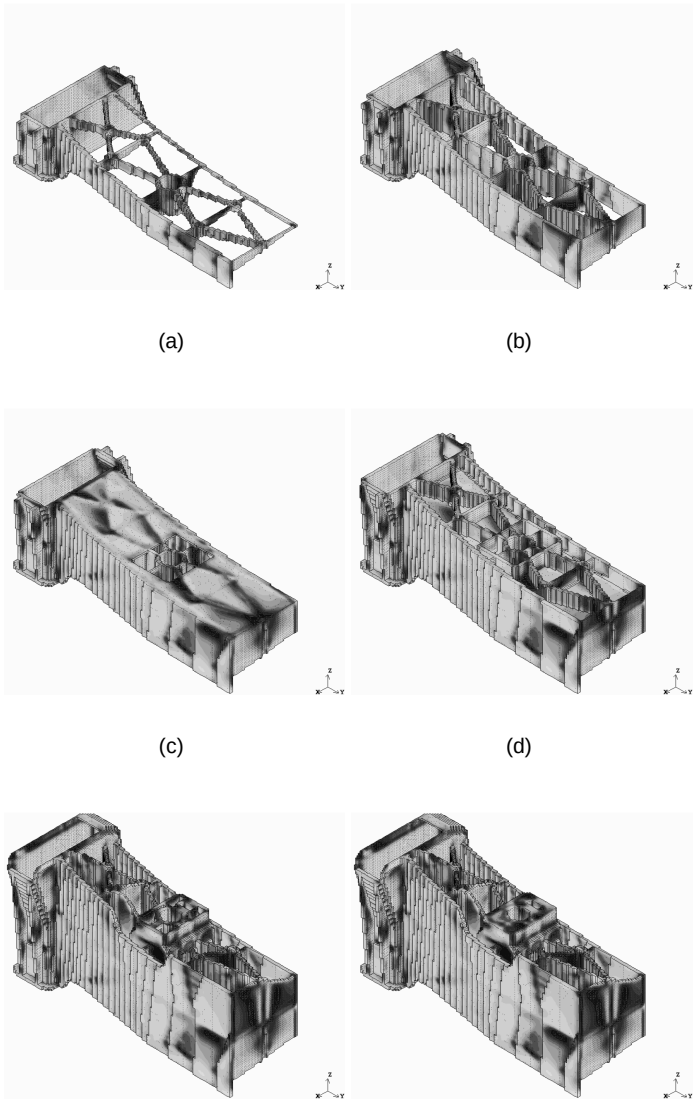

(a) (b)

(c) (d)

(e) (f)

Figure 6.27: Maximum eigenvalue of fiber orientation, passenger seat component, section in xy-plane

The simulations were carried out on a HP RISC workstation (2 CPU with 200Mhz) with 2GB RAM using a single processor. While the computational time for mold filling and fiber orientation simulation for small and mid-size models (1000 to 20000 part cells) ranged from less than one hour to four hours, the simulation time required for the passenger seat component was approximately five days. 40% of the mold was filled in less than four hours. The fiber orientation code has yet not been optimized with respect to speed.

6.4.3 Prediction of fracture toughness

Fracture toughness is one of the outstanding mechanical properties of PP-LGF. In order to verify the capability of the simulation package, the fracture toughness of PP with long glass fiber fraction of 30% and 50% has been evaluated experimentally and then compared to predictions using the microstructural efficiency concept [19, 228, 229] based on simulation of fiber orientation [230].
Square plaques (35mm x 35mm) with a height of 4mm were molded at a flow rate of Q = 30 cm^3/s and Q = 150 cm^3/s, respectively (s. fig.6.28). The melt temperature was 270^{o}C while the mold temperature yielded 40^{o}C . The fracture toughness was then derived from compact tension tests on specimens with notches parallel and transverse to the main direction of flow. The initial crack tip position was located at the center of the plaques.

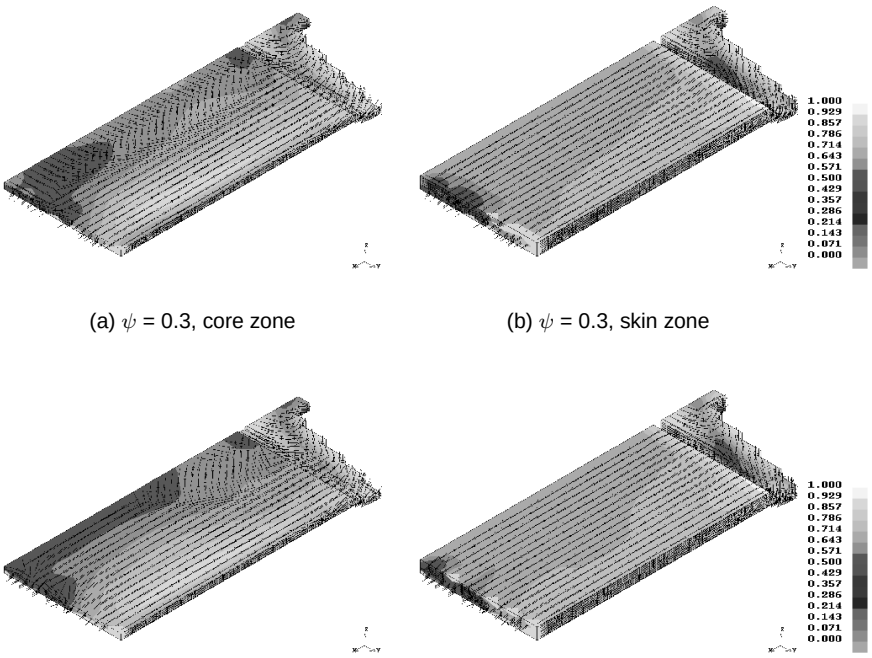

(a) ψ = 0.3, core zone (b) ψ = 0.3, skin zone

(c) ψ = 0.5, core zone (d) ψ = 0.5, skin zone

Figure 6.28: Fiber orientation degree f_p, square plaque

The fracture toughness predicted numerically yielded were moderately higher than the experimental values (s. table 6.2). The maximum deviation was derived as 14%.

		K_Q [MPa $\cdot$ m$^{\frac{1}{2}}$]	
ψ [1]	notch direction	calculated	measured
0.3	parallel	4.9	4.5
0.3	transverse	5.6	5.2
0.5	parallel	5.8	5.1
0.5	transverse	6.8	6.0

Table 6.2: Fracture resistance vs. fiber fraction and notch direction

7 Summary and Conclusion

Within the scope of this work, a rheometer has been developed that allows for measuring viscosity in situations as encountered in processing of fiber reinforced thermoplastics by injection molding with respect to the thermal and mechanical history experienced by the melt. Due to the modular design of the slit die, the cavity dimensions can quickly be altered. The combination of piezo-resistive pressure sensors and infrared sensors yields an adequate setup for measurement of pressure and temperature at elevated pressure and high rates of deformation.

However, temperature detection using infrared sensor yields weighted values of radiation emitted from different depth within the flow channel. In order to derive the penetration depth of radiation, the transmission of PP-LGF was evaluated using an infrared spectrometer. The penetration depth declined with increasing fiber fraction yielding 0.25mm for a fiber mass fraction of 50%.

During processing a significant increase in temperature of the melt prior to entering the mold and along the die was recorded. Dissipation is not as high as expected from solving the energy balance equation. However, it appears that numerical solution of momentum and energy balance equation with respect to viscosity depending on both pressure and temperature would improve the accuracy of the technique.

From pressure drop along the die, the viscosity of polypropylene reinforced by glass fibers with an initial length of 10mm, has been evaluated in both shear and extensional flow, depending on process parameters and materials composition using different cavity dimensions.

The extensional viscosity was generally found to be up to two decades higher than shear viscosity. With respect to process parameters, both shear and extensional viscosity declined with increasing temperature and rate of deformation but increase with pressure. A power-law type relationship modelling these effects on viscosity provided a good fit to experimental data in the evaluated range of parameters. While temperature had a more pronounced effect on shear viscosity, rate of deformation was observed to be the pre-dominant processing parameter for extensional viscosity.

In terms of material parameters, fiber fraction had a substantial effect on viscosity. Increasing fiber length from 10 to 12mm yielded a minor increase of viscosity. For both shear and extensional viscosity, a non-optimized sizing induced lower values for viscosity as desired for processing but not for mechanical performance.

Addressing the influence of channel dimensions on viscosity it was found, that the effect of channel height on shear viscosity was of minor importance and that good agreement between slit flow and capillary flow was obtained. In contrast, higher values for extensional viscosity were calculated with increasing channel height and decreasing contraction ratio.
Based on the rheological experiments, the coefficients of an orthotropic constitutive were derived. The coefficients were expressed in a power-law type relationship with respect to rate of deformation, melt temperature and fiber fraction.
The microstructure of injection molded specimens was quantitatively analyzed based on x-ray imaging and image processing. It was observed, that the fiber bundles generally remain intact and that good dispersion of fibers is only found in regions of high shear rates, typically the skin region. On one hand, fiber dispersion is desired with respect to mechanical performance, on the other hand, breakage in fiber bundles is reduced, leading to a higher length and also better performance. In the core region, fibers are bent and oriented transverse to the main direction of flow.
With respect to processing parameters it was observed, that fiber alignment was enhanced with increasing shear rate and decreasing temperature (i.e. higher viscosity). With increasing fiber fraction, the orientation in main flow direction is also increased due to the reduced probability of fiber-fiber interactions. Using a standard sizing of the fibers results in a fiber orientation shifted towards random when compared to an optimized fiber finish.
Analysis of the extruded strand yielded a decline of die swell with increasing shear rate, melt temperature and fiber fraction while the elastic recovery increased with quality of the fiber sizing. From theoretical considerations it was derived that average fiber length, with an initial aspect ratio of 588, was reduced with increasing fiber fraction and declining melt temperature yielding fiber aspect ratios between 60 and 135.
Correlating microstructure to the rheological properties derived from the experiments indicated that both shear and extensional viscosity are strongly related to the non-newtonian velocity profile and flow-induced fiber alignment.
In order to provide further insight into the morphology of long fiber reinforced thermoplastics, the three-dimensional microstructure of injection molded specimens was reconstructed based on x-ray imaging of 2D sections and image processing originating from computer tomography. This technique allowed for evaluation of fiber orientation, length and dispersion across an area in the range of several cm^2 with adequate resolution.

The rheological data obtained during the experiments was validated by comparing pressure and temperature data with values derived from 3D mold filling simulation using the commercial package SIGMASOFT®. The temperature profile derived from simulation slightly over-predicted the temperature rise at high shear rates while value slower than recorded were obtained at low shear rates, indicating that values measured for viscosity were too high.
Good agreement in pressure profile is observed at higher shear rates, whereas the simulation generally yields lower values at low shear rates. However, the entrance pressure drop is not captured during simulation. Hence, extensional viscosity and the effect of fiber orientation on flow become important.
For calculation of 3D fiber orientation, a module based on the orientation model proposed by Folgar and Tucker was developed at the Institute for Applied Mathematics (ITWM), Kaiserslautern. The fiber orientation, simulated and experimentally obtained was compared. It was found that for PP-LGF50 an interaction coefficient C_I = 0.01, in connection with the hybrid closure approximation, provided good agreement with experimental data. The interaction coefficient is not only a material property and has to be adjusted if melt temperature and hence viscosity is altered or fiber fraction is changed. For the fiber geometry parameter λ, a value of 0.9995, which corresponds to an aspect ratio of 63, lead to good agreement in mean fiber orientation.
3D simulation of injection molding has become very attractive due to the gain in information with respect to effects introduced by edges, ribs and thick wall sections as well as fountain flow and 3D fiber orientation. Simulation of mold filling and fiber orientation for an automotive structural component with a volume of 140cm^3 where the part geometry and mold are represented by 100,000 cells and 1.4 million solids, respectively, takes approximately 5 days.
The integration of design (CAD) and engineering (CAE) is crucial for composite structures since the interaction between design, processing and performance is very strong. 3D CAE, including process simulation and structural mechanics, will reduce the gap to CAD, where solid modelling is state-of-the art. Cost savings can be achieved by reducing the time for model generation. With rapidly increasing computational power, the additional computational effort is diminishing.

References

[1] L. D. Kramer, T. Matiacio, S. Rocca, and J. Tuschner. Improvements in injection molded thermoplastics using long fibers. In *Conference Paper EM 90-660*, Fabricating Composites, pages 1–16, Arlington, 1990. Society of Manufacturing Engineers.

[2] W. Michaeli and H. P. Thieltges. Kurz oder lang - Wirkung der Einflußfaktoren beim Spritzgießen von faserverstärkten Kunststoffen. *Maschinenmarkt*, 98(16):42–45, 1992.

[3] B. Schmid and H. G. Fritz. Schnecke ist entscheidend - Möglichkeiten zum Minimieren des Faserbruchs bei der Spritzgießverarbeitung von langfaserverstärkten Thermoplasten. *Maschinenmarkt*, 79(17):38–40, 1991.

[4] U. Bültjer. Entwicklung des europäischen Marktes für GMT/LFT. In *Weiterbilduns- und Technologie-Forum*, pages A1–A7, Würzburg, 2001. Süddeutsches Kunststoff-Zentrum.

[5] O. Becker, D. Karsono, K. Koelling, and T. Altan. Gas-assisted injection molding of long fiber reinforced thermoplastics. *J. of Materials Processing & Manufacturing Science*, 6:63–70, 1997.

[6] S.R. Gottgetreu. Injection compression molding of long fiber reinforced polypropylene. In *SAE Conference*, pages 69–76. Society of Automotive Engineers, 1998.

[7] B. Sanschagrin, M. Thierry, and B. Fisa. A study of long glass fibre orientation in reinforced injection molded parts. In *46th Annual Conference*. Composites Institute, The Society of the Plastics Industry, 1991.

[8] M. Thiery and B. Sanschagrin. A study of fiber orientation and microvoid content in long fiber reinforced injection molded parts. In *Processing Annual Technical Conference*, pages 319–325. Society of Plastics Engineers, 1991.

[9] A. Lutz and T. Harmia. Impregnation techniques for fiber bundles or tows. In J. Karger-Kocsis, editor, *Polypropylene: An A-Z Reference*, pages 301–306. Kluwer Publishers, Dordrecht, 1999.

[10] European patent application EP 0 124 003 B1, 1989.

[11] United states patent 4,812,247, 1989.

[12] F. Truckenmüller. Direktverarbeitung von Endlosfasern auf Spritzgießmaschinen. In *12. Stuttgarter Kunststoffkolloquium*, pages 1–12. IKT, IKP, Universität Stuttgart, 1991.

[13] H. Bijsterbosch and R. J. Gaymans. Polyamide 6 - long glass fiber injection moldings. *Polymer Composites*, 16(5):363–369, 1995.

[14] S. Ward and J. Crosby. The influence of microstructure on the mechanical property performance of long fiber reinforced thermoplastic composites. *Journal of Thermoplastic Composite Materials*, 3:160–169, 1990.

[15] J. Karger-Kocsis and K. Friedrich. Fracture behaviour of injection-moulded short and long glass fibre polyamide 6/6 composites. *Composite Science and Technology*, 32:293–325, 1988.

[16] J. Karger-Kocsis. Mechanical performance of short-fibre reinforced thermoplastics, application of fracture mechanics to composite materials. In K. Friedrich, editor, *Microstructure and Fracture*, pages 189–247. Elsevier Science Publishers B.V., Amsterdam, 1989.

[17] J. Karger-Kocsis. Microstructural aspects of fracture in polypropylene and in its filled chopped fiber and fiber mat reinforced composites. In J. Karger-Kocsis, editor, *Polypropylene: Structure, Blends and Composites, Part 3:Composites*, pages 142–202. Chapman and Hall, London, 1995.

[18] T. Harmia and K. Friedrich. Fracture Toughness and Failure Mechanisms of Neat and Discontinuous Long Glass Fiber Reinforced PA66/PP-Blends. *Composites Science and Technology*, 53:423–430, 1995.

[19] D.E. Spahr, K. Friedrich, J.M. Schultz, and R.S. Bailey. Microstructure and fracture behaviour of short and long fibre reinforced polypropylene composites. *Journal of Material Science*, 25:4427–4439, 1990.

[20] F. Truckenmüller and H. G. Fritz. Injection molding of long-fiber reinforced thermoplastics: A comparison of extruded and pultruded materials with direct addition of roving strands. *Polymer Engineering and Science*, 31(18):1316–1329, 1991.

[21] J. Karger-Kocsis, K. Friedrich, and R.S. Bailey. Fatigue and failure behaviour of short and long glass fiber reinforced injection-molded polypropylene. *Science and Engineering in Composite Materials*, 2:49–67, 1991.

[22] T. Harmia. Fatigue Behavior of Neat and Long Glass Fiber (LGF) Reinforced Blends of Nylon 66 and Isotactic PP. *Polymer Composites*, 17(6):926–936, 1996.

[23] H. Bogensperger. Durchblick - Erfahrungen mit Spritzgießsimulationen. *Kunststoffe*, 85(1):44–47, 1995.

[24] J.L. White. *Principles of Polymer Engineering Rheology*. John Wiley & Sons, New York, Chichester, Brisbane, Toronto, Singapore, 1990.

[25] F.N. Cogswell. *Polymer Melt Rheology*. Transactions of the Society of Rheology. John Wiley & Sons, New York, Toronto, 1981.

[26] C.W. Macosko. *Rheology: Principles, Measurements and Applications*. VCH Publishers, New York, Weinheim, Cambridge, 1994.

[27] J. P. Greene and J. O. Wilkes. Steady-state and dynamic properties of concentrated fiber-filled thermoplastics. *Polymer Engineering and Science*, 35(21):1670–1681, 1995.

[28] R. J. Crowson, M. J. Folkes, and P. F. Bright. Rheology of glass fibre-reinforced thermoplastics and its application to injection molding. I. Fiber motion and viscosity measurement. *Polymer Engineering and Science*, 20(14):925–933, 1980.

[29] R. J. Crowson, M. J. Folkes, and P. F. Bright. Rheology of glass fibre-reinforced thermoplastics and its application to injection molding. II. The effect of material parameters. *Polymer Engineering and Science*, 20(14):934–940, 1980.

[30] D.M. Binding. Capillary and contraction flow of long-(glass) fibre filled polypropylene. *Composites Manufacturing*, 2(3/4):243–252, 1991.

[31] S. E. Barbosa and J.M. Kenny. Rheology of thermoplastics matrix short glass fiber composites. In *SPE ANTEC '95*, pages 6116–6122, Boston, 1995. Society of Plastics Engineers.

[32] M.J. Folkes and A. Siddiqui. Flow of short fibre reinforced thermoplastics. *Materials World*, 5(8):448–450, 1997.

[33] A.G. Gibson and A.N. McClelland. Behaviour of long fiber reinforced polypropylene and nylon 66 in injection molding. *Mechanical Engineering*, pages 99–103, 1986.

[34] A.G. Gibson. Processing and properties of reinforced polypropylenes. In J. Karger-Kocsis, editor, *Polypropylene: Structure, Blends and Composites, Part 3:Composites*, pages 71–112. Chapman and Hall, London, 1995.

[35] G. Akay. Rheology of reinforced thermoplastics and its application to injection molding: IV. Transient injection capillary flow and injection-molding. *Polymer Engineering and Science*, 22(16):1027–1041, 1982.

[36] R. J. Crowson, M. J. Folkes, and P. F. Bright. Rheology of glass fibre-reinforced thermoplastics and its application to injection molding. III. Use of a high shear rate capillary rheometer in the injection molding shear rate range. *Polymer Engineering and Science*, 21(12):748–754, 1981.

[37] B. Schmid. *Spritzgießen von langfaserverstärktem Polyamid 6.6 unter besonderer Berücksichtigung der Faserlängenreduktion während des Formgebungsprozesses*. PhD thesis, Universität Stuttgart, 1997.

[38] S.F. Shuler, D.M. Binding, and R.B. Pipes. Rheological behavior of two- and three-phase fiber suspensions. *Polymer Composites*, 15(6):427–435, 1994.

[39] B. Souloumiac and M. Vincent. Steady shear viscosity of short fibre suspensions in thermoplastics. *Rheologica Acta*, 37:289 – 298, 1998.

[40] A. Vaxman, M. Narkis, A. Siegmann, and S. Kenig. Short-fiber-reinforced thermoplastics. Part III: Effect of fiber length on rheological properties and fiber orientation. *Polymer Composites*, 10(6):454–462, 1989.

[41] M. A. Russell. Rheological characterization of long glass fiber filled polyurethane for flow analysis programs. *Annual Technical Conference - ANTEC, Conference Proceedings*, 3:3532–3537, 1996.

[42] A. Oelgarth. *Analysis and determination of the Flow Behaviour of Long Fibre-Reinforced Moulding Compounds*. PhD thesis, RWTH Aachen, 1997.

[43] A.T. Mutel and M.R. Kamal. Rheological behavior and fiber orientation in slit flow of fiber reinforced thermoplastics. *Polymer Composites*, 12(3):136–145, 1991.

[44] D. J. Groves, M. T. Martyn, and P. D. Coates. Off line and in process converging flow measurements for polyethylene melts. *Plastics, Rubber and Composites Processing and Applications*, 26(1):13–22, 1997.

[45] A.G. Gibson. Die entry flow of reinforced polymers. *Composites*, 20(1):57–64, 1989.

[46] A. N. McClelland and A. G. Gibson. Rheology and fibre orientation in the injection molding of long fibre reinforced nylon 66 composites. *Composites Manufacturing*, 1(1):15–25, 1990.

[47] C.D. Han. *Rheology in Polymer Processing*. Academic Press, New York, San Francisco, London, 1976.

[48] R.K. Gupta and T. Sridhar. Elongational rheometers. In A.A. Collyer, editor, *Rheological Measurement*, pages 516–549. Chapman and Hall, London, 1998.

[49] H.M. Laun and H. Schuch. Elongational flow of polymer melts subsequent to extrusion. In *XIIIth International Congress on Rheology*, pages 1–55 – 1–56, Cambridge, UK, 2000.

[50] F.N. Cogswell. The rheology of polymer melts under tension. *Plastics and Polymers*, 36:109–111, 1968.

[51] H. Münstedt. Viscoelasticty of polystyrene melts in tensile creep experiments. *Rheologica Acta*, 14:1077–1088, 1975.

[52] W. Obendrauf. *Neue Methoden zur Temperatur- und Dehnviskositätsmessung für die Simulation von Kunststoffverarbeitungsprozessen*. PhD thesis, Montanuniversität Leoben, 1995.

[53] H. Münstedt. New universal extensional rheometer for polymer melts. measurements on a polystyrene sample. *Journal of Rheology*, 23(4):421–436, 1979.

[54] J. Meissner. Rheometer zur Untersuchung der deformationsmechanischen Eigenschaften von Kunststoff-Schmelzen unter definierter Zugbeanspruchung. *Rheologica Acta*, 8:78–88, 1969.

[55] J. Meissner. Development of a universal extensional rheometer for the uniaxial extension of polymer melts. *Transactions of the Society of Rheology*, 16(3):405–420, 1972.

[56] J. Meissner and J. Hostettler. A new elongational rheometer for polymer melts and other highly viscoelastic liquids. *Rheologica Acta*, 33:1–21, 1994.

[57] A. Tripathi, P. Whittingstall, and G.H. Mc Kinley. Using filament stretching rheometry to predict strand formation and 'processability' in adhesives and other non-newtonian fluids. *Rheologica Acta*, 39:321–337, 2000.

[58] M.H. Wagner, H. Bastian, P. Hachmann, J. Meissner, S. Kurzbeck, H. Münstedt, and F. Langouche. The strain-hardening behaviour of linear and long-chain-branched polyolefin melts in extensional flows. *Rheologica Acta*, 39(2):97–109, 2000.

[59] G. Lin and M. Hu. Measurement of elongation viscosity for polymer melts by fiber spinning. *Advances in Polymer Technology*, 16(3):199–207, 1997.

[60] A.G. Gibson. Converging dies. In A.A. Collyer, editor, *Rheological Measurement*, pages 455 – 491. Chapman and Hall, London, 1998.

[61] A.G. Gibson and S. Toll. Mechanics of the squeeze flow of planar fibre suspensions. *Journal of Non-Newtonian Fluid Mechanics*, 82:1 – 24, 1999.

[62] M. Kompani and D.C. Venerus. Equibiaxial extensional flow of polymer melts via lubricated squeezing flow. I. Experimental analysis. *Rheologica Acta*, 39:444–451, 2000.

[63] D.C. Venerus, M. Kompani, and B. Bernstein. Equibiaxial extensional flow of polymer melts via lubricated squeezing flow. II. Flow modeling. *Rheologica Acta*, 39:574–582, 2000.

[64] W. Obendrauf, W. Peinhopf, B. Mlekusch, and G.R. Langecker. Dehneffekte berücksichtigen - eine einfache Möglichkeit zur Berücksichtigung von Dehneffekten in Simulationsprogrammen. *Kunststoffe*, 87(11):1676–1679, 1997.

[65] D. Rajagopalan. Computational analysis of techniques to determine extensional viscosity from entrance flows. *Rheologica Acta*, 39(2):138–151, 2000.

[66] A.B. Metzner and A.P. Metzner. *Rheologica Acta*, 9:174, 1970.

[67] F.N. Cogswell. Converging flows of polymer melts in extrusion dies. *Polymer Engineering and Science*, 12(1):64 –73, 1972.

[68] F.N. Cogswell. Measuring the extensional rheology of polymer melts. *Transactions of the Society of Rheology*, 16(3):383 – 403, 1972.

[69] C. Kwag and J. Vlachopoulos. An assessment of Cogswell's method of measurement of extensional viscosity. *Polymer Engineering and Science*, 31(14):1015 – 1021, 1991.

[70] B.H. Bersted. Refinement of the converging flow method of measuring extensional viscosity in polymers. *Polymer Engineering and Science*, 33(16):1079 – 1083, 1993.

[71] S.A. McGlashan and M.E. Mackay. Comparison of entry flow techniques for measuring elongation flow properties. *Journal of Non-Newtonian Fluid Mechanics*, 85:213 – 227, 1999.

[72] P. Revenu, J. Guillet, C. Carrot, and A. Arsac. Validation of Cogswell's convergent flow analysis. *Journal of Applied Polymer Science*, 62:1783–1792, 1996.

[73] D. M. Binding. An approximate analysis for contraction and converging flows. *Journal of Non-Newtonian Fluid Mechanics*, 27:173–189, 1988.

[74] D. M. Binding and K. Walters. On the use of flow through a contraction in estimating the extensional viscosity of mobile polymer solutions. *Journal of Non-Newtonian Fluid Mechanics*, 30:233–250, 1988.

[75] H.M. Laun and H. Schuch. Transient elongational viscosities and drawability of polymer melts. *Journal of Rheology*, 33(1):119–175, 1989.

[76] A. D. Gotsis and A. Odriozola. The relevance of entry flow measurements for the estimation of extensional viscosity of polymer melts. *Rheologica Acta*, 37(5):430–437, 1998.

[77] M. Rides and C.R.G. Allen. Evaluation and comparison of the predictions of various converging flow models for determining extensional viscosity data for polymer melts. In *XIIIth International Congress on Rheology*, pages 3–16 – 3–18, Cambridge, UK, 2000.

[78] R.N. Shroff, L.V. Canci, and M. Shida. Extensional flow of polymer melts. *Trans Soc Rheol*, 21(3):429–446, 1977.

[79] M. Padmanabhan and C.W. Macosko. Extensional viscosity from entrance pressure drop measurements. *Rheologica Acta*, 36(2):144 – 151, 1997.

[80] R. Müller and D. Frölich. New extensional rheometer for elongational viscosity and flow birefringence measurements: Some results on polystyrene melts. *Polymer*, 26(10):1477–1488, 1985.

[81] H.M. Laun. Polymer melt rheology with a slit die. *Rheologica Acta*, 22:171 – 185, 1983.

[82] G.K. Batchelor. The stress system in a suspension of force-free particles. *Journal of Fluid Mechanics*, 41(3):545 – 570, 1970.

[83] G.K. Batchelor. The stress generated in a non-dilute suspensions of elongated particles by pure straining motion. *Journal of Fluid Mechanics*, 46(4):813 – 829, 1971.

[84] J. Mewis and A.B. Metzner. The rheological properties of suspensions of fibres in newtonian fluids subjected to extensional deformation. *Journal of Fluid Mechanics*, 62(3):593 – 600, 1974.

[85] E.S.G. Shaqfeh and G.H. Fredrickson. The hydrodynamic stress in a suspension of rods. *Physics of fluids A*, 2(5):7 – 24, 1990.

[86] R.B. Pipes, J.W.S. Hearle, A.J. Beaussart, A.M Sastry, and R.K. Okine. A constitutive relation for the viscous flow of an oriented fiber assembly. *Journal of Composite Materials*, 25:1204–1217, 1991.

[87] R.B. Pipes, D.W. Coffin, S.F. Shuler, and P. Simacek. Non-newtonian constitutive relationships for hyperconcentrated fiber suspensions. *Journal of Composite Materials*, 28(4):343–351, 1994.

[88] J.D. Goddard. An elastohydrodynamic theory for the rheology of concentrated suspensions of deformable particles. *Journal of Non-Newtonian Fluid Mechanics*, 2:169 – 189, 1977.

[89] D.W. Coffin and R.B. Pipes. Constitutive relations for aligned discontinuous fiber composites. *Journal of Composite Manufacturing*, 2(3/4):141–146, 1991.

[90] S. Toll and P. O. Andersson. Microstructure of long- and short-fiber reinforced injection moulded polyamide. *Polymer Composites*, 14(2):116–125, 1993.

[91] P. H. Foss, L. P. Inzinna, C. M. Dunbar, and C. L. Tucker III. Prediction of fiber orientation and mechanical properties using C-mold and ABAQUS. In *Processing Annual Technical Conference*. Society of Plastics Engineers, 1996.

[92] C. Hauck and G. Brouwers. Faserverstärkte Spritzguß-Bauteile optimal auslegen. *Kunststoffe*, 82(7):586–590, 1992.

[93] T.P. Skourlis, C. Chassapis, and S. Mannoochehri. Fiber orientation morphological layers in injection molded long fiber reinforced thermoplastics. *Journal of Thermoplastic Composite Materials*, 10:453–475, 1997.

[94] M. Metten and M. Cremer. Langfaserverstärkte Thermoplaste spritzgiessen. *Kunststoffe*, 90(1):80–83, 2000.

[95] S. Ranganathan and S.G. Advani. Characterization of orientation clustering in short-fiber composites. *Journal of Polymer Science, Part B: Polymer Physics*, 28:2651–2672, 1990.

[96] D. M. Scott. Nondestructive analysis of fiber dispersion and loading. *Composites Part A*, 18A:703–707, 1997.

[97] J.S. Cheon, S.Y. Kim, and Y.T. Im. Determination of short glass-fiber volume fractions in compression molded thermoset composites - experimental. *Journal of Composite Materials*, 1997.

[98] Y. T. Zhu, W. R. Blumenthal, and T. C. Lowe. Determination of nonsymmetric 3-d fiber-orientation distribution and average fiber length in short-fiber composites. *Journal of Composite Materials*, 31(13):1287–1301, 1997.

[99] J.S. Cheon, S.Y. Kim, and Y.T. Im. Determination of short glass-fiber volume fractions in compression molded thermoset composites - numerical. *Journal of Composite Materials*, 1997.

[100] Z. Fang and N. Phan-Thien. Particle suspension model: An unstructured finite-volume implementation. *Journal of Non-Newtonian Fluid Mechanics*, 80(2-3):135–153, 1999.

[101] M.G. Bertoluzzo, S.M. Bertoluzzo, J.A. Luisetti, and C.A. Gatti. A bidimensional simulation fo particle-cluster aggregation with variable active sites particles. *Colloid Polymer Science*, 276:443 – 445, 1998.

[102] S. Ranganathan and S.G. Advani. Fiber-fiber and fiber-wall interactions during the flow of non-dilute suspensions. In T. D. Papathanasiou and D. C. Guell, editors, *Flow-Induced Alignment in Composite Materials*. Technomic, Lancaster, 1997.

[103] M. B. Mackaplow and E. S. G. Shaqfeh. Numerical study of the sedimentation of fibre suspensions. *Journal of Fluid Mechanics*, 376:149, 1998.

[104] M. Vincent, E. Devilers, and J. F. Agassant. Fibre orientation calculation in injection moulding of reinforced thermoplastics. *J. Non-Newt. Fluid Mech.*, 73(3):317, 1997.

[105] J. Azaiez, R. Guenette, and A. Ait-Kadi. Investigation of the abrupt contraction flow of fiber suspensions in polymeric fluids. *Journal of Non-Newtonian Fluid Mechanics*, 73(3):289–316, 1997.

[106] A. Ramazani, A. Ait-Kadi, and M. Grmela. Rheological modelling of short fiber thermoplastic composites. *Journal of Non-Newtonian Fluid Mechanics*, 73(3):241–260, 1997.

[107] R. R. Sundararajakumar and D. L. Koch. Structure and properties of sheared fiber suspensions with mechanical contacts. *Journal of Non-Newtonian Fluid Mechanics*, 73(3):205, 1997.

[108] K. A. Ericsson, S. Toll, and J. A. E. Manson. The two-way interaction between anisotropic flow and fiber orientation in squeeze flow. *Journal of Rheology*, 41(3):491–511, 1997.

[109] R. Shanker, Jr. Gillespie, J. W., and S. I. Guceri. Numerical simulation of hydrodynamic interactions in fiber suspensions. *American Society of Mechanical Engineers, Applied Mechanics Division*, 175:165–175, 1993.

[110] S. E. Barbosa, D. R. Ercoli, M. A. Bibbo, and J. M. Kenny. Rheology of short-fiber composites: A systematic approach. *Composite Structures*, 27(1-2):83, 1994.

[111] K. K. Kabanemi, J. F. Hetu, and A. Garcia-Rejon. 3-d coupled solution for the flow and fiber orientation in injection molding of fiber-filled systems. *American Society of Mechanical Engineers, Applied Mechanics Division*, 217:207, 1996.

[112] M. B. Mackaplow and E. S. G. Shaqfeh. Numerical study of the rheological properties of suspensions of rigid, non-brownian fibres. *Journal of Fluid Mechanics*, 329:155, 1996.

[113] S. Ranganathan and S. G. Advani. Simultaneous solution for flow and fiber orientation in axisymmetric diverging radial flow. *Journal of Non-Newtonian Fluid Mechanics*, 47:107, 1993.

[114] S. Yamamoto and T. Matsuoka. Dynamic simulation of microstructure and rheology of fiber suspensions. *Polymer Engineering and Science*, 36(19):2396–2403, 1996.

[115] S. J. Lee and S. J. Lee. Numerical simulation of extrudate swell of semi-concentrated fiber suspensions. *American Society of Mechanical Engineers, Applied Mechanics Division*, 153:87, 1992.

[116] Y. Iso, D. L. Koch, and C. Claude. Orientation in simple shear flow of semi-dilute fiber suspensions. 1. Weakly elastic fluids. *Journal of Non-Newtonian Fluid Mechanics*, 62(2-3):115, 1996.

[117] C. L. Tucker. Flow regimes for fiber suspensions in narrow gaps. *Journal of Non-Newtonian Fluid Mechanics*, 39:239–268, 1991.

[118] S. Ranganathan and S. G. Advani. Characterization of orientation clustering in short-fiber composites. *Journal of Polymer Science, Part B: Polymer Physics*, 28(13):2651, 1990.

[119] M. Rahnama, D. L. Koch, and E. S. G. Shaqfeh. Effect of hydrodynamic interactions on the orientation distribution in a fiber suspension subject to simple shear flow. *Physics of Fluids*, 7(3):487, 1995.

[120] X. Fan, N. Phan-Thien, and R. Zheng. Direct simulation of fibre suspensions. *Journal of Non-Newtonian Fluid Mechanics*, 74(1-3):113–135, 1998.

[121] N. Phan-Thien, Z. Fang, and A. L. Graham. Stability of some shear flows for concentrated suspensions. *Rheologica Acta*, 35(1):69, 1996.

[122] C. G. Caro, T. J. Pedley, R. C. Schroter, and W. A. Seed. *The mechanics of the circulation*. Oxford University Press, 1978.

[123] H. L. Goldsmith. Red cell motions and wall interactions in tube flow. *Fed. Proc. Fedn. Am. Socs. Exp. Biol.*, 30:1578, 1971.

[124] H. L. Goldsmith. The flow of model particles and blood cells and its relation to thrombogenesis. In *Progress in Hemostasis and Thrombosis*. Gune and Stratton, Inc., 1972.

[125] J. Happel and H. Brenner. *Low Reynolds number hydrodynamics*. Prentice-Hall, Inc., 1965.

[126] M. M. El-Refaee and R. M. El-Taher. Viscous shear flow over a circular cylinder - numerical study. *International Journal of Engineering Science*, 23(12):1305, 1985.

[127] A. J. Goldman, R. G. Cox, and H. Brenner. Slow viscous motion of a sphere parallel to a plane wall - II. Couette flow. *Chemical Engineering Science*, 22:653, 1967.

[128] C. L. Tucker III. and S. G. Advani. Processing of short fiber systems. In S. G. Advani, editor, *Flow and Rheology in Polymer Composites Manufacturing*, pages 257 – 324. Elsevier, 1994.

[129] T. A. Osswald and S. C. Tseng. Compression molding. In S. G. Advani, editor, *Flow and Rheology in Polymer Composites Manufacturing*, pages 361 – 414. Elsevier, 1994.

[130] M. J. Crochet, F. Dupret, and V. Verleye. Injection molding. In S. G. Advani, editor, *Flow and Rheology in Polymer Composites Manufacturing*, pages 415 – 464. Elsevier, 1994.

[131] G. Jeffery. The motion of ellipsoidal particles immersed in a viscous fluid. *Proceedings of the Royal Society of London, Series A*, 102:161–179, 1923.

[132] G.F. Modlen. Re-orientation of fibres during mechanical working. *Journal of Materials Science*, 4:283–289, 1969.

[133] S. Dinh and R. Armstrong. A rheological equation of state for semi-concentrated fiber suspensions. *Journal of Rheology*, 28(3):207–227, 1984.

[134] K. von Diest. *Prozeßsimulation und Faserorientierungserkennung von GMT-Bauteilen*. PhD thesis, Universität Kaiserslautern, 1995.

[135] K. von Diest. Experimental evaluation and numerical simulation of fiber orientation in GMT. In *ICCM-10*, 1995.

[136] H. L. Goldsmith and S. G. Mason. The micro-rheology of dispersions. In F. R. Eirich, editor, *Rheology: Theory and Applications*, pages 85–250, 1967.

[137] B. J. Trevelyan and S. G. Mason. Particle motions in sheared suspensions - I. Rotations. *Journal of Colloid Science*, 6:354, 1951.

[138] E. Anczurowski, R. G. Cox, and S. G. Mason. The kinetics of flowing dispersions - IV. Transient orientations of cylinders. *Journal Colloid and Interface Science*, 23:547, 1967.

[139] A. Okagawa, R. G. Cox, and S. G. Mason. The kinetics of flowing dispersions - XII. Some effects of non uniform shear. *Journal Colloid and Interface Science*, 71(1):11, 1979.

[140] F. P. Folgar. Fiber orientation distribution in concentrated suspensions: a predictive model. Phd thesis, University of Illinois at Urbana-Champaign, 1983.

[141] C. A. Stover. The dynamics of fibers suspended in shear flows. Ph.D. thesis, Cornell University, 1991.

[142] S. Ranganathan and S. G. Advani. Fiber-fiber interactions in homogeneous flows of non-dilute suspensions. *Journal of Rheology*, 35:1499, 1991.

[143] S. Ranganathan. Mechanics of fiber-fiber interactions during the flow of non-dilute short fiber suspensions. PhD thesis, University of Delaware, 1993.

[144] R. G. Cox. The motion of suspended particles almost in contact. *International Journal of Multiphase Flow*, 1:343, 1974.

[145] E. P. Ascoli, D. S. Dandy, and L. G. Leal. Low Reynolds number hydrodynamic interaction of a solid particle with a planar wall. *International Journal of Numerical Methods in Fluids*, 9:651, 1989.

[146] H. Brenner. The slow motion of a sphere through a viscous liquid toward a plane surface. *Chem. Eng. Sci.*, 16:242, 1961.

[147] M.P. Petrich and D.L. Koch. Interactions between contacting fibers. *Physics of fluids Fluids*, 10(8):2111–2113, 1998.

[148] J. Thomasset, M. Grmela, and P. J. Carreau. Microstructure and rheology of polymer melts reinforced by long glass fibres: Direct simulations. *Journal of Non-Newtonian Fluid Mechanics*, 73(3):195–203, 1997.

[149] P. Skjetne, R.F. Ross, and D.J. Klingenberg. Simulation of single fiber dynamics. *Journal of Chemical Physics*, 107(6):2108–2121, 1997.

[150] A. Falade and H. Brenner. First-order wall curvature effects upon the Stokes' resistance of a spherical particle moving in close proximity to a solid wall. *Journal of Fluid Mechanics*, 193:533, 1988.

[151] S. Wakiya. Viscous flows past a spheroid. *Journal of the Physical Society of Japan*, 12(10):1130, 1957.

[152] S. M. Yang and L. G. Leal. Particle motion in Stokes' flow near a plane fluid-fluid interface - I. Slender body in a quiescent fluid. *Journal of Fluid Mechanics*, 136:393, 1983.

[153] S. M. Yang and L. G. Leal. Particle motion in Stokes' flow near a plane fluid-fluid interface - II. Linear shear and axisymmetric straining flows. *Journal of Fluid Mechanics*, 149:275, 1984.

[154] C. Chan. Hydrodynamic interactions in large aspect ratio fiber suspensions. Ph.D. thesis, University of Delaware, 1991.

[155] M. W. Darlington and P. L. McGinley. Fiber orientation in short fiber reinforced plastics. *Journal of Material Science*, 10:906, 1975.

[156] P. Singh and M. R. Kamal. The effect of processing variables on microstructure of injection molded short fiber reinforced polyproylene composites. *Polymer Composites*, 10(5):344, 1989.

[157] G. Lipscomb and M. Denn. The flow in fiber suspensions in complex geometries. *Journal of Non-Newtonian Fluid Mechanics*, 26:297–325, 1988.

[158] S. T. Chung and T. H. Kwon. Coupled analysis of injection molding filling and fiber orientation, including in-plane velocity gradient effect. *Polymer Composites*, 17(6):859–872, 1996.

[159] B.E. VerWeyst. *Numerical Predictions of Flow-Induced Fiber Orientation in Three-Dimensional Geometries*. PhD thesis, University of Illinois, Urbana-Champaign, 1998.

[160] C. Friedl. Progress towards true 3D CAE analysis for injection molding. In *Processing Annual Technical Conference*, volume 1, pages 731–735. Society of Plastics Engineers, 1996.

[161] V. Rajupalem, K. Talwar, and C. Friedl. Three-dimensional simulation of the injection molding process. In *Processing Annual Technical Conference*, pages 670–673. Society of Plastics Engineers, 1997.

[162] S. G. Advani and C. L. Tucker III. A numerical simulation of short fiber orientation in compression molding. *Polymer Composites*, 11(3):164–173, 1990.

[163] W. Michaeli and M. Heber. Calculation of fibre orientation for complex SMC parts. In *Processing Annual Technical Conference*, pages 1794–1797. Society of Plastics Engineers, 1994.

[164] M. Saitoh, T. Nakagawa, S. Kukula, and O. Ohtani. Development of numerical analysis software applied to products with discontinuous fibers. *Kobelco Technology Review*, 19:52–56, 1996.

[165] O. Altmann and H. J. Wirth. 3D-CAE-Rheologie über 3D-CAD-Volumenmodelle. *Kunststoffe*, 87(11):1670–1675, 1997.

[166] K. K. Kabanemi, J. F. Hetu, and A. Garcia-Rejon. Numerical simulation of the flow and fiber orientation in reinforced thermoplastics injection molded products. *International Journal of Polymer Processing*, 12(2):182–191, 1997.

[167] G.A.A.V Haagh, H. Zuidema, F.N. van de Vosse, G.W.M Peters, and H.E.H. Meijer. Towards a 3-D finite element model for the gas-assisted injection moulding process. *International Journal of Polymer Processing*, 3:207–215, 1997.

[168] A. Reinhardt, M. Maier, H. Schüle, and S.G. Advani. Rheological characterization of long glass fibre reinforced polypropylene. In *XIIIth International Congress on Rheology*, pages 4–47 – 4–49, Cambridge, UK, 2000.

[169] R.W. Whorlow. *Rheological Techniques*. John Wiley & Sons, New York, Chichester, Brisbane, Toronto, 1980.

[170] W. Obendrauf and G.R. Langecker. Temperature measuring in plastics processing with infrared radiation thermometers. *International polymer processing*, 13(1):71–77, 1998.

[171] W. Obendrauf, C. Kukla, and G.R. Langecker. Schnelle Temperaturmessung mit IR-Fühlern. *Kunststoffe*, 83(12):971–974, 1993.

[172] C.D. Han. Slit rheometry. In A.A. Collyer and D.W. Clegg, editors, *Rheological Measurement*, pages 190 – 209. Chapman and Hall, London, Weinheim, New York, Tokyo, Melbourne, Madras, 2nd edition, 1998.

[173] E. Mitsoulis, S. G. Hatzikiriakos, K. Christodoulou, and D. Vlassopoulos. Sensitivity analysis of the bagley correction to shear and extensional rheology. *Rheologica Acta*, 37(5):438–448, 1998.

[174] V. G. Geethamma, K. Ramamurthy, R. Janardhan, and Sabu Thomas. Melt flow behavior of short coir fiber reinforced natural rubber composites. *International Journal of Polymeric Materials*, 32(1-4):147–161, 1996.

[175] D. Roy and B. R. Gupta. Rheological behavior of short carbon fiber-filled thermoplastic elastomer based on styrene-isoprene-styrene block copolymer. *Journal of Applied Polymer Science*, 49(8):1475–1482, 1993.

[176] H.C. Tseng, G.E. Grant, C.A. Hieber, K.K. Wang, and H.H. Chiang. Analysis of rheological data from an automated-injection-molding capillary rheometer. In *Annual Technical Conference SPE ANTEC '85*, pages 716–, Indianapolis, 1985. Society of Plastics Engineers.

[177] R.E. Carter. On the measurement of the pressure coefficient of viscosity by capillary extrusion rheometry, and on the relevance of this parameter to practical materials processing. In *XIIIth International Congress on Rheology*, pages 3–125 – 3–127, Cambridge, UK, 2000.

[178] D. M. Binding, M. A. Couch, and K. Walters. Pressure dependence of the shear and elongational properties of polymer melts. *Journal of Non-Newtonian Fluid Mechanics*, 79(2-3):137–155, 1998.

[179] H. Hamada, K. Fujihara, and A Harada. The influence of sizing conditions on bending properties of continuous glass fiber reinforced polypropylene composites. *Composites*, Part A(31):979–990, 2000.

[180] P.R. Schunk and L.E. Scriven. Constitutive equation for modeling mixed extension and shear in polymer solution procesing. *Journal of Rheology*, 34(7):1085–1119, 1990.

[181] J. Thomasset, B. Sanschagrin, and P.J. Carreau. Rheological properties of long glass fiber reinforced polyproplene. In *Proc. 10th Annual Meeting PPS*, pages 417–418, Akron, 1994.

[182] A.N.R. McClelland. *The Injecton Moulding of Long Glass Fibre Reinforced Thermoplastic Materials*. Phd thesis, University of Liverpool, 1988.

[183] R.C. Warren. Viscous heating. In A.A. Collyer, editor, *Rheological Measurement*, pages 210 – 236. Chapman and Hall, London, 1998.

[184] J.F.T. Pittman and R. Sander. Thermal effects in extrusion: Slit dies. *Intern. Polymer Processing*, IX(4):326 – 345, 1994.

[185] J. Radon. über die Bestimmung von Funktionen durch ihre Integralwerte längs gewisser Mannigfaltigkeiten. *Berichte der Sächsischen Akademie der Wissenschaften*, 69:262–277, 1917.

[186] A.M. Cormack. Representation of a function by its line integrals, with some radiological applications. *Journal of Applied Physics*, 34:2722–2733, 1963.

[187] G. Hounsfield. Computerized transverse axial scanning (tomography): Part 1. Description of system. *British Journal of Radiology*, 46:1016–1022, 1973.

[188] S. Fakirov and C. Fakirova. Direct determination of the orientation of short glass fibres in an injection moulded polyethylene terephthalate system. *Polymer Composites*, 6(1):41–46, 1985.

[189] S.W. Yurgartis. Measurement of small angle fibre misalignments in continuous fibre composites. *Composites Science and Technology*, 30:279–293, 1987.

[190] G. Fischer and P. Eyerer. Measuring spatial orientation of short fibre reinforced thermoplastics using image analysis. *Polymer Composites*, 9(4):297–304, 1988.

[191] S. Toll and P.O. Andersson. Microstructural characterisation of injection moulded composites using image analysis. *Composites*, 22(4):298–306, 1991.

[192] P.J. Hine, R.A. Duckett, N.C. Davidson, and A.R. Clarke. Modelling of the elastic properties of fibre reinforced composites. I. Orientation measurement. *Composites Science and Technology*, 47:65–73, 1993.

[193] J.J. McGrath and J.M. Wille. Determination of 3D fiber orientation distributions in thermoplastic injection molding. *Composites Science and Technology*, 53:133–143, 1995.

[194] B. Lian, J. Ladewig, J.M. Wille, and J.J. McGrath. Three-dimensional fiber orientation distributions in injection-molded, short fiber-reinforced thermoplastics. In *Processing Annual Technical Conference*, pages 2316–2320. Society of Plastics Engineers, 1994.

[195] A.R. Clarke, N.C. Davidson, and G. Archenhold. Mesostrutural characterisation of aligned fibre composites. In T. D. Papathanasiou and D. C. Guell, editors, *Flow-Induced Alignment in Composite Materials*. Technomic, Lancaster, 1997.

[196] A.R. Clarke, G. Archenhold, and N.C. Davidson. A novel technique for determining the 3D spatial distribution of glass fibres in polymer composites. *Composites Science and Technology*, 55:75–91, 1995.

[197] J.P. Dunkers, R.S. Parnas, C.G. Zimba, R.C. Peterson, K.M. Flynn, J.G. Fujimoto, and B.E. Bouma. Optical coherence tomography of glass reinforced polymer composites. *Composites: Part A*, 30:139–145, 1999.

[198] G. Bechtold. *Pultrusion von geflochtenen und axial verstärkten Thermoplast-Halbzeugen und deren zerstörungsfreie Porengehaltsbestimmung*. PhD thesis, Universität Kaiserslautern, 2000.

[199] K. von Diest, A. Meij, M. Maier, and M. Neitzel. Neue Erkenntnisse zur Faserorientierung von GMT. In *AVK-Tagung*, pages B9.1–B9.9, Berlin, 1994.

[200] W. Michaeli and M. Heber. Easy and quick method for the measurement of fibre orientation. In *Processing Annual Technical Conference*, pages 1790–1793. Society of Plastics Engineers, 1994.

[201] J. Bonse. Röntgen-Mikrotomographie. *Phys.Bl.*, 53(33):211–214, 1997.

[202] U. Huber and M. Maier. Optische Bestimmung der Faserorientierung in Verbundwerkstoffen. *Nachrichten aus Chemie, Technik und Laboratorium, Supplement*, 45:134 – 136, 1997.

[203] T. Harmia. *Aufbau, mechanische Eigenschaften und Bruchverhalten von unverstärkten, kurzfaser- und diskontinuierlich langfaserverstärkten Polymeren und Blends*. PhD thesis, Universität Kaiserslautern, Kaiserslautern, 1996.

[204] N.N. Bestimmung von Faserorientierungsstrukturen an diskontinuierlich fasergefüllten Thermoplasten durch Rekonstruktion dreidimensionaler Sachverhalte aus räumlichen Bildfolgen zweidimensionaler Schnitte und/oder Schliffe. Technical Report 310D, AiF, 1993.

[205] N.N. Bildanalytische Rekonstruktion dreidimensionaler Füllstoffstrukturen. Technical Report 1083B, AiF, 1999.

[206] R. Shanker, Jr. J. W. Gillespie, and S. I. Guceri. Flow-induced fiber orientation in nonhomogeneous flow fields. *American Society of Mechanical Engineers, Applied Mechanics Division*, pages 71–79, 1989.

[207] J. Linn, J. Steinbach, and A. Reinhardt. Calculation of the 3d fiber orientation in the simulation of the injection molding process for short fiber reinforced thermoplastics. In *11th ECMI Conference*, Palermo, 2000. European Consortium for Mathematics in Industry.

[208] S. G. Advani and C. L. Tucker. The use of tensors to describe and predict fiber orientation in short fiber composites. *Journal of Rheology*, 31(8):751–784, 1987.

[209] E. J. Hinch. The distortion of a flexible inextensible thread in a shearing flow. *Journal of Fluid Mechanics*, 74(2):317–333, 1976.

[210] F. Folgar and C. L. Tucker. Orientation behavior of fibers in concentrated suspensions. *Journal of Reinforced Plastics and Composites*, 3:98–119, 1984.

[211] M.R. Kamal and A.T. Mutel. The prediction of flow and orientation behavior of short fiber reinforced melts in simple flow systems. *Polymer Composites*, 10:337–343, 1989.

[212] B. E. VerWeyst and C. L. Tucker III. The optimized quasi-planar approximation for predicting fiber orientation in injection-molded composites. *Intern. Polymer Processing*, XII(3):238–248, 1997.

[213] S. Ranganathan and S. G. Advani. On modeling fiber-fiber interactions of flowing suspensions in homogeneous flows. *Journal of Rheology*, 35:1499–1522, 1991.

[214] R.S. Bay and C.L. Tucker III. Fiber orientation in simple injection moldings. part I: Theory and numerical methods. *Polymer Composites*, 13(4):317–331, 1992.

[215] S. G. Advani. Molding short fiber composites: Flow processing. In S. Lee, editor, *International Encyclopedia of Composites*, volume III, pages 514–526. VCH Publishers, 1990.

[216] J. S. Cintra and C. L. Tucker. Orthotropic closure approximations for flow-induced fiber orientation. *Journal of Rheology*, 39(6):1095–1122, 1995.

[217] F. Dupret, V Verleye, and B. Languilier. Numerical prediction of the moulding of short fibre composite parts. In *1st ESAFORM Conference*, pages 291–294, 1998.

[218] K.B. Moses, A. Reinhardt, and S.G. Advani. Investigation of fiber motion near solid boundaries in simple shear flow. *Rheologica Acta*, 40:296–306, 2000.

[219] A. J. Van der Lelij. 3D ist genauer als 2D - Spritzgiesssimulation mit Volumenelementen. *Kunststoffe*, 87(1):51–53, 1997.

[220] N.N. Füllanalyse ohne Netzgenerierung. *Kunststoffe*, 87(9):1188–1189, 1997.

[221] C. L. Tucker III and S. G. Advani. Processing of Short Fiber Systems. In S. G. Advani, editor, *Flow and Rheology in Polymer Composites Manufacturing*, volume 10 of *Composite Materials Series*. Elsevier, Amsterdam, The Netherlands, 1994.

[222] A. Garcia-Rejon, J.-F. Hétu, L. Pecora, and O. Khennache. 3D mould filling of a transfer sprocket. In *Processing Annual Technical Conference*, pages 567–571. Society of Plastics Engineers, 1998.

[223] W. Michaeli, H. Findeisen, H. Gossel, and Th. Klein. 2,5D und 3D im Vergleich - Spritzgiesssimulationen auf dem Prüfstand. *Kunststoffe*, 87(4):462–466, 1997.

[224] K. Talwar, F. Costa, V. Rajupalem, L. Antanovski, and C. Friedl. Three-dimensional simulation of plastic injection molding. In *Processing Annual Technical Conference*, pages 562–566. Society of Plastics Engineers, 1998.

[225] G. Batch. 3D effects in injection molding simulation. In *Processing Annual Technical Conference*, pages 547–553. Society of Plastics Engineers, 1994.

[226] M. Steffens, N. Himmel, and M. Maier. Design and analysis of discontinuous long fiber reinforced thermoplastic structures for car seat applications. In *Computer Methods in Composite Materials (CADCOMP)*, Montreal, 1998.

[227] M. Steffens. *Zur Substitution metallischer Fahrzeug-Strukturbauteile durch innovative Faser-Kunststoff-Verbund-Bauweisen*. PhD thesis, Universität Kaiserslautern, Kaiserslautern, 2000.

[228] K. Friedrich. Microstructural efficiency and fracture toughness of short fiber / thermoplastic matrix composites. *Composite Science and Technology*, 22:43–47, 1985.

[229] J. Karger-Kocsis and K. Friedrich. Fracture behaviour of injection-molded short and long glass fiber-polyamide6.6 composites. *Composite Science and Technology*, 53:293–325, 1998.

[230] V. Rizov, T. Harmia, A. Reinhardt, and K. Friedrich. Fracture toughness of discontinuous long glass fiber reinforced polypropylene: An approach

based on a numerical prediction of fiber orientation in injection molding. *Applied Composite Materials*, submitted 2001.

[231] Schott AG, 2000.

[232] H. Bach and N. Neuroth. *The Properties of optical Glass*. Springer, Berlin, Heidelberg, New York, 1995.

[233] I. Fanderlik. *Optical Properties of Glass*, volume 5 of *Glass Science and Technology*. Elsevier, Amsterdam, Oxford, New York, Tokyo, 1983.

A Optical Properties of PP-LGF

The transmission for neat and long glass fiber filled PP A.3 was determined using a infrared spectroscope (Nicolet). The bandwidth evaluated was restricted from 2.5 to 8 μm which is the operating range of the IR sensor. Results for neat PP (s. fig. A.1) show excellent agreement with previous studies [170].

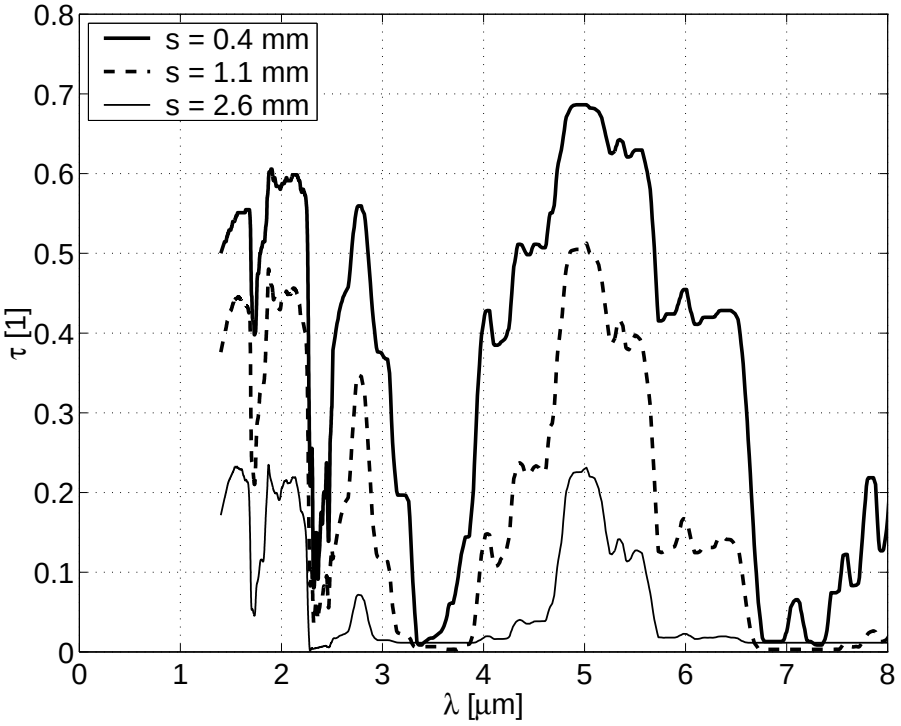

Figure A.1: Spectral Transmission of PP versus plaque thickness

Basically, the transmission spectrum of neat PP contains peaks from 1.8 to 2.2 μm, 2.5 to 3.1 μm and 4 to 6.5 μm. The maximum occurs at 5 μm. Depending on the thickness of the specimen the transmission reaches values of up to 70%. Using planck's law (fig. 3.4) and the transmission spectrum, it was found that for polypropylene the most significant fraction of radiation is emitted between 4 and 6.5 μm.

Radiation in the most important range cannot be detected using IR thermometers with fiber-optic transmission since quartz glass fibers basically absorb any radiation with a wavelength higher than 4 μm (fig. A.2). In the range between 1.5 and 3 μm, glass is virtually transparent with respect to infrared radiation [231].

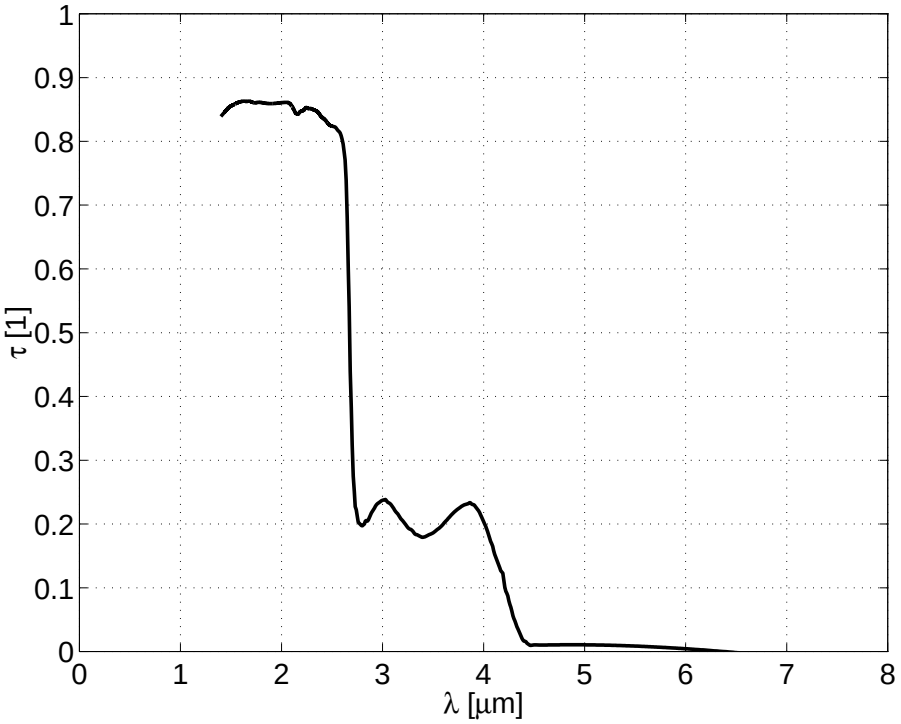

Figure A.2: Spectral Transmission for Float-glass

The transmission spectrum of PP-LGF with different fiber weight fraction is shown in fig.A.3. The difference in thickness of the specimens is of minor importance.

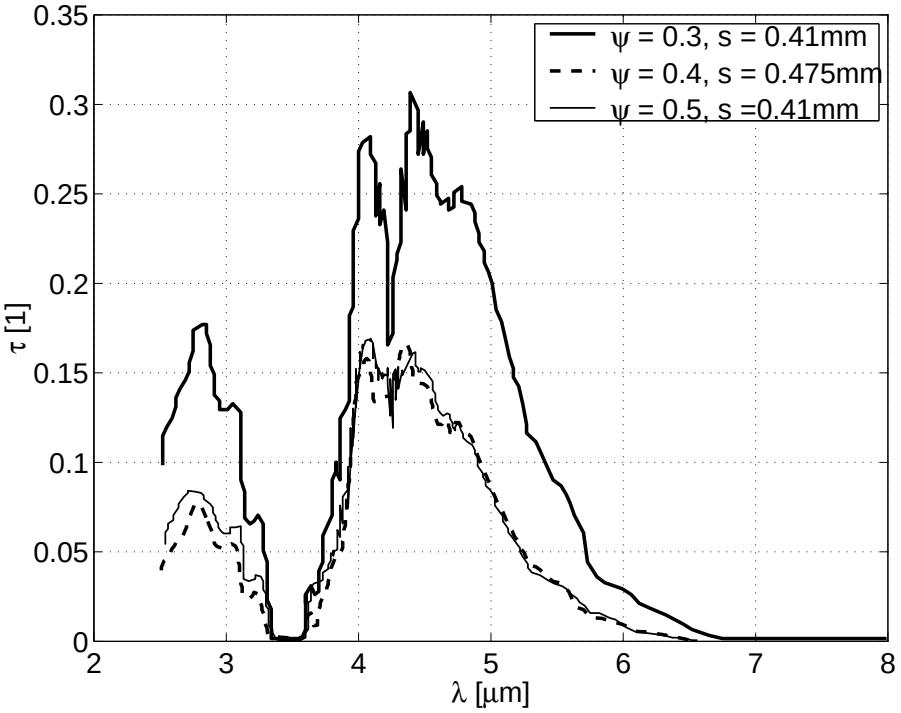

Figure A.3: Spectral Transmission for PP-LGF versus fiber fraction

The addition of long glass fibers significantly reduces the transmission of radiation. The maximum transmission of PP declines from 0.7 to 0.3 and 0.15 for a weight fraction of 30% and 50%, respectively, and is also shifted from 5 to 4.5 μm.

Based on the transmission spectrum of glass (s. fig A.2), the transmission of glass fiber filled should theoretically increase, at least in the range up to 4 μm. The decline in transmission experimentally observed is due to reflection, refraction and attenuation.
With the transmission spectra, the coefficient of absorption μ can be derived using

$$\mu = \frac{1}{d} \cdot log\left(\frac{1}{\tau_i}\right) \tag{A.1}$$

depending on the thickness of the specimen d and its internal transmission

$$\tau_i = \frac{\tau}{P} \tag{A.2}$$

with

$$P = \frac{2n}{n^2 + 1} \tag{A.3}$$

and the refractive index n. The penetration depth d_E, where the intensity has decreased to 1/e (36.8%) is determined using

$$d_E = \frac{1}{\mu} \tag{A.4}$$

The penetration depth for neat PP is shown in fig. A.4. The maximum value of d_E = 1.2mm is obtained at λ = 5 μm. It is also visible, that penetration depth is a strong function of wavelength. At elevated temperature, slightly lower values are obtained [170].

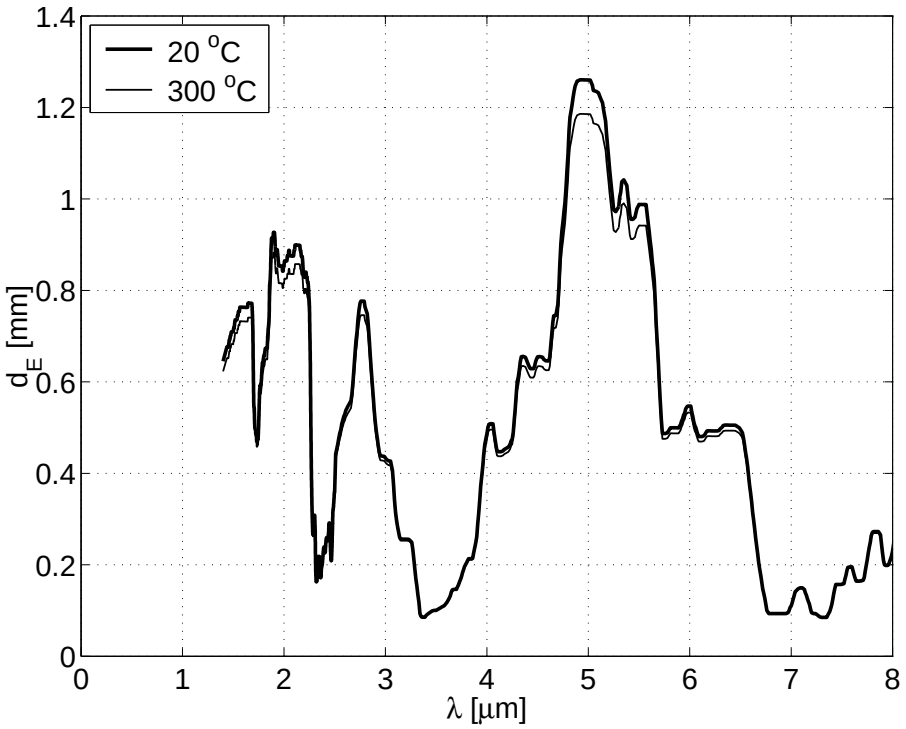

Figure A.4: Penetration depth for PP vs. Temperature

The increase in absorption with temperature allows, with moderate error, the use of transmission spectra obtained at room temperature in order to obtain an upper limit for penetration depth at elevated temperature levels.

According to the transmission spectrum, the penetration depth d_E declines with addition of glass fibers.

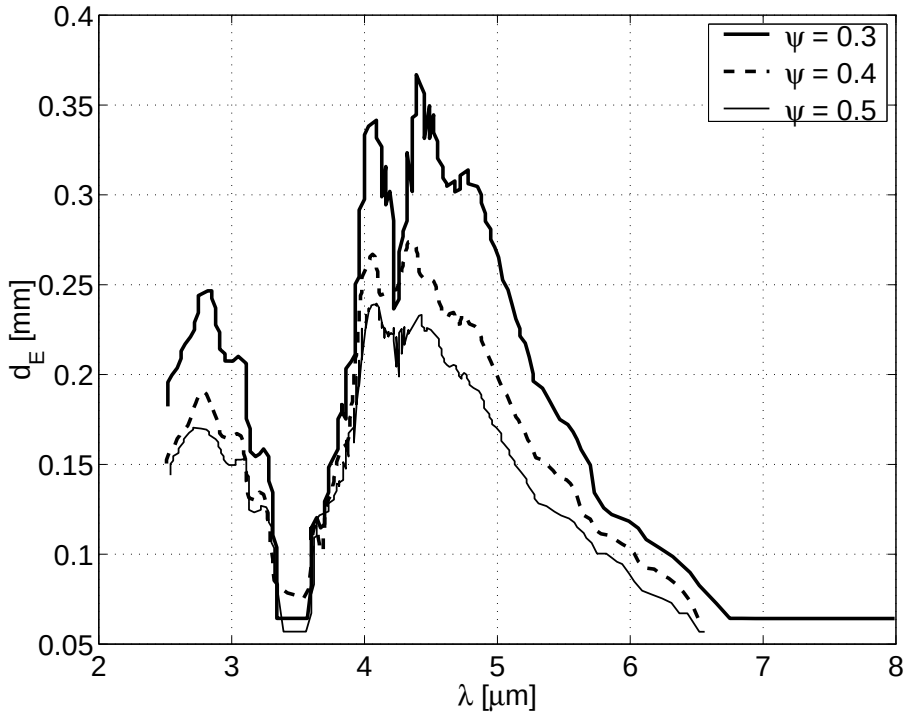

Figure A.5: Penetration depth for PP-LGF

The maximum penetration depth occurs at 4.5 μm and decreases from 0.37 mm to 0.23 mm when the fiber fraction is varied from 30% to 50%. This result deviates from the increase in penetration depth predicted using Beer's law for filled materials [232, 233]

$$\mu = \mu_f \cdot \varphi + \mu_m \cdot (1 - \varphi) \tag{A.5}$$

with the absorption coefficient of the suspension μ, the fibers (μ_f) and the melt (μ_m), respectively.

B Rheometry

B.1 Binding's Analysis

Binding's analysis is based on the assumptions of a no-slip boundary condition at the wall. Power-law behavior of the melt in shear flow is also assumed.

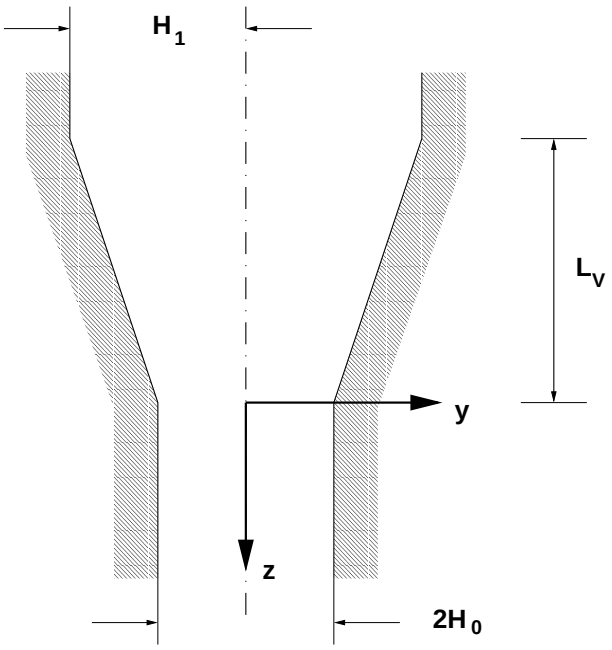

Figure B.1: Convergent flow analysis of extensional viscosity

If the gap-wise velocity is neglected,

$$v_x = 0 \tag{B.1}$$

the velocity in width direction yields

$$v_y = \frac{Q(2n+1)}{2d(n+1)H^2}\left[(y/H)^{1+(1/n)} - 1\right] \cdot y \cdot \left[-\frac{dH}{dz}\right] \tag{B.2}$$

and the velocity in main flow direction is derived as

$$v_z = \frac{Q(2n+1)}{2d(n+1)H}\left[1-(y/H)^{1+(1/n)}\right] \tag{B.3}$$

The cavity wall is described using

$$H(z) = H_0 - \frac{H_1 - H_0}{L_V}\cdot z \tag{B.4}$$

and the derivative yields

$$\frac{dH}{dz} = -\frac{H_1 - H_0}{L_V} \tag{B.5}$$

With the definition of coordinates as depicted in fig. B.1 the stress tensor yields

$$\mathbf{T} = \begin{bmatrix} -p & 0 & 0 \\ 0 & -p+\tau_{yy} & \tau_{yz} \\ 0 & \tau_{yz} & -p+\tau_{zz} \end{bmatrix} \tag{B.6}$$

and the rate of deformation tensor is defined as

$$\mathbf{E} = \frac{1}{2}\left(\nabla\mathbf{v} + \nabla\mathbf{v}^T\right) = \begin{bmatrix} 0 & 0 & 0 \\ 0 & -\dot{\epsilon} & -\dot{\gamma}/2 \\ 0 & -\dot{\gamma}/2 & -\dot{\epsilon} \end{bmatrix} \tag{B.7}$$

The shear rate depends on the distance y from the center line

$$\dot{\gamma} = \frac{Q(2n+1)}{2n\cdot wh^2}\cdot\left(\frac{y}{w}\right)^{1/n} \tag{B.8}$$

If elastic effects are neglected, the rate of dissipation is determined by the contribution of shear and extensional flow

$$\dot{W} = \mathbf{TE} = \dot{W}_S + \dot{W}_E = \eta\dot{\gamma}^2 + \lambda\dot{\epsilon}^2 \tag{B.9}$$

The energy required in order to maintain flow between segments at z und $z+dz$ yields

$$\delta\dot{E} = 2w\left[\int_0^H \left(\dot{W}_S + \dot{W}_E\right)\, dy\right]\delta z + \delta\dot{k} \tag{B.10}$$

where $\delta\dot{k}$ is the increase in kinetic energy due to acceleration. The total energy consumed between to pressure sensors located at L_A and L_B is equal to

the pressure drop multiplied by the flow rate, if recirculation and inertia are neglected:

$$\dot{E} = \left[\Delta p_E + \Delta p_{(-L_v,0)}\right] \cdot Q \tag{B.11}$$

The energy consumption therefore is a function of flow rate, shear viscosity (k, n), extensional viscosity (l, t) and the flow profile and its change

$$\dot{E} = f\left(Q, k, n, l, t, w, \frac{\partial w}{\partial z}\right) \tag{B.12}$$

It is assumed, that the flow profile will yield a shape with minimum energy consumption

$$\delta\dot{E} = f\left(w, \frac{\partial w}{\partial z}\right) \equiv \min \tag{B.13}$$

The rate of energy consumption is then

$$\dot{E} = \frac{kQ(t+1)^2}{2t^2(n+1)^2} \cdot \left[\frac{l(2n+1)tn^t \cdot I_{nt}}{k}\right]^{\frac{1}{t+1}} \cdot \dot{\gamma}_{H_0}^{\frac{t(n+1)}{t+1}} \cdot \left[1 - \alpha^{\frac{2t(n+1)}{t+1}}\right] \tag{B.14}$$

with the wall shear rate in the converging die

$$\dot{\gamma} = \frac{Q(2n+1)}{2n \cdot w{H_0}^2} \tag{B.15}$$

and the inverse of the contraction ratio

$$\alpha = \frac{H_0}{H_1} \tag{B.16}$$

I_{nt} is the integral

$$I_{nt} = \int_0^1 \left[\mid \left(1 - \frac{2n+1}{n}\right) \mid \Phi^{1+\frac{1}{n}}\right]^{t+1} d\Phi \tag{B.17}$$

The maximum of the rate of extension yields

$$\dot{\epsilon} = (n+1) \cdot \left[\frac{k}{l(2n+1)tn^t \cdot I_{nt}}\right] \cdot \dot{\gamma}_{H_0}^{\left(\frac{n+1}{t+1}\right)} \tag{B.18}$$

C Thermal Data

C.1 Specific Heat

Specific Heat of PP-LGF was measured using Differential Scanning Calorimetry (DSC). The dependence of heat capacity on temperature and fiber fraction is plotted in fig.C.1.

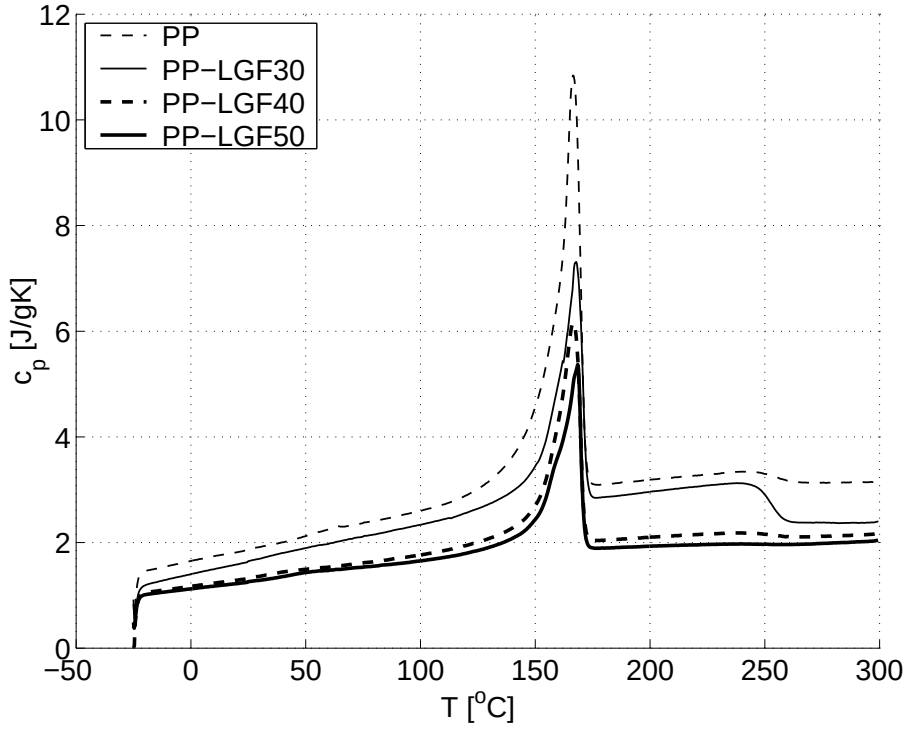

Figure C.1: Specific Heat c_p vs. temperature and fiber fraction

C.2 Conductivity

Thermal conductivity k of PP-LGF was calculated from data of neat PP using the rule of mixture. As depicted in fig. C.2, k is a strong function of temperature and assuming a constant value would produce errors in the order of magnitude of 10% for PP-LGF50 and 50% for neat PP.

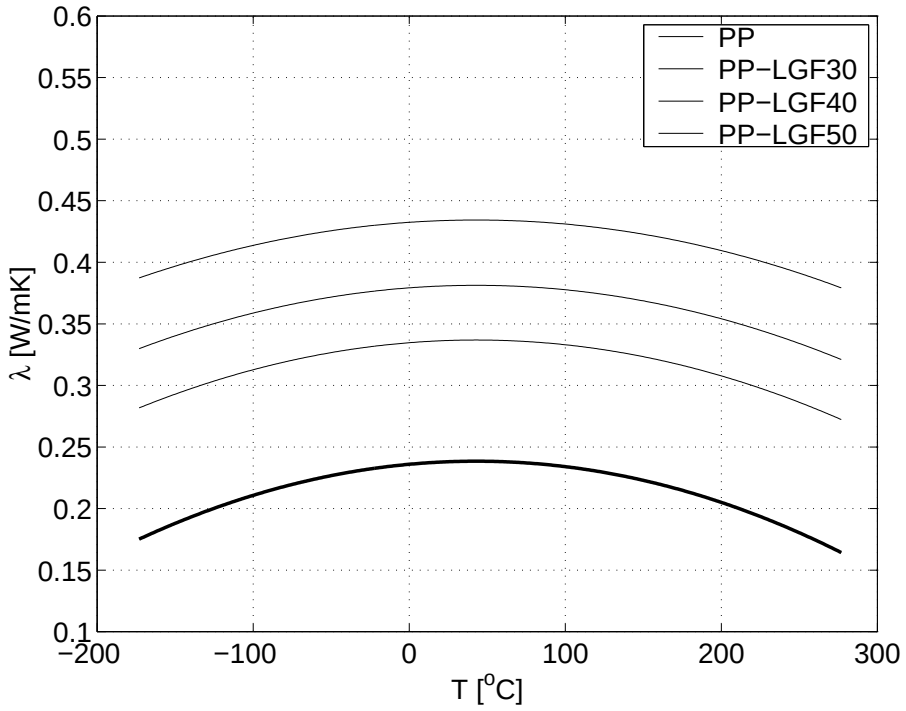

Figure C.2: Thermal conductivity k vs. temperature and fiber fraction

C.3 pvT Data

In order to account for the compressibility of the melt during the mold filling and the packing phase, pvT-data for PP-LGF at different fiber fraction was derived from data of neat PP taken from literature [64]. Based on the change of density $\rho = 1/v$ of neat PP with pressure and temperature, the density of fiber filled PP was calculated using the rule of mixture.
The density values are re-converted into values for v. Applying non-linear least-square curve-fit methods, the coefficients of the compressibility law given by Menges for both solid and liquid state are derived using

$$v = \frac{K_1}{p + K_2} + \frac{K_3}{p + K_4} * T + K_5 \cdot e^{K_6 * T - K_7 * p} \tag{C.1}$$

K_5, K_6 and K_7 are assumed to be zero in the liquid region. The transition between solid and liquid state is assumed to depend on pressure only and is given by

$$T_s(p) = K_8 + K_9 * p \tag{C.2}$$

The values of the pvT-law for different fiber fractions are listed in table C.1.

			φ [%]			
			0	30	40	50
solid	K_1	[10^4 cm^3 bar/g]	5.3402	4.9914	4.8451	4.6822
	K_2	[10^4 bar]	4.8117	5.5935	5.9034	6.2485
	K_3	[cm^3 bar/g^{o}C]	0.4731	0.6042	0.5909	0.5474
	K_4	[10^3 bar]	0.9512	2.0313	2.4307	2.8374
	K_5	[10^{-9} cm^3/g]	3.6795	3.6795	3.6795	3.6795
	K_6	[1/^{o}C]	0.1442	0.0286	0.0286	0.0286
	K_7	[10^{-2} 1/bar]	0.3186	1.5112	1.5112	1.5112
transition	K_8	[10^2 ^{o}C]	1.2967	1.2951	1.2949	1.2948
	K_9	[10^{-2} ^{o}C/bar]	1.9100	1.9131	1.9101	1.9037
liquid	K_1	[10^4 cm^3 bar/g]	4.6678	4.5044	4.4090	4.2677
	K_2	[10^4 bar]	4.0963	4.9243	5.2500	5.5762
	K_3	[cm^3 bar/g^{o}C]	1.0071	0.7491	0.6422	0.5360
	K_4	[10^3 bar]	1.2277	1.2136	1.2155	1.2266

Table C.1: pvT data for PP-LGF, solid and liquid phase

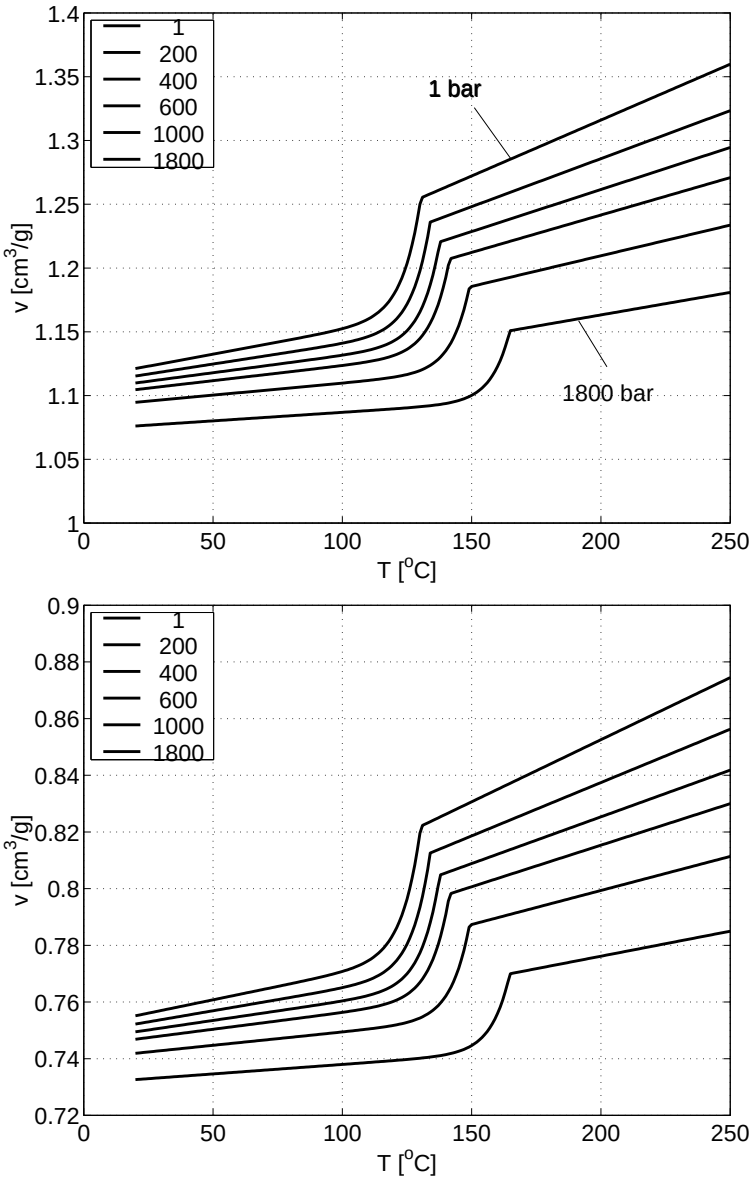

Figure C.3: pvT diagram for PP (top) and PP-LGF50 (bottom)